Development of Electrode Materials with Efficient Carbon Network for Fast Rechargeable Lithium-ion Batteries

리튬이온전지의 빠른 충/방전을 위한 효율적인

탄소네트워크를 가진 전극물질의 개발

2019년 2월

서울대학교 융합과학기술대학원

융합과학부 나노융합전공

오 지 섭

Development of Electrode Materials with Efficient Carbon Network for Fast Rechargeable Lithium-ion Batteries

지도 교수 박 원 철

이 논문을 공학박사 학위논문으로 제출함
2018년 10월

서울대학교 융합과학기술대학원
융합과학부 나노융합전공
오 지 섭

오지섭의 공학박사 학위논문을 인준함
2019년 2월

위 원 장 _____ (인)

부위원장 _____ (인)

위   원 _____

위   원 _____ (인)

위   원 _____ (인)

Abstract

Development of the Electrode Material with Efficient Carbon Network for Fast Rechargeable Lithium-ion Batteries

Jiseop Oh

Program in Nano Science and Technology

Graduate School of Convergence Science & Technology

Seoul National University

As global warming problem emerged, green energy technologies and electric vehicles have been considered solution to reduce greenhouse gas emission. Lithium ion batteries have drawn a lot of attention as an energy storage device due to high energy density and lightweight characteristics. The requirements of energy storage devices for high power application are power capability, cost effectiveness, and safety. The lithium ion

batteries systems suffer from sluggish rate performance due to electron transfer and ion diffusion in electrode materials. To improve the rate performance of both anode and cathode materials, material engineering and electrode architecturing should be considered.

Dual carbon layer coating strategy for LiFePO$_4$ (LFP), which uses polydopamine-derived nitrogen-doped carbon (N-doped carbon) and reduced graphene oxide (RGO) was applied to improve the rate performance. These dual carbon layers are prepared by a one-pot polymerization process and thermal treatment. The dual carbon coated LFP has a rate capability with a discharge capacity of 98 mAh g^{-1} at 30 C, cycling performance with a discharge capacity of 115 mAh g^{-1} at 10 C, and 96.18% capacity retention after 700 cycles. The high rate performance and the excellent long-term cycling stability can be attributed to the enhanced electric conductivity with N-doped carbon coating, the well-connected electron pathway, and the fast Li$^+$ ion diffusion induced by the small size of the particles.

The composite of N-doped carbon coated LFP (NCL) nanoparticles attached to rGO wrapped N-doped carbon framework was synthesized using polydopamine as binding agent as well as carbon coating source and studied as cathode material for lithium ion battery. The N-doped

carbon framework provided a high surface area for attaching the LFP particles, pore space for Li ion migration, and network for high electrical conductivity. LFP nanoparticles were densely attached to N-doped carbon framework due to the interaction between rGO and polydopamine. Furthermore, the high interaction between rGO and polydopamine could help to achieve long cyclic stability of the electrode material. The as-prepared N-doped carbon framework@rGO@N-doped carbon coated LFP (NCFG-NCL) showed excellent cycle stability with a capacity retention of 92.2% after 500 cycle at a 2 C. A remarkable rate performance with a discharge capacity of 108 mAh g^{-1} even at 20 C was also achieved.

Ultrafine Sn nanoparticles were anchored on graphene-hollow carbon framework and studied as an anode material for lithium-ion battery. Graphene-hollow carbon framework (G-HCF) anchors ultrafine Sn nanoparticles on its surface to prevent them from aggregation. The hollow structure can provide a buffer space to accommodate the volume expansion of the Sn particles and prevents electrode pulverization during the charge/discharge process. Furthermore, the interconnected hollow carbon structure enables rapid lithium ion and electron transport to give the enhanced rate performance. Also, the G-HCF was doped with

nitrogen and phosphorus to stabilize its electrochemical performance. Consequently, the as-prepared G-HCF-Sn composite exhibited a highly stable cycling performance, even at a current density of 1.0 A g^{-1} (specific capacity of 1048 mA h g^{-1} after 1000 cycles).

Keywords: carbon network, LFP, Sn, polydopamine, graphene, melamine foam, lithium ion battery

Student Number: 2013-23750

Contents

Chapter 2. Dual Layer Coating Strategy Utilizing N-doped Carbon and Reduced Graphene Oxide for High-Performance LiFePO₄ Cathode Material

Chapter 3. Melamine Foam derived N-doped Carbon Framework and Graphene Supported LiFePO₄ Composite for High-performance Lithium-ion Battery Cathode Material

Chapter 4. Ultrafine Sn Nanoparticles Anchored on Nitrogen- and Phosphorus-Doped Hollow Carbon Frameworks for Lithium Ion Batteries

List of Figures

18

List of Tables

List of abbreviations

Chapter 1.

1. **EVs** : Electric Vehicles

2. **HEVs** : Hybrid Electric Vehicles

3. **LFP** : Lithium Iron Phosphate ($LiFePO_4$)

4. **NMC** : $Li(Ni_{1/3}Co_{1/3}Mn_{1/3})O_2$

5. **NCA** : $Li(Ni_{0.8}Co_{0.15}Al_{0.05})O_2$

6. **CNT** : Carbon Nanotube

7. **CNF** : Carbon NanoFiber

Chapter 2.

1. **RGO** : Reduced graphene oxide

2. **GO** : Graphene oxide

3. **XRD** : X-ray diffractometer

4. **SEM** : Scanning electron microscopy

5. **EDS** : Energy-dispersive spectrometer

6. **FE-SEM** : Field emission scanning electron microscope

7. **HR-TEM** : High-resolution transmission electron microscopy

8. **BET** : Brunauer-Emmett-Teller

9. **XPS** : X-ray photoelectron spectroscopy

10. **TGA** : Thermogravimetric analysis

11. **PVDF** : Poly(vinylidene fluoride)

12. **NMP** : N-methyl-2-pyrrolidone

13. **EC** : Ethylene carbonate

14. **DEC** : Diethyl carbonate

15. **NC** : Nitrogen-doped carbon

16. **LFP NP** : $LiFePO_4$ nanoplate (lithium iron phosphate nanoplate)

17. **LFP NP@NC@RGO** : $LiFePO_4$ nanoplate@Nitrogen-doped carbon@reduced graphene oxide

18. **LFP NP@NC** : $LiFePO_4$ nanoplate@Nitrogen-doped carbon

19. **LFP NP@RGO** : $LiFePO_4$ nanoplate@reduced graphene oxide

Chapter 3.

1. **rGO** : Reduced graphene oxide

2. **GO** : Graphene oxide

3. **LFP** : LiFePO$_4$ (lithium iron phosphate)

4. **XRD** : X-ray diffractometer

5. **FE-SEM** : Field emission scanning electron microscopy

6. **HR-TEM** : High-resolution transmission electron microscopy

7. **BET** : Brunauer-Emmett-Teller

8. **BJH** : Barrett-Joyner-Halenda

9. **XPS** : X-ray photoelectron spectroscopy

10. **TGA** : Thermogravimetric analysis

11. **EIS** : Electrochemical impedance spectroscopy

12. **FT-IR** : Fourier-transform infrared spectroscopy

13. **PVDF** : Poly(vinylidene fluoride)

14. **NMP** : N-methyl-2-pyrrolidone

15. **EC** : Ethylene carbonate

16. **DEC** : Diethyl carbonate

17. **NCF** : Nitrogen-doped carbon framework

18. **NCFG** : Nitrogen-doped carbon framework@reduced graphene oxide

19. **NCL** : Nitrogen-doped carbon coated $LiFePO_4$

20. **NCF-NCL** : Nitrogen-doped carbon framework@Nitrogen-doped carbon coated $LiFePO_4$

21. **NCFG-NCL** : Nitrogen-doped carbon framework@reduced graphene oxide@Nitrogen-doped carbon coated $LiFePO_4$

22. **NCFG-PD@LFP** : Nitrogen-doped carbon framework@reduced graphene oxide-Polydopamine@$LiFePO_4$

Chapter 4.

1. **rGO** : Reduced graphene oxide

2. **GO** : Graphene oxide

3. **LFP** : $LiFePO_4$ (lithium iron phosphate)

4. **XRD** : X-ray diffractometer

5. **FE-SEM** : Field emission scanning electron microscopy

6. **HR-TEM** : High-resolution transmission electron microscopy

7. **BET** : Brunauer-Emmett-Teller

8. **XPS** : X-ray photoelectron spectroscopy

9. **TGA** : Thermogravimetric analysis

10. **EIS** : Electrochemical impedance spectroscopy

11. **CV** : Cyclic voltammetry

12. **FT-IR** : Fourier-transform infrared spectroscopy

13. **EDS** : Energy-dispersive spectrometer

14. **PVDF** : Poly(vinylidene fluoride)

15. **NMP** : N-methyl-2-pyrrolidone

16. **EC** : Ethylene carbonate

17. **DEC** : Diethyl carbonate

18. **LFP@PD@GO** : $LiFePO_4$@polydopamine@graphene oxide

19. **HCF** : Hollow carbon framework

20. **G-HCF** : Reduced graphene oxide-hollow carbon framework

21. **G-HCF-LFP** : Reduced graphene oxide-hollow carbon framework-LiFePO$_4$

22. **G-Sn** : Reduced graphene oxide-Sn

23. **HCF-Sn** : Hollow carbon framework-Sn

24. **G-HCF-Sn** : Reduced graphene oxide-hollow carbon framework-Sn

25. **SEI** : Solid-electrolyte interphase

Chapter 1. Introduction

1.1. Lithium ion battery

1.1.1. Introduction

Since lithium ion batteries have been introduced in 1991, portable electronics (smart phone, tablet, etc) has entered our lives and development of lithium ion battery with safety, large capacity, high power and high energy, and long lifespan is attracting attention. Furthermore, as the global warming problem emerged, governments around the world recognized the problem of greenhouse gases on climate
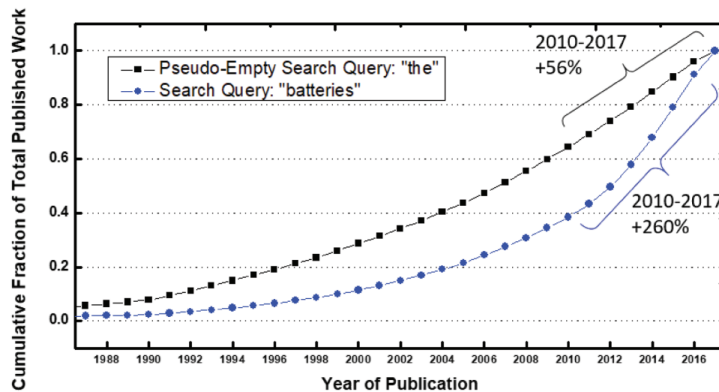
Figure 1.1. Comparison of literature growth from 1987 to 2017 in field of "batteries", utilizing the Web of Science (from Ref. [2] *Adv. Mater.* **2018**, *30*, (33), 1800561-1800561.)

change and planned to develop green energy technologies (solar, wind, etc) and electric vehicles (EVs) as a core solutions. The electrification of transportation has become an important component to reduce greenhouse gas emission.[1] Lithium ion batteries have been considered as an essential material for EVs due to the lightweight and high energy density of lithium ion batteries. Consequently, many papers have been published explosively on the subject of "batteries",[2] shown in **figure 1.1.**

In the early days of lithium ion batteries, lithium ion batteries had been
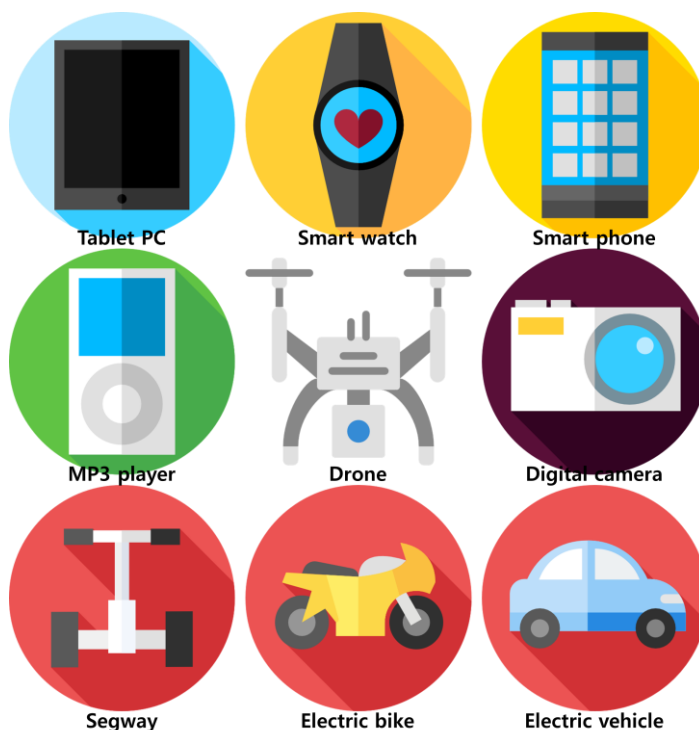
Figure 1.2. Portable and large scale devices

used in consumer electronics such as laptop and cellular phone. As battery technology has evolved, lithium ion batteries are applied to the power tool and power supply. Efforts have also been made to introduce lithium ion batteries into large scale and high power applications such as EVs, and hybrid electric vehicles (HEVs) (**figure 1.2.**).

The advent of large scale and high power applications (EVs, HEVs) dramatically changes the requirements of lithium ion batteries. Portable devices, which are represented by smartphones and tablet PCs, are designed for portability and ease of use. Therefore, batteries for portable devices are required to have miniaturization, shape deformability, high energy density, safety, and cycle stability. On the other hand, batteries for large-scale and high power applications, represented by EVs and HEVs,
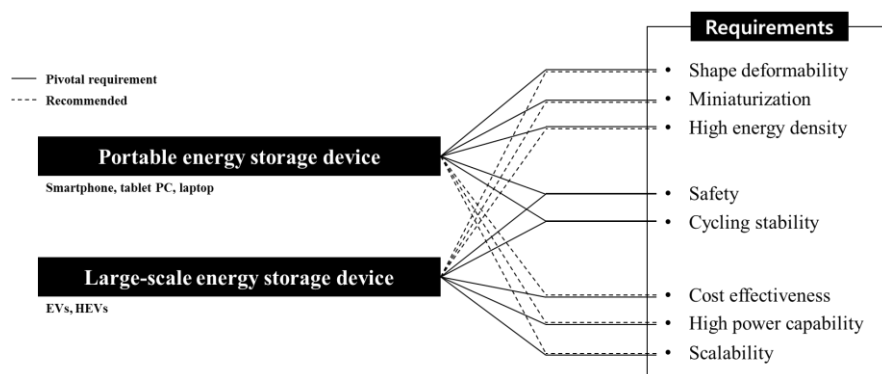
Figure 1.3. Requirements for portable and large-scale energy storage devices

3 4

are required to have power capability, cost effectiveness and safety rather than miniaturiation and shape deformability. To meet the requirements of batteries for large-scale and high power devices, a lot of researches on the electrode materials are needed. (**Figure 1.3.**)

1.1.2. Outline of lithium ion batteries

An electrochemical cell store the energy converting the chemical energy into electrical energy. Lithium ion battery, which is one kind of electrochemical cell, is energy storage device based on lithium redox
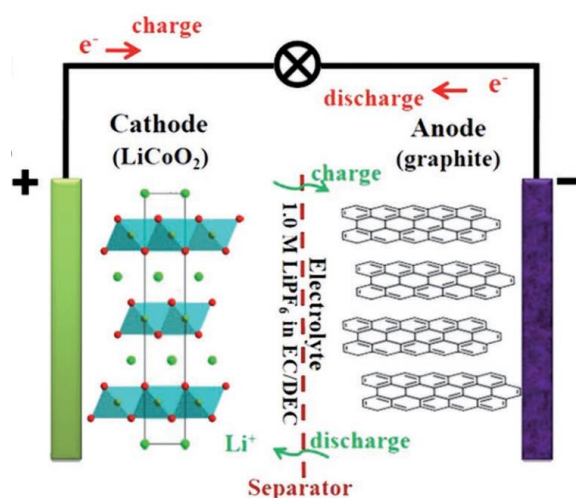
Figure 1.4. Charge/discharge process in lithium ion batteries with graphite anode and $LiCoO_2$ cathode. (from Ref. [3] *Adv. Energy. Mater.* **2018**, *8*, (6), 1701415.)

reaction. Lithium ion batteries consist of a cathode, anode, separator and electrolyte.[3] (**Figure 1.4.**)

When an electrochemical redox reaction occurs in the electrode, ions move between anode and cathode through the electrolyte, and at the same time, electron moves between the electrodes through the external circuit. Electrochemically oxidation of the electrode material occurs during the discharge process, and this electrode is called anode. Electrochemically reduction of the electrode material occurs by electrons transferred from the anode through the external circuit during the discharge process, and this electrode is called cathode. Electrolyte is ionic conductors that bridging ionic connection between two electrodes but insulating electrons.

1.1.3. Lithium ion batteries electrodes

1.1.3.1. Anode

Lithium metal anode has high specific capacity (3860 mAh g^{-1}), but it can lead to safety problems due to formation of dendrite during charge/discharge process and strong reactivity between the electrolyte and lithium metal.[4] There has been effort to find new anode materials that are safer and more stable than lithium metal. As a result, many kinds of anode materials have been studied, and they can be classified into three types depending on the type of reaction: intercalation type anode materials such as graphite and $Li_4Ti_5O_{12}$, alloying reaction type anode
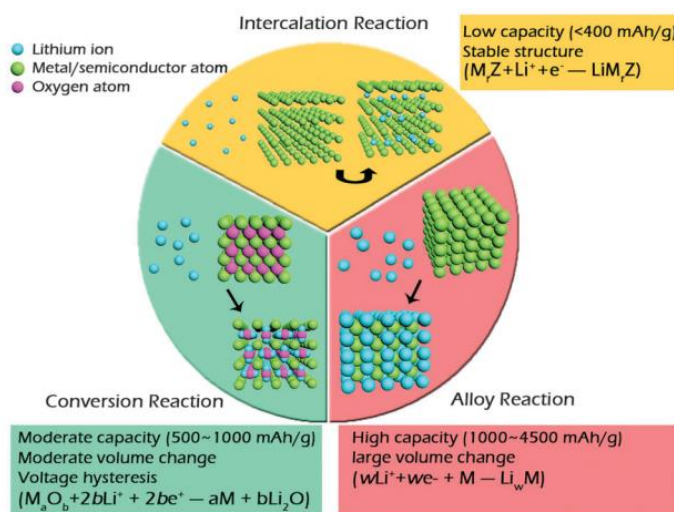
Figure 1.5. A schematic representation of three typical reaction mechanisms (from Ref. [5] *Chem. Soc. Rev.* **2015**, *44*, (17), 5926-5940.)

materials such as Sn, Ge and Si, and conversion reaction type anode materials based on transition metal oxides.[5] (**Figure 1.5.**)

1.1.3.2. Cathode

Since the introduction of layered metal oxide, various cathode materials have been studied.[3] (**Figure 1.6.**) The various cathode materials can be divided into three classes: layered structure represented by $LiCoO_2$, Mn-based spinel structure represented by $LiMn_2O_4$, and polyanion structure represented by lithium iron phosphate (LFP). Cathode material determines the capacity and output voltage of the lithium ion battery. Also, since most of the battery cost is generated in the cathode material, many researchers have been working on improving the cathode material. (**Figure 1.5.**)
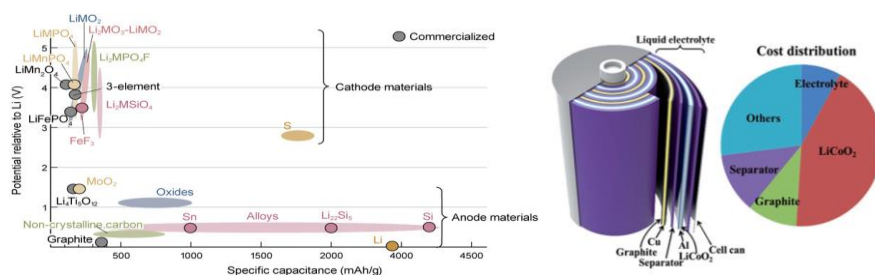
Figure 1.6. (a) Relative potential and specific capacity of anode and cathode materials, and (b) structural illustration and relative cost of cell components (from Ref. left image: *Nikkei Electronics Asia,* Feb., **2010**., right image: [3] *Adv. Energy. Mater*. **2018**, *8*, (6), 1701415.)

1.2. Anode materials for lithium ion batteries

1.2.1. Intercalation based anode

Graphite has a layered structure, which allows lithium ions to be inserted between the layers. Graphite can be divided into two types depending on the degree of crystallinity and carbon atoms stacking.[4] Soft carbon (grahpitizable carbon) is well-known graphite with reversible capacity (i.e. LiC_6, 350-370 mAh g^{-1}), in which graphene layers are stacked almost in the same direction. On the other hand, hard carbon (non-graphitizable carbons) has a structure where the graphene layers are randomly oriented. This structure provide many voids space to accomodate lithium.[6-9] Many automobile and battery companies have focused on developing hard carbon as anode material for EVs because of its high reversible capacity. However, hard carbon has several disadvantages: poor rate performance, low initial coulombic efficiency, low tap density, and lihium ion deposition problem on carbon anode due to low equilibrium potential.

Another anode cadidate is $Li_4Ti_5O_{12}$ with high operating potential of 1.55 V vs Li/Li$^+$ (no metal deposition), low volume change (<5%), high

reversible capacity. When lithium is inserted/extracted into $Li_4Ti_5O_{12}$, it undergoes structural change from spinel $Li_4Ti_5O_{12}$ to rock salt type $Li_7Ti_5O_{12}$ with zero-strain.[10-12] Currently, $Li_4Ti_5O_{12}$ is used as battery for EVs and HEVs because it has very fast charge/discharge, good cycling stability and good calendar life. However, it has a low theoretical capacity of 175 mAh g^{-1} and low electronic conductivity ($\sim 10^{-13}$ S cm^{-1}),[13] which is disadvantageous to be utilized for high power battery application.

1.2.2. Conversion based anode

Since conversion compounds M_aO_b (M = Co, Fe, Ni, Mn, Cu, etc) are discovered by Tarascon *et al.*[14] transition metal compounds (oxides, sulphides, nitrides, phosphides) have been studied as anode materials for lithium ion batteries due to their high specific capacity values. During the charge/discharge process, these oxides, sulphides, nitrides, and phosphides are converted to a lithium compounds (Li_xN_y; N = O, S, P, and N) and reversibly returned to initial state. These anode materials exhibit high reversible capacities (~ 1000 mAh g^{-1}) due to the multitple electron reaction, which make conversion material an attractive anode materials. However, there are disadvantages such as poor reaction

kinetics, large volume expansion, high energy barrier in the breaking of lithium compounds (Li_xN_y; N = O, S, P, and N),[15] which causes the poor electrochemical performance and cycling stability.

1.2.3. Alloying based anode (Sn)

Many researchers have focused on alternative anode materials such as Si, Ge, and Sn, which have highest volumetric and gravimetric energy densities. Alloy compounds Li_xM (M = Si, Sn, Ge, etc) can store large amout of lithium ion per M. Among them, Sn-based materials have been considered as a promising anode material for high-power lithium ion batteries because of the abundance, appropriate working voltage, high theoretical capacity (992 mAh g^{-1} for $Li_{4.4}Sn$), and high electrical conductivity of Sn.[16] Tin anodes shows higher volumetric capacity of about 2000 mAh cm^{-3} and gravitational capacity of 990 mAh g^{-1} than the commercial graphite as well as other transition metal compound anodes. However, the practical application of Sn-based anodes is hampered because Sn exhibits large volume changes (~300%) during the charge/discharge process, which causes electrode pulverization and consequently quick capacity fading during cycling.[17]

1.3. Cathode materials for lithium ion batteries

1.3.1. Layered structure (LiMO$_2$)

In general, the layered structure forms a layer with CoO_6 octahedral via sharing edges and forms a fast 2D lithium ion diffusion channel between the CoO_2 interlayers.[18] (**figure 1.7.**) This structure is suitable for high-rate cathode material. However, when $LiCoO_2$ is over-delithiated ($Li_{x \to 0}CoO_2$), Co_3O_4 and O_2 are generated by phase transfomation,[19] which cause the exothermic combustion of electrolyte, anode material, separator.[19] In addition, due to the expensive and toxic Co, researchers developed multi-cation layered oxide to replace cobalt ion. Promising candidates such as $Li(Ni_{1/3}Co_{1/3}Mn_{1/3})O_2$ (NMC) and $Li(Ni_{0.8}Co_{0.15}Al_{0.05})O_2$ (NCA) have been developed.[20-22] NMC material is widely used in lithium ion battery for EVs due to increased capacity, high decomposition temperature. In generally, the higher Ni contents in active material, the higher specific capacity. But it exhibit poorer stability at high charge/discharge rates. NCA, another Ni-rich ternary metal cathode material, has excellent thermal stability (extothermic reactions at higher temperatures than $LiCoO_2$). Ni-rich compounds suffer from similar drawbacks. During the electrochemical process, Ni^{2+} irreversibly

migrates to the Li^+ site, hindering the transfer of Li^+ and increase the overall cell impedance. Furthermore, there is a difficulty in synthesis and storage, due to the chemical sensitivity of Ni^{3+}.
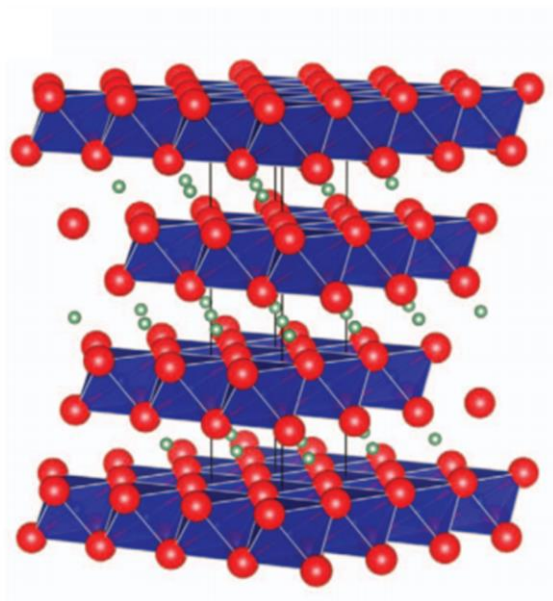
Figure 1.7. Crystal structure of layered $LiCoO_2$ (from Ref. [18] *NPG Asia Materials*, **2016**, 8, 254.)

1.3.2. Spinel structure (LiMn$_2$O$_4$)

LiMn$_2$O$_4$ has a 3D spinel structure with dual charge plateau at 3 V and 4 V *vs.* Li/Li$^+$.[23] This structure is suitable for high-rate cathode material due to its 3D pathway for Li-ion transport. However, LiMn$_2$O$_4$ has serious capacity fading problems due to dissolution of Mn^{2+} cuased by disproportionation reaction ($2Mn^{3+} \rightarrow Mn^{4+} + Mn^{2+}$) at high temperature into the electrolyte.[24] The dissolution of Mn cation cause the phase transformation and volume expansion of LiMn$_2$O$_4$. Furthermore, the Mn cations dissoloved from LiMn$_2$O$_4$ migrated to the anode, which increase resistance of the anode. (**Figure 1.8.**)
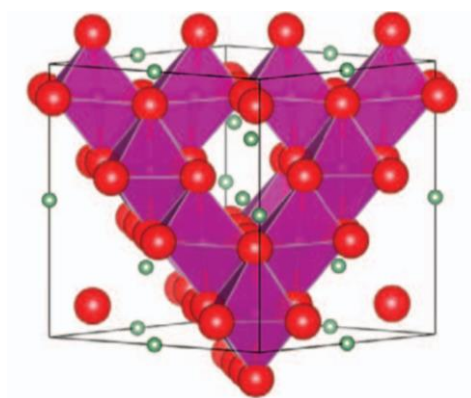
Figure 1.8. Crystal structure of spinel LiMn$_2$O$_4$ (from Ref. [18] *NPG Asia Materials*, **2016**, *8*, 254.)

1.3.3. Olivine structure (LiMPO₄, M = Fe, Mn, Co, Ni)

LiFePO$_4$ has olivine structure which belongs to a polyanion compounds. (**Figure 1.9.**) LFP, a low cost and nontoxic material, has excellent thermal stability, a high theoretical capacity (170 mAh g^{-1}), an acceptable operation potential (3.4 V *vs.* Li/Li$^+$) along with its abundant precursors.[25-28] Furthermore, two-phase lithiation process of LFP offers a stable voltage plateau. Due to the strong bonding of polyanions (PO$_4^{3-}$), structural stability of LFP is better than other layered and spinel structures. These advantages make LFP a promising cathode material for high-rate lithium ion battery. However, 1-dimensional lithium diffusion
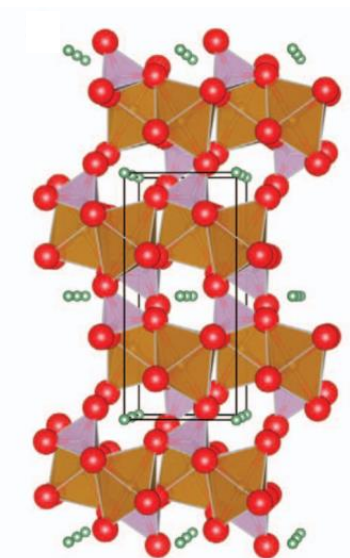
Figure 1.9. Crystal structure of olivine LiFePO$_4$ (from Ref. [18] *NPG Asia Materials*, **2016**, 8, 254)

in the [010] direction leads to poor diffusivity in the bulk ($\sim 10^{-14}$ cm^2 s^{-1}). In addition, LFP exhibits poor electronic conductivity ($\sim 10^{-10}$ S cm^{-1}), making it difficult to be used practically.[29-31] Many reports on the use of LFP in large-scale energy storage devices, such as EVs, HEVs, and energy storage systems, have been made.[32] Currently, Battery Company in China is producing lithium batteries with LFP cathode and graphite anode.[2] (**Table 1.1.**)

Battery company	Vehicle of application [company/model]	Battery material [anode||cathode]
AESC	Nissan/Leaf	Graphite||LMO-NCA
LG Chem	Renault/Zoe	Graphite||NMC-LMO
Li-Tec	Daimler/Smart	Graphite||NMC
Li Energy Japan	Mitsubishi/i-MiEV	Graphite||LMO-NMC
Samsung	Fiat/500	Graphite||NMC-LMO
Lishen Tianjin	Coda/EV	Graphite||LFP
Toshiba	Honda/Fit	LTO||NMC
Panasonic	Tesla/Model S	Graphite||NCA

Table 1.1. List of battery company, and battery materials (from Ref. [2] *Adv. Mater.* **2018**, *30*, (33), 1800561-1800561.)

1.4. Motivation and thesis outline

1.4.1. Introduction

There is a growing interest in lithium ion batteries due to the widespread utilization of consumer electronics and transport electricfication. Lithium ion batteries for large scale, high power applications such as EVs and HEVs require different pivotal requirements (safety, cycling stability, cost effectiveness, high power capability, and scalability), compared to portable devices. In order to meet these requirements, it is necessary to improve the electrochemical performance of anode and cathode materials.

To create high-rate lithium ion batteries, it is necessary to understand the diffusion process of lithium ions and electrons in battery system. **Figure 1.10.** shows the discharge process of lithium ion batteries. (1) Lithium ion and electron disassociation occurs in the anode material during the discharge process. (2) Lithium ions diffuse through the electrolyte and reach the electrolyte/electrode interface of the cathode material. (3) On the other hand, the electron pass through anode particles and reach the current collector. And the elctron travels along the outer circuit to the opposite electrode material. (4) Lithium ions and electrons enter the cathode material.[5]
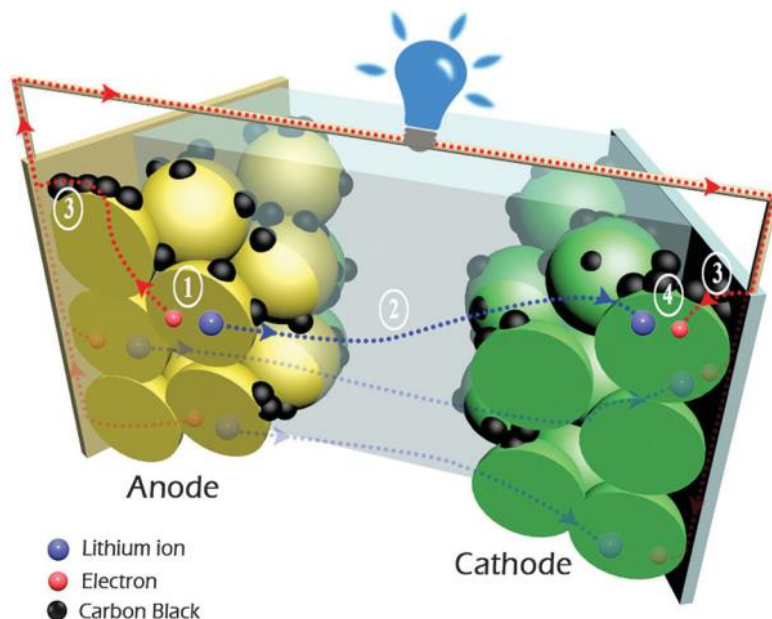
Figure 1.10. Lithium ion and electron diffusion pathway in lithium ion batteries during discharge process (from Ref. [5] *Chem. Soc. Rev.* **2015**, *44*, (17), 5926-5940.)

1.4.2. Material engineering (Sn based anode material)

Sn-based materials have been considered as a promising anode material for large scale and high power lithium ion batteries because of advantageous characteristics of Sn. However, the poor cycling stability of Sn-based anode material is caused by the large volume expansion of Sn during charge/discharge process. To overcome the issues during the charge/discharge process, material level engineering has been conducted. (**Figure 1.11**)

1. Sn based material nanostructuring

Particle size reduction is an effective way to reduce the mechanical stress caused by volume change of Sn during the lithiaion/delithiation process reducing the surface to volume ratio. In addition, the lithium and electron diffusion path is shortened, which improve the rate performance of Sn anode. Furthermore, Sn nanoparticles can accommodate the volume expansion during lithiation without fracture.[33, 34] Thus, cycling stability also improved by material nanostructuring. However, side reactions with the electrolyte due to high specific surface area can cause cycling stability problems. In addition, during the lithiation/delithiation process, volume expansion occurs between Sn nanoparticles, causing the particles aggregation.[34, 35] Cracking and fracture are exhibited to these aggregated Sn particles, resulting in poor cycling stability.

2. Sn based material surface modification

Core-shell structure consisting of mechanically robust and electrically conducting shell and active material core is an efficient way to improve the electrochemical performance of the Sn anode. In this case, shape, thickness, and uniformity of shells should be considered because these factors affect the lithium ion diffusion, volume expansion, and electric

conductivity. However, the high stress is generated due to repetitive volume changes during lithiation/delithiation process, and cause the cycling stability problem. Considering this phenomenon, the yolk-shell structure which provide a space to accomodates volume expansion of Sn has been considered as another solution.[36]

3. Hybrid-composite design

There have been efforts to anchoring Sn particles to carbon additive (such as carbon back, carbon nanotube (CNT), carbon nanofiber (CNF), and graphene) to diminish the internal stress/strain by volume change and increase the electronic conductivity.[37-40] In the case of Graphene additive, the flexible structure of grapnhene provides a buffer space for the volume change of Sn and electron pathway. Thus, Sn and carbon additive composite can alleviate the pulverization problem of the electrode.

1.4.3. Material engineering (LiFePO$_4$ cathode material)

Olivine type LFP has been used as high-rate cathode material for lithium ion batteries because its advantages are sufficient to meets the requirements of large scale and high power application. However, its sluggish electron and Li ion transport lead to poor rate capability of LFP. To address thees issues, material engineering strategies have been widely used. (**Figure 1.11.**)

1. LiFePO$_4$ nanostructuring

Particle size reduction is the most efficient way to improve ionic and electronic conductivity by shortening the lithium ion and electron pathway. There have been efforts to obtain samll LFP particles.[41-43] However, the smaller particle size, the more interface between the particles. Thus, electrochemical performance depends on contact mode and contact resistance between particles.[44, 45] As the particle size becomes smaller, the specific surface area becomes larger, resulting in decreasing volumetric energy density. Also, the larger specific surface area, the larger surface energy, which cause the side reaction between the electrolyte and active materials.

2. LiFePO$_4$ surface modification (carbonaceous material coating)

Carbon coating is an efficient way to improve the electronic conductivity of LFP.[46] It also acts as a protective layer to prevent unwanted particle growth during heat treatment and side reactions with the electrolyte, which helps to avoid loss of power density of LFP when used in high power applications. However, the thickness and crystallinity of the carbon coating affects the electrochemical performance of active materials.[47] In addition, the uniformity of the carbon coating affects the rate performance of LFP because the coating on the LFP surface can transfer the electron in all directions during the electrochemical reaction.[48] To achieve the uniform carbon layer, various organic carbon sources, such as citric acid and sucrose, are commonly used.[49, 50]

3. Dopant manipulation

Dopant manipulation is an intrinsic way to improve the electronic conductivity of LFP.[51-53] There are two doping sites in LFP and the lithium diffusivity can be improved depending on the doping position. Alien ion doping in the Li-site improves the lithium diffusivity in the bulk by expanding the 1-dimensional diffusion channels. In addition, alien ion doping in the Fe-site weakens the Li-O interaction and improve

the electronic and ionic conductivity.[52] However, the mechanism of electronic conductivity improvement is still controversial.

4. Li-ion diffusion control

LFP has 1-dimensional lithium diffusion pathway along the b axis. Thus, facet tailoring of LFP is one of the efficient way to improve the rate performance with exposed (010) surface facets.[54, 55] The rate capability of LFP are varied depending on how the crystal orientation tuning of the LFP. However, synthetic process of crytstal orientation tailored LFP is not simple.

5. Hybrid-composite design

Designing a hybrid composite with a conductive additive is a way to improve electronic transport.[54, 56] Carbon based materials (such as carbon back, CNT, CNF and graphene), conductive polymers, and metallic compounds are used as conductive additives. Conducting materials improve the electronic transport by forming an electron pathway which electrically interconnect the active materials.
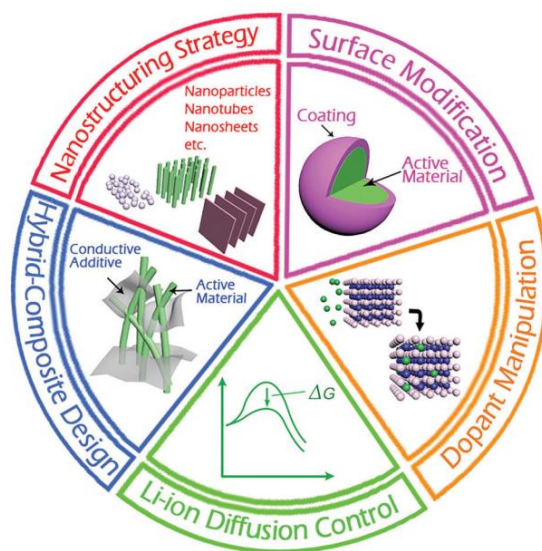
Figure 1.11. Material level engineering (from Ref. [5] *Chem. Soc. Rev*. **2015**, *44*, (17), 5926-5940.)

1.4.4. Electrode architecturing

Electrode architecting is a method of boosting the high-rate performance of lithium ion batteries by improving the ion and electron transport kinetics in the electrode. Various electrode structures have been proposed, including a porous network structure capable of rapid ion transport, maximizing the surface area of the electrode, and forming an electron conductive pathway from the active material to the current collector.[57]

1.4.5. Motivation

The lithium ion batteries suffer from sluggish charging/discharge due to slow (1), (4) solid-state diffusion, (2) lithium ion diffusion in electrolyte, and (3) electron transfer in both anode and cathode materials. (Figure 1.10.) (1), and (4) steps are related to material engineering. (2), and (3) steps are related to electrode architecturing. All steps can be a rate determining step that determines the electrode performance during high-rate charge/discharge process.

In order to make lithium ion batteries for large scale, high power applications, not only material level engineering but also electrode architecturing at system level should be considered. The objective of the thesis is to experimentally develop the efficient carbon network for fast rechargeable lithium ion batteries electrode materials (LFP cathode, and Sn anode) by combining the material and system level engineering. These carbon network prvide the efficient electron and ion pathway, which results in improved electrochemical properties.

1.5. References

1.   Tran, M.;   Banister, D.;   Bishop, J. D. K.; McCulloch, M. D., Realizing the electric-vehicle revolution. *Nat. Clim. Change* **2012,** *2,* (5), 328-333.

2.   Li, M.;   Lu, J.;   Chen, Z. W.; Amine, K., 30 Years of Lithium-Ion Batteries. *Adv. Mater.* **2018,** *30*, (33), 1800561-1800561.

3.   Zhou, L. M.;   Zhang, K.;   Hu, Z.;   Tao, Z. L.;   Mai, L. Q.; Kang, Y. M.;   Chou, S. L.; Chen, J., Recent Developments on and Prospects for Electrode Materials with Hierarchical Structures for Lithium-Ion Batteries. *Adv. Energy. Mater.* **2018,** *8*, (6), 1701415.

4.   Goriparti, S.;   Miele, E.;   De Angelis, F.;   Di Fabrizio, E.; Zaccaria, R. P.; Capiglia, C., Review on recent progress of nanostructured anode materials for Li-ion batteries. *J. Power Sources* **2014,** *257*, 421-443.

5.   Tang, Y. X.;   Zhang, Y. Y.;   Li, W. L.;   Ma, B.; Chen, X. D., Rational material design for ultrafast rechargeable lithium-ion batteries. *Chem. Soc. Rev.* **2015,** *44*, (17), 5926-5940.

6.   Bridges, C. A.;   Sun, X. G.;   Zhao, J. K.;   Paranthaman, M. P.; Dai, S., In Situ Observation of Solid Electrolyte Interphase Formation in Ordered Mesoporous Hard Carbon by Small-Angle Neutron

Scattering. *J Phys Chem C* **2012,** *116* (14), 7701-7711.

7.   Fujimoto, H.;   Tokumitsu, K.;   Mabuchi, A.;   Chinnasamy, N.; Kasuh, T., The anode performance of the hard carbon for the lithium ion battery derived from the oxygen-containing aromatic precursors. *J. Power Sources* **2010,** *195*, (21), 7452-7456.

8.   Liu, Y. H.;   Xue, J. S.;   Zheng, T.; Dahn, J. R., Mechanism of lithium insertion in hard carbons prepared by pyrolysis of epoxy resins. *Carbon* **1996,** *34*, (2), 193-200.

9.   Yang, J.;   Zhou, X. Y.;   Li, J.;   Zou, Y. L.; Tang, J. J., Study of nano-porous hard carbons as anode materials for lithium ion batteries. *Mater. Chem. Phys.* **2012,** *135*, (2-3), 445-450.

10.   Li, X. F.; Wang, C. L., Engineering nanostructured anodes via electrostatic spray deposition for high performance lithium ion battery application. *J. Mater. Chem. A* **2013,** *1*, (2), 165-182.

11.   Martha, S. K.;   Haik, O.;   Borgel, V.;   Zinigrad, E.;   Exnar, I.;   Drezen, T.;   Miners, J. H.;   Aurbach, D., $Li_4Ti_5O_{12}/LiMnPO_4$ Lithium-Ion Battery Systems for Load Leveling Application. *J. Electrochem. Soc.* **2011,** *158*, (7), A790-A797.

12.   Wagemaker, M.; Mulder, F. M., Properties and Promises of Nanosized Insertion Materials for Li-Ion Batteries. *Accounts Chem. Res.*

2013, *46* (5), 1206-1215.

13.   Zhu, G. N.;   Chen, L.;   Wang, Y. G.;   Wang, C. X.;   Che, R. C.; Xia, Y. Y., Binary $Li_4Ti_5O_{12}$-$Li_2Ti_3O_7$ Nanocomposite as an Anode Material for Li-Ion Batteries. *Adv. Funct. Mater.* **2013,** *23*, (5), 640-647.

14.   Poizot, P.;   Laruelle, S.;   Grugeon, S.;   Dupont, L.; Tarascon, J. M., Nano-sized transition-metal oxides as negative-electrode materials for lithium-ion batteries. *Nature* **2000,** *407*, 496.

15.   Hayner, C. M.;   Zhao, X.; Kung, H. H., Materials for Rechargeable Lithium-Ion Batteries. *Annu Rev Chem Biomol* **2012,** *3*, 445-471.

16.   Courtney, I. A.; Dahn, J. R., Electrochemical and in situ x-ray diffraction studies of the reaction of lithium with tin oxide composites. *J. Electrochem. Soc.* **1997,** *144*, (6), 2045-2052.

17.   Winter, M.; Besenhard, J. O., Electrochemical lithiation of tin and tin-based intermetallics and composites. *Electrochim. Acta* **1999,** *45*, (1-2), 31-50.

18.   Deng, Z.;   Mo, Y. F.; Ong, S. P., Computational studies of solid-state alkali conduction in rechargeable alkali-ion batteries. *NPG Asia Mater.* **2016,** *8*, 254.

19.   Doh, C. H.;   Kim, D. H.;   Kim, H. S.;   Shin, H. M.;   Jeong,

Y. D.; Moon, S. I.; Jin, B. S.; Eom, S. W.; Kim, H. S.; Kim, K. W.; Oh, D. H.; Veluchamy, A., Thermal and electrochemical behaviour of C/Li$_x$CoO$_2$ cell during safety test. *J. Power Sources* **2008,** *175*, (2), 881-885.

20. Kalyani, P.; Kalaiselvi, N.; Renganathan, N. G.; Raghavan, M., Studies on LiNi$_{0.7}$Al$_{0.3-x}$Co$_x$O$_2$ solid solutions as alternative cathode materials for lithium batteries. *Mater. Res. Bull.* **2004,** *39*, (1), 41-54.

21. Li, Z.; Chernova, N. A.; Roppolo, M.; Upreti, S.; Petersburg, C.; Alamgir, F. M.; Whittingham, M. S., Comparative Study of the Capacity and Rate Capability of LiNi$_y$Mn$_y$Co$_{1-2y}$O$_2$ (y=0.5, 0.45, 0.4, 0.33). *J. Electrochem. Soc.* **2011,** *158*, (5), A516-A522.

22. Xu, J.; Lin, F.; Doeff, M. M.; Tong, W., A review of Ni-based layered oxides for rechargeable Li-ion batteries. *J. Mater. Chem. A* **2017,** *5*, (3), 874-901.

23. Hunter, J. C., Preparation of a New Crystal Form of Manganese-Dioxide-λ-MnO$_2$. *J. Solid State Chem.* **1981,** *39*, (2), 142-147.

24. Xu, B.; Qian, D. N.; Wang, Z. Y.; Meng, Y. S. L., Recent progress in cathode materials research for advanced lithium ion batteries. *Mat. Sci. Eng. R* **2012,** *73*, (5-6), 51-65.

25. Padhi, A. K.; Nanjundaswamy, K. S.; Goodenough, J. B.,

Phospho-olivines as positive-electrode materials for rechargeable lithium batteries. *J. Electrochem. Soc.* **1997,** *144*, (4), 1188-1194.

26.   Yamada, A.; Chung, S. C.; Hinokuma, K., Optimized $LiFePO_4$ for lithium battery cathodes. *J. Electrochem. Soc.* **2001,** *148*, (3), A224-A229.

27.   Padhi, A. K.; Nanjundaswamy, K. S.; Masquelier, C.; Okada, S.; Goodenough, J. B., Effect of structure on the Fe^{3+}/Fe^{2+} redox couple in iron phosphates. *J. Electrochem. Soc.* **1997,** *144*, (5), 1609-1613.

28.   Andersson, A. S.; Thomas, J. O.; Kalska, B.; Haggstrom, L., Thermal stability of $LiFePO_4$-based cathodes. *Electrochem. Solid-State Lett.* **2000,** *3*, (2), 66-68.

29.   Wang, J. J.; Sun, X. L., Olivine $LiFePO_4$: the remaining challenges for future energy storage. *Energy Environ. Sci.* **2015,** *8*, (4), 1110-1138.

30.   Chung, S. Y.; Bloking, J. T.; Chiang, Y. M., Electronically conductive phospho-olivines as lithium storage electrodes. *Nat. Mater.* **2002,** *1*, (2), 123-128.

31.   Nishimura, S.; Kobayashi, G.; Ohoyama, K.; Kanno, R.; Yashima, M.; Yamada, A., Experimental visualization of lithium

diffusion in Li$_x$FePO$_4$. *Nat. Mater.* **2008,** *7*, (9), 707-711.

32.　　Swierczynski, M.; Stroe, D. I.; Stan, A. I.; Teodorescu, R.; Kaer, S. K., Lifetime Estimation of the Nanophosphate LiFePO$_4$/C Battery Chemistry Used in Fully Electric Vehicles. *IEEE. Trans. Ind. Appl.* **2015,** *51*, (4), 3453-3461.

33.　　Kravchyk, K.; Protesescu, L.; Bodnarchuk, M. I.; Krumeich, F.; Yarema, M.; Walter, M.; Guntlin, C.; Kovalenko, M. V., Monodisperse and Inorganically Capped Sn and Sn/SnO$_2$ Nanocrystals for High-Performance Li-Ion Battery Anodes. *J. Am. Chem. Soc.* **2013,** *135*, (11), 4199-4202.

34.　　Wang, J. W.; Fan, F. F.; Liu, Y.; Jungjohann, K. L.; Lee, S. W.; Mao, S. X.; Liu, X. H.; Zhu, T., Structural Evolution and Pulverization of Tin Nanoparticles during Lithiation-Delithiation Cycling. *J. Electrochem. Soc.* **2014,** *161*, (11), F3019-F3024.

35.　　Courtney, I. A.; McKinnon, W. R.; Dahn, J. R., On the aggregation of tin in SnO composite glasses caused by the reversible reaction with lithium. *J. Electrochem. Soc.* **1999,** *146*, (1), 59-68.

36.　　Kang, S.; Chen, X.; Niu, J. J., Sn Wears Super Skin: A New Design for Long Cycling Batteries. *Nano Lett.* **2018,** *18*, (1), 467-474.

37.　　Liu, L. J.; Huang, X. K.; Guo, X. R.; Mao, S.; Chen, J. H.,

Decorating in situ ultrasmall tin particles on crumpled N-doped graphene for lithium-ion batteries with a long life cycle. *J. Power Sources* **2016,** *328*, 482-491.

38.   Guo, Y. Y.;   Zeng, X. Q.;   Zhang, Y.;   Dai, Z. F.;   Fan, H. S.;   Huang, Y.;   Zhang, W. N.;   Zhang, H.;   Lu, J.;   Huo, F. W.; Yan, Q. Y., Sn Nanoparticles Encapsulated in 3D Nanoporous Carbon Derived from a Metal-Organic Framework for Anode Material in Lithium-Ion Batteries. *ACS Appl. Mater. Interfaces* **2017,** *9*, (20), 17173-17178.

39.   Zhang, N.;   Zhao, Q.;   Han, X. P.;   Yang, J. G.; Chen, J., Pitaya-like Sn@C nanocomposites as high-rate and long-life anode for lithium-ion batteries. *Nanoscale* **2014,** *6*, (5), 2827-2832.

40.   Shi, X.;   Song, H. H.;   Li, A.;   Chen, X. H.;   Zhou, J. S.; Ma, Z. K., Sn-Co nanoalloys embedded in porous N-doped carbon microboxes as a stable anode material for lithium-ion batteries. *J. Mater. Chem. A* **2017,** *5*, (12), 5873-5879.

41.   Nan, C. Y.;   Lu, J.;   Li, L. H.;   Li, L. L.;   Peng, Q.; Li, Y. D., Size and shape control of LiFePO₄ nanocrystals for better lithium ion battery cathode materials. *Nano Research* **2013,** *6*, (7), 469-477.

42.   Burch, D.; Bazant, M. Z., Size-Dependent Spinodal and Miscibility Gaps for Intercalation in Nanoparticles. *Nano Lett.* **2009,** *9*,

(11), 3795-3800.

43.   Cho, M. Y.;   Kim, H.;   Kim, H.;   Lim, Y. S.;   Kim, K. B.;   Lee, J. W.;   Kang, K.; Roh, K. C., Size-selective synthesis of mesoporous LiFePO$_4$/C microspheres based on nucleation and growth rate control of primary particles. *J. Mater. Chem. A* **2014,** *2* (16), 5922-5927.

44.   Su, F. Y.;   You, C. H.;   He, Y. B.;   Lv, W.;   Cui, W.;   Jin, F. M.;   Li, B. H.;   Yang, Q. H.; Kang, F. Y., Flexible and planar graphene conductive additives for lithium-ion batteries. *J. Mater. Chem.* **2010,** *20*, (43), 9644-9650.

45.   Kim, J. Y.; Kotov, N. A., Charge Transport Dilemma of Solution-Processed Nanomaterials. *Chem. Mater.* **2014,** *26*, (1), 134-152.

46.   Zhu, P. P.;   Yang, Z. Y.;   Zhang, H.;   Yu, J.;   Zhang, Z.;   Cai, J. X.; Li, C., Utilizing egg lecithin coating to improve the electrochemical performance of regenerated lithium iron phosphate. *J. Alloy Compd.* **2018,** *745*, 164-171.

47.   Doeff, M. M.;   Hu, Y. Q.;   McLarnon, F.; Kostecki, R., Effect of surface carbon structure on the electrochemical performance of LiFePO$_4$. *Electrochem. Solid-State Lett.* **2003,** *6*, (10), A207-A209.

48.   Wang, Y. G.;   Wang, Y. R.;   Hosono, E. J.;   Wang, K. X.;

Zhou, H. S., The design of a LiFePO$_4$/carbon nanocomposite with a core-shell structure and its synthesis by an in situ polymerization restriction method. *Angew. Chem. Int. Ed.* **2008,** *47*, (39), 7461-7465.

49.   Chen, Z. Y.;   Zhu, H. L.;   Ji, S.;   Fakir, R.;   Linkov, V., Influence of carbon sources on electrochemical performances of LiFePO$_4$/C composites. *Solid State Ionics* **2008,** *179*, (27-32), 1810-1815.

50.   Milev, A.;   George, L.;   Khan, S.;   Selvam, P.; Kannangara, G. S. K., Li-ion kinetics in LiFePO$_4$/carbon nanocomposite prepared by a two-step process: The role of phase composition. *Electrochim. Acta* **2016,** *209*, 565-573.

51.   Liu, W. M.;   Liu, Q. L.;   Qin, M. L.;   Xu, L.; Deng, J. Y., Inexpensive and green synthesis of multi-doped LiFePO$_4$/C composites for lithium-ion batteries. *Electrochim. Acta* **2017,** *257*, 82-88.

52.   Gao, L. B.;   Xu, Z. R.; Zhang, S., The co-doping effects of Zr and Co on structure and electrochemical properties of LiFePO$_4$ cathode materials. *J. Alloy. Compd.* **2018,** *739*, 529-535.

53.   Yue, H. F.;   Wang, D.; Li, L. S., The synergistic effect of multiple doping on structure and electrochemical performance of LiFe$_{1-x-y-z}$Zn$_x$Mn$_y$Ca$_z$PO$_4$. *J. Alloy. Compd.* **2017,** *711*, 617-626.

54.   Wang, B.;   Al Abdulla, W.;   Wang, D. L.; Zhao, X. S., A three-

dimensional porous LiFePO$_4$ cathode material modified with a nitrogen-doped graphene aerogel for high-power lithium ion batteries. *Energy Environ. Sci.* **2015,** *8*, (3), 869-875.

55.   Rui, X. H.;   Zhao, X. X.;   Lu, Z. Y.;   Tan, H. T.;   Sim, D. H.;   Hng, H. H.;   Yazami, R.;   Lim, T. M.; Yan, Q. Y., Olivine-Type Nanosheets for Lithium Ion Battery Cathodes. *ACS Nano* **2013,** *7*, (6), 5637-5646.

56.   Wang, X.;   Feng, Z.;   Huang, J.;   Deng, W.;   Li, X.;   Zhang, H.; Wen, Z., Graphene-decorated carbon-coated LiFePO$_4$ nanospheres as a high-performance cathode material for lithium-ion batteries. *Carbon* **2018,** *127*, 149-157.

57.   Fischer, M. G.;   Hua, X.;   Wilts, B. D.;   Castillo-Martinez, E.; Steiner, U., Polymer-Templated LiFePO$_4$/C Nanonetworks as High-Performance Cathode Materials for Lithium-Ion Batteries. *ACS Appl. Mater. Interfaces* **2018,** *10*, (2), 1646-1653.

Chapter 2. Dual Layer Coating Strategy Utilizing N-doped Carbon and Reduced Graphene Oxide for High-Performance LiFePO₄ Cathode Material

2.1. Introduction

LFP has attracted considerable attention as a promising cathode material for lithium ion battery since the pioneering report by Padhi et al. [1] LFP, a low cost and nontoxic material, has excellent thermal stability, a high theoretical capacity (170 mAh g^{-1}), an acceptable operation potential (3.4 V vs. Li/Li$^+$) along with its abundant precursors.[2-4] Consequently, many reports on the use of LFP in large-scale energy storage devices, such as electric vehicles (EVs), hybrid electric vehicles (HEVs), and energy storage systems, have been made.[5, 6] Nevertheless, LFP is not fully utilized in highperformance applications because of its intrinsic drawbacks such as low electronic conductivity (~10^{-10} S cm^{-1}) and Li-ion diffusivity (~10^{-14} cm^2 s^{-1}).[7-9] To overcome these drawbacks, the use of carbon additives,[10-12] the control of particle size[13-15] and morphology,[16-18] and alien ion doping[19, 20] have been widely utilized.

For practical use in EV and HEV applications, the rate performance, which depends on fast lithium ion and electron transport in the battery, must be improved.[21] Conductive carbon additives such as amorphous carbon, carbon nanotubes, and RGO are commonly added to enhance the electronic conductivity. Another technique to achieve this is particle size reduction[21, 22] because small particles have shorter Li-ion and electron diffusion pathways in the solid phase, enhancing the cathode performance of LFP.[23] However, as the particle size of LFP powder moves from the micro- to the nanoscale, carbon additives must be added more to connect the active materials, resulting in low loading of active materials. Carbon coating is a good method to enhance the electric conductivity while not lowering the mass loading of active materials. Furthermore, carbon coating can act as a blocking layer between the active material and the electrolyte, preventing unwanted side reactions during the charge/discharge processes;[24] in addition, the carbon coating suppresses particle growth during heat treatment.[25]

The properties of carbon coating such as the thickness and crystallinity can affect electrochemical performances. The thin uniform carbon layer can improve the electrochemical performance of LFP significantly because the coating on the LFP surface can transfer the electrons in all

directions during the electrochemical reaction.[26] To achieve a uniform carbon layer, various organic carbon sources, such as citric acid and sucrose, are commonly used.[27, 28] Furthermore, most of the carbon layers derived from the organic carbon sources are amorphous carbon, and electrochemical performance is significantly affected by the carbon structure in LFP/C composites.[29] Therefore, the carbon source must be carefully selected to improve electrochemical performance. Dopamine is a well-known, naturally occurring carbon precursor containing catechol and amine functional groups. Polydopamine-derived carbon shows highly graphitic characteristic (nearly 100% sp^2C)[30, 31] and produces a highly uniform carbon layer.32 In addition, dopamine can be easily polymerized to polydopamine on any substrate under weakly basic conditions, and the layer thickness can easily be controlled. These properties make it suitable for electrochemical applications.

However, in the system level perspective, carbon coating approaches have focused on improving the intrinsic properties of LFP, such as its low electronic conductivity, which, because carbon coated particles are connected in a "point-to-point" mode, is not an efficient way to attain a good rate performance.[33, 34] This "point-to-point" mode is not beneficial to fast charge and discharge performance because of the low contact area

between LFP particles. One way to improve rate performance is to increase the interparticle contact area between the carbon coated LFP particles by using conductive carbon additives based electrode architecturing. Among the various carbon additives, RGO has attracted attention because of its large specific surface area, excellent electronic conductivity, flexibility, and mechanical strength, favorable properties for increasing interparticle contact area.

Herein, we report a crystalline LFP nanoplate (LFP NP) that is coated with a dual carbon layer composed of polydopamine-derived nitrogen-doped carbon (NC) and RGO. This coated LFP NP material has an excellent rate performance and long cycling stability, and we believe that polydopamine plays three important roles in this material. First, polydopamine connects the active materials and conductive additives; secondly, it is a thickness-controlled conductive N-doped carbon layer due to amine groups in the dopamine monomer; thirdly, it prevents LFP NP particles from agglomerating during thermal treatment. The RGO layer forms a well-interconnected structure that may enlarge the particle-to-particle contact area, resulting in efficient electron transport pathway between the active materials. Furthermore, the thickness-controlled N-doped carbon layers are not sufficiently thick to impede Li-ion transport,

and N-doped carbon layers enhance the electronic conductivity of LFP. Moreover, these dual carbon layers can be prepared easily in a one-pot polymerization and thermal treatment process. To confirm the effect of carbon structural difference of mono- and dual carbon coating on battery performance, we compared the electrochemical performances of LFP nanoplate@N-doped carbon@RGO (LFP NP@NC@RGO), LFP nanoplate@N-doped carbon (LFP NP@NC), and LFP nanoplate@RGO (LFP NP@RGO) composites.

2.2. Experimental Section

2.2.1. Chemicals

Dopamine hydrochloride, Tris-buffer, and lithium hydroxide monohydrate ($LiOH \cdot H_2O$, 99%) were purchased from Sigma-Aldrich. Phosphoric acid (H_3PO_4, 85%) was purchased from ACROS. Iron sulfate heptahydrate ($FeSO_4 \cdot 7H_2O$, 99%) was purchased from Alfa Aesar. Ethylene glycol was purchased from SAMCHUN. All chemicals were used without further purification.

2.2.2. Characterization methods

The crystallographic structures of the samples were characterized by X-ray diffractometer (XRD; Bruker New D8 Advance, 40 kV, 40 mA, Cu-$K\alpha$ radiation source, scan range in 2θ of 5–80˚). Scanning electron microscopic (SEM) images were obtained with a field emission scanning electron microscope (FE-SEM; Hitachi S-4800, 15 kV) equipped with an energy-dispersive spectrometer (EDS). The microstructures of the samples were characterized by high-resolution transmission electron microscopy (HR-TEM; JEOL JEM-2100F, 200 keV). Nitrogen adsorption/desorption isotherms at 77 K were measured using a

BELSORP-mini II (MicrotracBEL Corp). The Brunauer-Emmett-Teller (BET) method was used to calculate the average pore diameter and the Barrett-Joyner-Halenda (BJH) method was used to calculate the average pore diameter. X-ray photoelectron spectroscopy (XPS) was conducted on Axis-HIS with Al irradiation at 12 kV and 18 mA at a constant pass energy of 20 eV. Raman analysis was performed with a Raman spectrometer (Horiba T64000).

2.2.3. Preparation of bare LFP nanoplates (bare LFP NP)

LiFePO$_4$ nanoparticles were prepared by solvothermal synthesis using LiOH•H$_2$O (99%, Sigma-Aldrich), H$_3$PO$_4$ 85% (Acros), and FeSO$_4$•7H$_2$O (99% Alfa Aesar) as precursors in the stoichiometric ratio of 2.7:1:1.5, respectively. First, an appropriate quantity of LiOH•H$_2$O was dissolved in ethylene glycol (45 mL, SAMCHUN). Then, H$_3$PO$_4$ was added dropwise into the above solution with vigorous stirring. FeSO$_4$•7H$_2$O was dissolved in ethylene glycol (30 mL). Subsequently, the LiOH•H$_2$O solution was added into the iron sulfate solution with stirring. The obtained olive green suspension was transferred into a Teflon-lined stainless steel autoclave and then heated at 180 °C for 10 h. After heating, the autoclave was cooled to room temperature. The

obtained gray precipitates were washed with EtOH and DI water several times. Finally, the LFP residues were dried in an oven overnight.

2.2.4. Preparation of LFP nanoplate@N-doped carbon@RGO (LFP NP@NC@RGO) and LFP nanoplate@N-doped carbon (LFP NP@NC)

The as-prepared bare LFP NP powder was dispersed in Tris-buffer solution (10 mM) by sonication. Then, dopamine hydrochloride (3 mg/mL, 200mL H_2O) was added to the above suspension and stirred for 15 min. Then, graphene oxide suspension (3wt% in H_2O) was added to the dopamine solution over 10 min. After reacting for 5 min, the suspension of LFP, dopamine, and graphene oxide suspension was washed three times with DI water and dried at 70 °C in an oven for 10 h. The collected $LiFePO_4$ nanoplate@polydopamine@GO composite was calcined at 700 °C for 5 h in Ar-filled Swagelok container to form LFP NP@NC@RGO. For comparison, LFP NP@NC samples were also prepared under the same condition without RGO.

2.2.5. Preparation of LFP nanoplate@RGO (LFP NP@RGO)

The as-prepared bare LFP NP powder was dispersed in DI water. The

graphene oxide suspension (3wt% in H_2O) was added. The mixture was stirred for 30 min. And then, the suspension of LFP and graphene oxide suspension was filtered and dried at 70 $^\circ$C in an oven for 10 h. The collected $LiFePO_4$ nanoplate@GO composite was calcined in Ar-filled Swagelok container at 700 $^\circ$C for 5 h.

2.2.6. Electrochemical Characterization

The electrode was prepared by mixing the as-prepared active materials, Super P (Timcal, carbon black), and poly(vinylidene fluoride) (PVDF) with N-methyl-2-pyrrolidone (NMP, Aldrich) in a weight ratio of 70:15:15. The mixed slurry was spread onto an aluminum foil current collector and dried at 120 $^\circ$C under vacuum for 10 h. Then, coin type 2016 cell was assembled in an Ar-filled glove box with a lithium foil as the counter electrode and Celgard 2450 membrane was used as the separator. The loading mass of active material was ranged between 1.6 mg cm^{-2} and 2.6 mg cm^{-2}. The electrolyte was 1 M $LiPF_6$ in ethylene carbonate (EC) and diethyl carbonate (DEC) in a 1:1 v/v mixture of solvent. Electrochemical tests were conducted by a WBCS3000s cycler (WonATech, Korea) within a potential window of 2.0–4.2 V vs. Li/Li$^+$.

2.3. Results and Discussion

The preparation process of LFP NP@NC@RGO is illustrated in Figure 2.1.a The catechol groups of dopamine were first chemisorbed to metal groups on LFP NP, and the amine groups of dopamine were adsorbed to functional groups of graphene oxide (GO) via formation of amide bonds.[35-38] During the synthesis process, LFP NP particles became anchored on the GO surface due to the polymerization of the dopamine on the GO and LFP NP surfaces. To enhance the crystallinity of the LFP NP particles, the nanoparticles were heat treated. During thermal treatment, the GO layers were reduced to RGO layers, and polydopamine layers were converted into N-doped carbon layers. As shown in Figure.
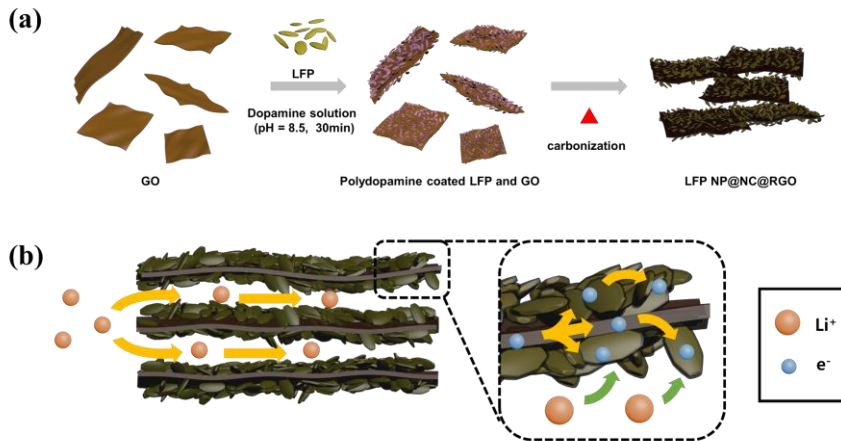
Figure 2.1. Schematic illustration of (a) preparation and carbonization process for the LFP NP@NC@RGO composites. (b) Li$^+$ ion diffusion and electron transfer pathway.

2.2, LFP NP particles act as spacers between the RGO layers, which increase the surface area of RGO. Furthermore, N-doped carbon coated LFP NP particles are anchored to the RGO, resulting in fast electron transport between particles, as illustrated in Figure. 2.1.(b).

To investigate the morphology and microstructure of the as-prepared composites, FE-SEM and HR-TEM measurements were conducted. Figure 2.3. shows the FE-SEM image of the as-synthesized LFP NP@RGO, LFP NP@NC, and LFP NP@NC@RGO composites. Furthermore, EDS mapping images are shown in Figures 2.4.-2.7. Figure 2.8. shows that the bare LFP nanoplate (LFP NP) particles of 100–200 nm in length, 50–150 nm in width were prepared. The LFP NPs in both LFP NP@NC and LFP NP@NC@RGO composites (shown in Figures 2.3.b and c and Figure 2.8.) have similar morphologies and particle sizes
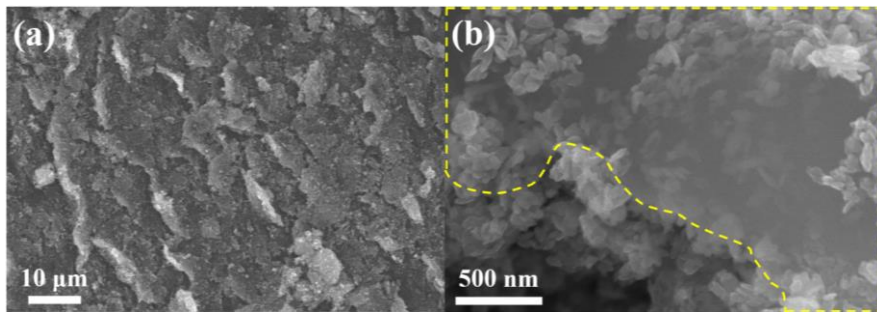
Figure 2.2. Low magnification SEM image (a), high magnification SEM image (b) of LFP NP@NC@RGO.

to those of bare LFP NP, whereas the LFP NP in LFP@RGO composite (in Figure 2.3.a and Figure 2.9.) is aggregated and enlarged. This result demonstrates that a uniform polydopamine layer prevented particle aggregation during heat treatment. Figures 2.3.a and (c) inset images show that LFP NP@RGO and LFP NP@NC@RGO composites are anchored on the RGO. As shown in the HR-TEM images in Figures 2.3.e–f, LFP NP@NC and LFP NP@NC@RGO were uniformly coated with N-doped carbon (NC) layers. As shown in Figure 2.3.f, it is difficult to distinguish the NC layer and RGO layer because the N-doped carbon layers appear similar to graphitic RGO layers.
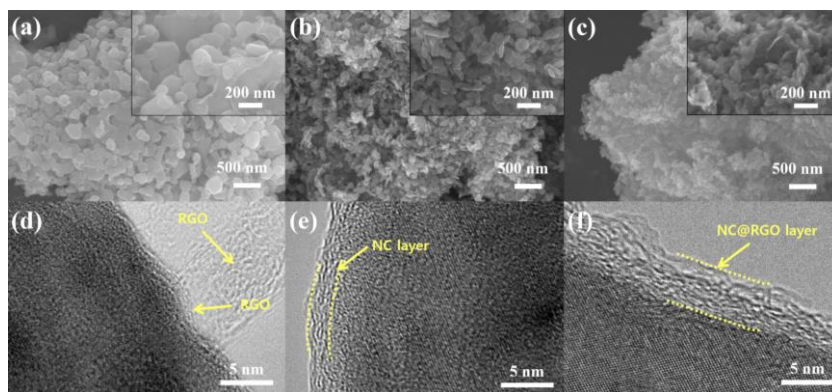
Figure 2.3. FE-SEM images of (a) LFP NP@RGO, (b) LFP NP@NC, and (d) LFP NP@NC@RGO composite. Inset: magnified FE-SEM images of samples. HR-TEM images of (d) LFP NP@RGO, (e) LFP NP@NC, and LFP NP@NC@RGO composites.
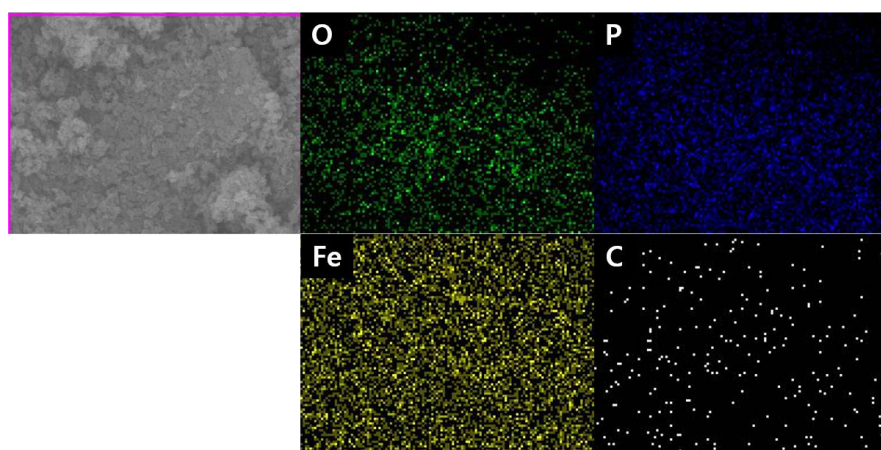
Figure 2.4. EDS mapping images of bare LFP NP.
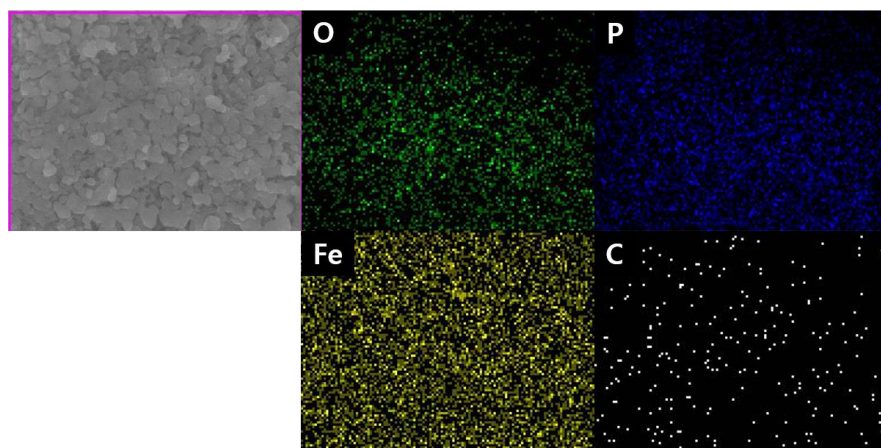
Figure 2.5. EDS mapping images of LFP NP@RGO.
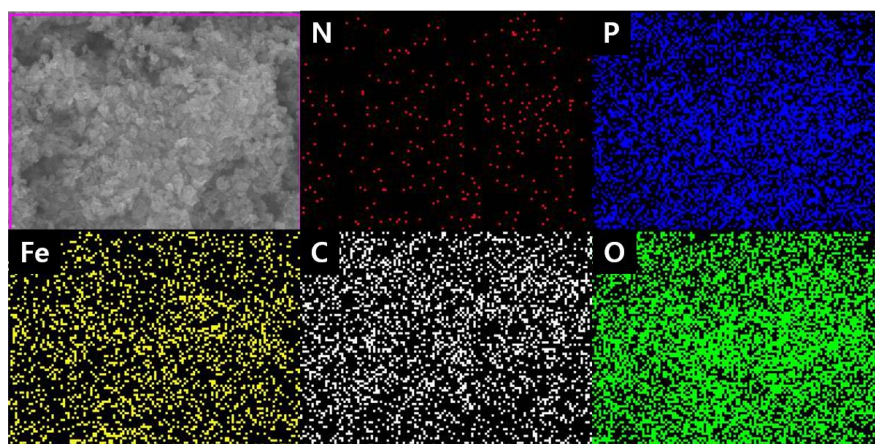
Figure 2.6. EDS mapping images of LFP NP@NC.
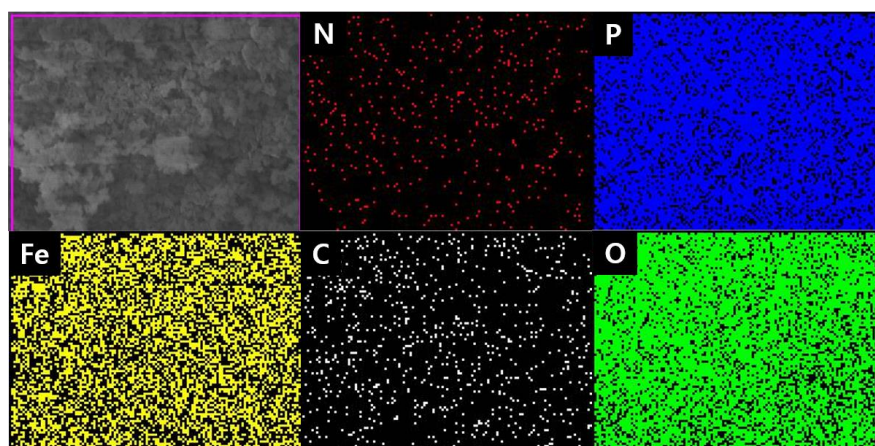
Figure 2.7. EDS mapping images of LFP NP@NC@RGO.
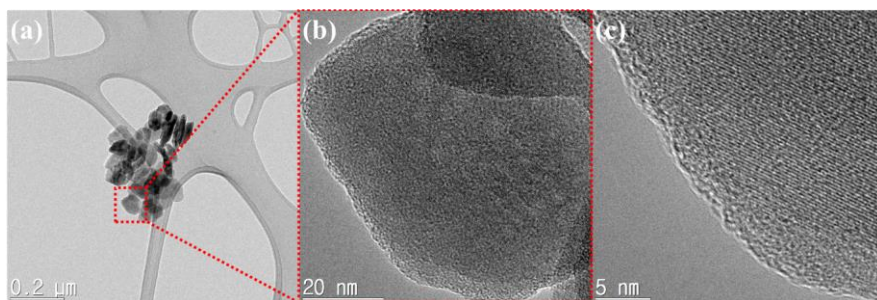
Figure 2.8. TEM images of (a) LFP NP, (b) low magnified image of selected area, and (c) high magnified image of selected area.
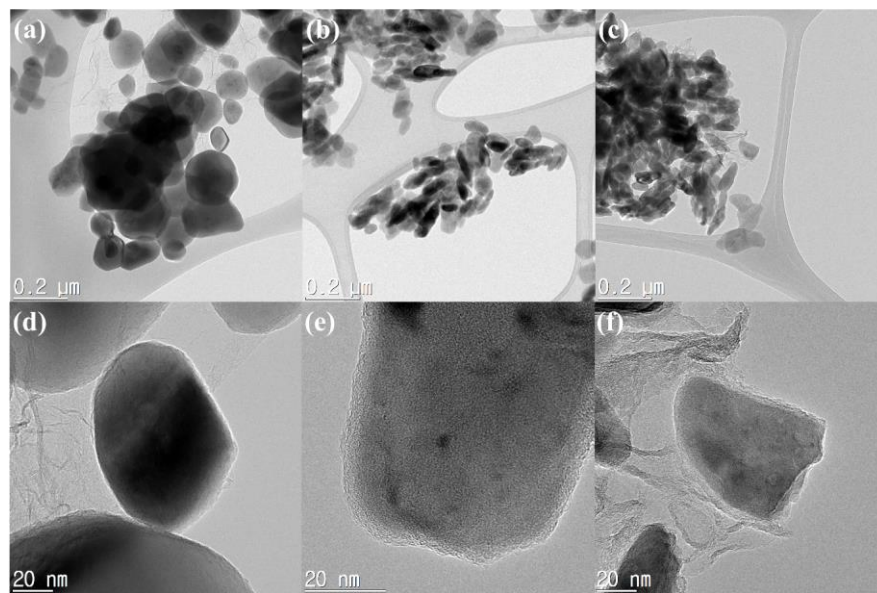
Figure 2.9. TEM images of (a) bare LFP NP, (b) low magnified image of selected area, and (c) high magnified image of selected area.
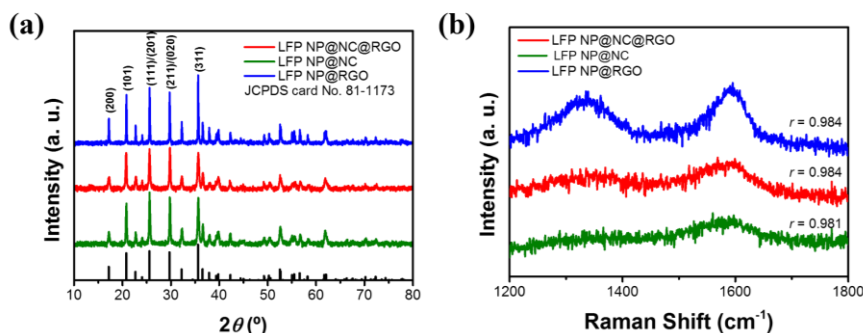
Figure 2.10. (a) XRD patterns of LFP NP@RGO, LFP NP@NC, and LFP NP@NC@RGO samples, and (b) Raman spectra of same samples.
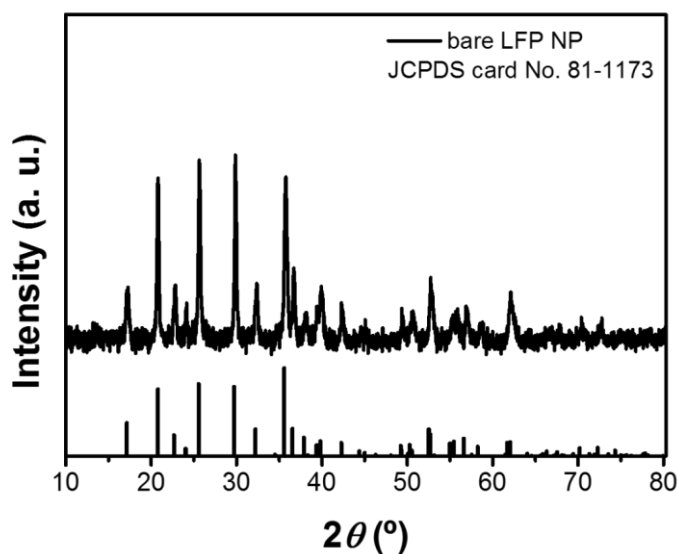
Figure 2.11. XRD pattern of bare LFP NP.

The as-prepared bare LFP NP, LFP NP@RGO, LFP NP@NC, and LFP NP@NC@RGO composites were characterized by XRD (Figure. 2.10.a and Figure 2.11.). All diffraction peaks were indexed to the orthorhombic

space group of Pnma (JCPDS card no 81-1173), indicative of olivine LFP. No impurity peaks are present. The sharp diffraction peaks suggest that the LFP NP particles are very crystalline, indicating that RGO and/or N-doped carbon does not affect the LFP crystal structure. There were no other peaks indicative of reduced graphene oxide, suggesting that the graphene (002) peak ($2\theta = 23°$)[39] is hidden behind the LFP (111) peak. Furthermore, carbon contents of all three samples are measured by TGA analysis (Figure 2.12.). LiFePO$_4$ has been completely oxidized to
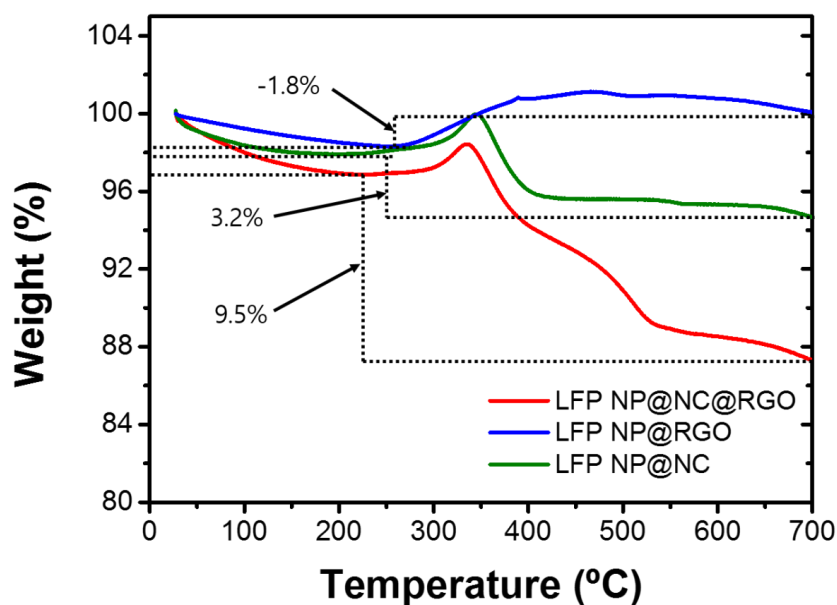
Figure 2.12. TGA analysis of LFP NP@RGO, LFP NP@NC, and LFP NP@NC@GO with temperature range from 25 to 700 °C under air flow.

$Li_3Fe_2(PO_4)_3$ and Fe_2O_3 phases, which lead to weight increase of 5.03%.[36] The carbon contents of LFP NP@RGO, LFP NP@NC, and LFP NP@NC@RGO are calculated to be 3.23%, 8.23%, and 14.54%, respectively. To further analyze the carbon structure of the samples, we used Raman spectroscopy. Spectra of RGO, LFP NP@RGO, LFP NP@NC, and LFP NP@NC@RGO (Figure 2.10.b and Figure 2.13.) contain broad peaks in the ranges of 1300–1400 and 1550–1650 cm^{-1} related to carbon material, which are attributed to disordered graphitic carbon (D, disordered peak) and ordered graphitic carbon (G, graphitic peak), respectively. Typically, the intensity ratio between the D and G
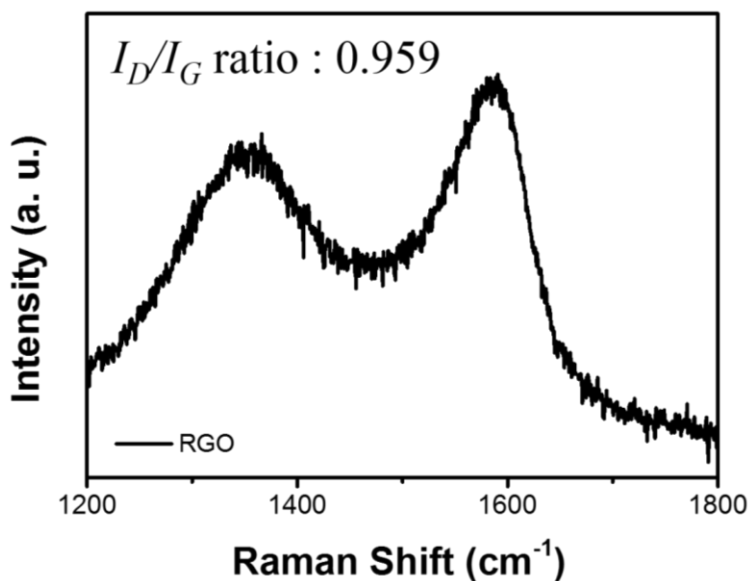
Figure 2.13. Raman spectrum of RGO.

peaks (I_D/I_G) is used to evaluate the degree of graphitization of carbon. In this case, it is not easy to calculate the value of I_D/I_G ratio for LFP NP@NC@RGO and LFP NP@NC samples because the peak intensity is too low to be clearly defined. This is attributed to high hydrogen content. It is known that it is difficult to obtain the obvious Raman peaks from a sample that has high hydrogen content.[40, 41] LFP NP@RGO shows higher peak intensity than LFP NP@NC and LFP NP@NC@RGO. The result from Elemental Analysis (in Table 2.1.) shows that LFP NP@RGO has least hydrogen content (0.09 wt %) among samples. Thus Raman spectra is in agreement of Elemental Analysis result. Even though the peak intensity is low, we can confirm that the carbon layers from polydopamine and reduced GO by heat treatment have the graphitic

Table 2.1. Elemental analysis of LFP NP@RGO, LFP NP@NC, and LFP NP@NC@RGO samples.

Sample	Elemental ratio (wt %)			
	C	H	N	O
LFP NP@RGO	1.6	0.09	0.03	19.3
LFP NP@NC	6.6	0.29	0.5	27.2
LFP NP@NC@RGO	9.4	0.28	0.7	24.8

properties.

The chemical state of the atoms in samples were identified by deconvolution of the C1s (Figures 2.14.a–c) and N1s (Figures 2.14.d–f) XPS spectra of LFP NP@RGO, LFP NP@NC, and LFP NP@NC@RGO. The C1s spectra of the samples can be deconvoluted into five peaks at 282.8 eV (Fe_xC),[42] 284.5 eV (C-C/C=C), 286.1 eV (C-O/C=O), 286.3 (C-N), and 288.5 eV (O-C=O), as shown in Figures. 2.14.a–c. Interestingly, there is a new peak near 282.8 eV in the LFP@RGO sample (Figure 2.14.a), which might arise from iron carbide species ($Fe_xC = Fe_3C, Fe_2C$) formed by Fe^{3+} impurities during the thermal treatment.[43-45] The XRD patterns show no impurity peaks related to iron
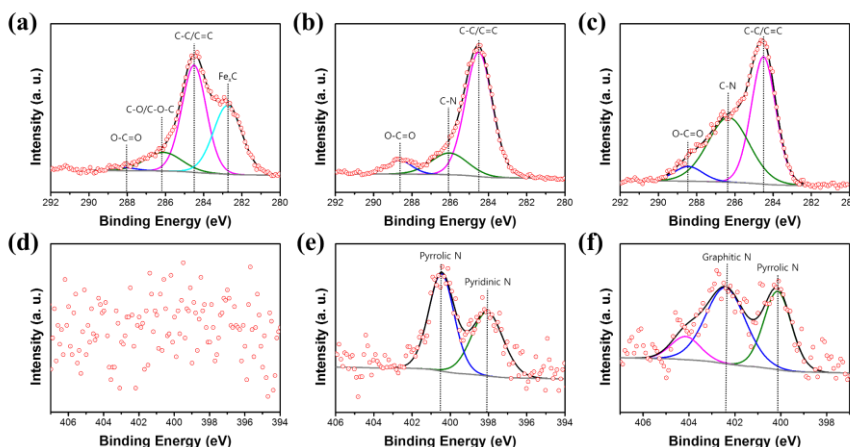
Figure 2.14. C1s XPS spectra of (a) LFP NP@RGO, (b) LFP NP@NC, and (c) LFP NP@NC@RGO, and N1s XPS spectra of (d) LFP NP@RGO, (e) LFP NP@NC, and (f) LFP NP@NC@RGO.

carbide species, suggesting that the amount of carbide species is too low to be detected by this method. In contrast, no peaks attributed to iron carbide peak were found in the XPS spectra of LFP NP@NC and LFP NP@NC@RGO (Figures 2.14.b and c, respectively). As shown in Figure 2.15., Fe2p spectra of all three samples are split in two parts because of spin-orbits splitting (Fe2p$_{3/2}$ and Fe2p$_{1/2}$). If Fe^{3+} exists, a new peak appears around Fe2p$_{1/2}$ and Fe2p$_{3/2}$ peak.[46, 47] In this case, we cannot
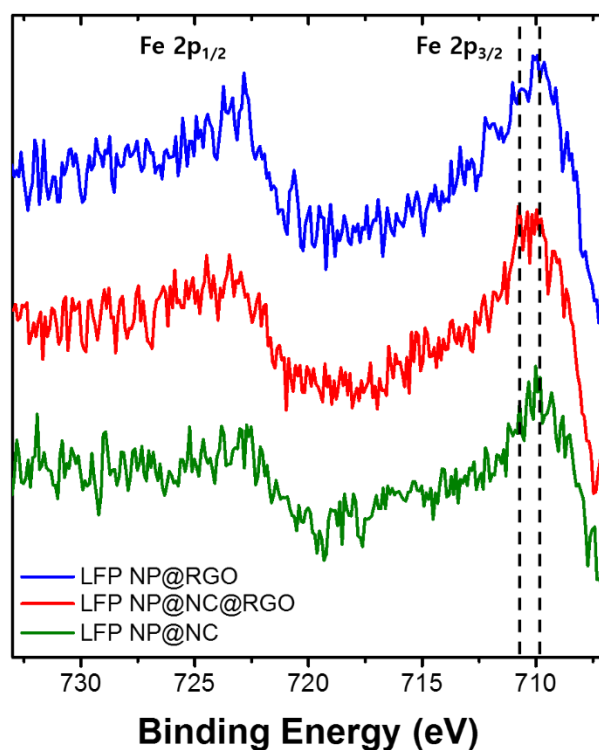
Figure 2.15. Fe2p XPS core peaks obtained from LFP NP@RGO, LFP NP@NC, and LFP NP@NC@RGO

define the Fe^{3+} peak around $Fe2p_{1/2}$ peak, because the intensity of $Fe2p_{1/2}$ is too low. However, the $Fe2p_{3/2}$ spectrum of LFP NP@NC@RGO and LFP NP@RGO displays a new peak at 711-712 eV which is characteristic of Fe^{3+}. Thus other impurity phases can exist in LFP NP@NC@RGO and LFP NP@RGO samples. In addition, all the peaks related to C and O bonds in each sample are smaller than the C-C/C=C bond peak, indicating that GO was reduced during the thermal treatment process. This result well matches the results from the Raman spectra. Notably, the peaks near 286.3 eV in the LFP NP@NC and LFP NP@NC@RGO (Figure 2.14.c) samples clearly demonstrate the existence of N-doped carbon layer.

Figures 2.14.d–f show the deconvoluted N1s XPS spectra of LFP NP@RGO, LFP NP@NC, and LFP NP@NC@RGO. In the case of LFP@RGO (Figure 2.14.d), there are no nitrogen atom related peaks. In contrast, in the spectra of LFP NP@NC (Figure 2.14.e) and LFP NP@NC@RGO (Figure 2.14.f), peaks are present at 398.1 eV due to the pyridinic N, near 400 eV due to pyrrolic N, and at 402.4 eV due to graphitic N.[48] For LFP NP@NC@RGO (Figure 2.14.f), a new peak detected at 404.1 eV is correspond to charging effects of positive charge localization in heterocycles.[49, 50] Therefore, all evidence indicates that

the LFP NP particles in the LFP NP@NC@RGO composite were well coated with N-doped carbon and RGO.

Figures 2.16.a and b show the electrochemical performance of LFP NP@RGO, LFP NP@NC, and LFP NP@NC@RGO. For comparison, the initial charge/discharge profiles of samples, of the LFP NP@RGO, LFP NP@NC, and LFP NP@NC@RGO composites at 0.5 C rate in the potential range of 2.0–4.2 V were tested, as shown in Figure 2.16a. All three samples contain a flat potential plateau around 3.4–3.5 V, indicative of a typical two-phase Fe^{2+}/Fe^{3+} redox process. The initial discharge capacity of LFP NP@NC@RGO was 140 mAh g^{-1}, higher than those of LFP NP@RGO (116 mAh g^{-1}) and LFP NP@NC (132 mAh g^{-1}). The
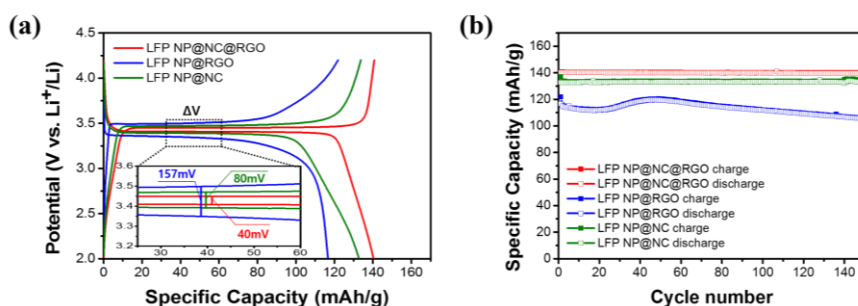
Figure 2.16. Initial charge/discharge profiles of the LFP NP@RGO, LFP NP@NC, and LFP NP@NC@RGO (a). Inset: potential difference between the charge/discharge plateaus. Cycling performances of LFP NP@RGO, LFP NP@NC, and LFP NP@NC@RGO (b). Electrochemical tests for the samples were conducted at 0.5 C.

potential difference between charge/discharge plateaus of LFP NP@RGO, LFP NP@NC, and LFP NP@NC@RGO are 157, 80, and 40 mV, as shown in the inset of Figure 2.16.a. Furthermore, the charge/discharge potential plateau of LFP NP@NC@RGO was more stable than those of LFP NP@RGO and LFP NP@NC. These results indicate that LFP NP particles in LFP NP@NC@RGO composite have shorter Li^+ diffusion pathways and enhanced electron transport properties. To further investigate the electrode, differential capacity vs. potential (dQ/dV) plots for the three samples are shown in Figure 2.17. As shown in Figure 2.17., dQ/dV curves of these three samples clearly show an oxidation and reduction peak in the potential range of 2.0–4.2 V at a rate of 0.5 C, indicative of the $LiFePO_4$/$FePO_4$ two-phase reaction.
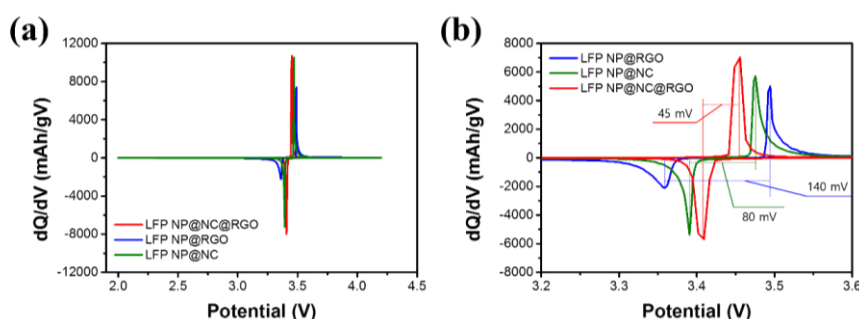
Figure 2.17. (a) Differential capacity vs. potential (dQ/dV) plots of LFP NP@RGO, LFP NP@NC, and LFP NP@NC@RGO at initial cycle; (b) magnified image of selected voltage range.

There are no other oxidation/reduction peaks. To clearly distinguish the peak position, selected regions of the curves were magnified (Figure 2.17.b). The peak positions are different and the peak potential difference of LFP NP@NC@RGO was 46 mV, which was lower than LFP NP@RGO (135 mV), and LFP NP@NC (84 mV). The lower difference in peak potential is indicative of the lower polarization and good reversibility of the electrode, resulting from the improved LFP NP electrochemical kinetics arising from the small size of the active materials and the uniformly interconnected carbon structure.

Figure 2.16.b shows the cycling performance of LFP NP@RGO, LFP NP@NC, and LFP NP@NC@RGO composites at a rate of 0.5 C. The discharge capacities of the samples were comparatively constant over 150 cycles. After the 150 cycle, the discharge capacity retention of the LFP NP@RGO was 90.32% of the initial value. In addition, the discharge capacities of LFP NP@NC and LFP NP@NC@RGO samples were 100.23% and 99.62%, respectively. The capacity fading of LFP NP@RGO (~10% loss of capacity) can be attributed to side reactions between the LFP NP particles and electrolyte, which results in poor cyclability. Meanwhile, the LFP NP particles in LFP NP@NC and LFP NP@NC@RGO result in good cyclability because carbon coating

prevents unwanted side reactions. These results suggest that the incorporation of RGO in LFP NP is not an efficient way to enhance the cyclability.

The electrochemical performance, including initial galvanostatic charge/discharge profiles at various C-rates, rate performances, and long-term cycling performances of LFP NP@RGO, LFP NP@NC, and LFP NP@NC@RGO are shown in Figure 2.18. The LFP NP@RGO sample delivers the specific discharge capacities of 149, 143, 112, 78, 62, 45, and 28 mAh g^{-1} at rates of 0.1 C, 0.2 C, 1 C, 5 C, 10 C, 20 C, and 30 C, respectively. In the case of LFP NP@NC electrode, the specific discharge capacities were 144, 141, 133, 114, 99, 69, and 4 mAh g^{-1} at rates of 0.1 C, 0.2 C, 1 C, 5 C, 10 C, 20 C, and 30 C, respectively. LFP NP@NC exhibits higher discharge capacities and lower polarization than those of the LFP NP@RGO sample between 0.1 C and 20 C, while LFP NP@NC electrode shows the lower discharge capacities and higher polarization than LFP NP@RGO sample at a high rate. This result indicates that the LFP NP@NC particles were connected in point-to-point mode, which is an unfavorable contact mode at high C-rates due to the low contact area. In comparison to LFP NP@NC particle, LFP NP particles in LFP NP@RGO composites have large contact area with

RGO, which reduces the contact resistance between LFP NP and RGO, and thus enhances rate performance. In contrast, the LFP NP@NC@RGO sample delivered specific discharge capacities of 146, 144, 138, 129, 121, 109, and 98 mAh g^{-1} at rates of 0.1 C, 0.2 C, 1 C, 5 C, 10 C, 20 C, and 30 C, respectively. These results show that the LFP NP@NC@RGO electrode has a higher discharge capacity and a more stable charge/discharge plateau than LFP NP@RGO and LFP NP@NC electrodes at various C-rates. The N-doped carbon enhances the electronic conductivity of LFP NP particles, and RGO enhances the electronic conductivity between LFP NP@NC particles.
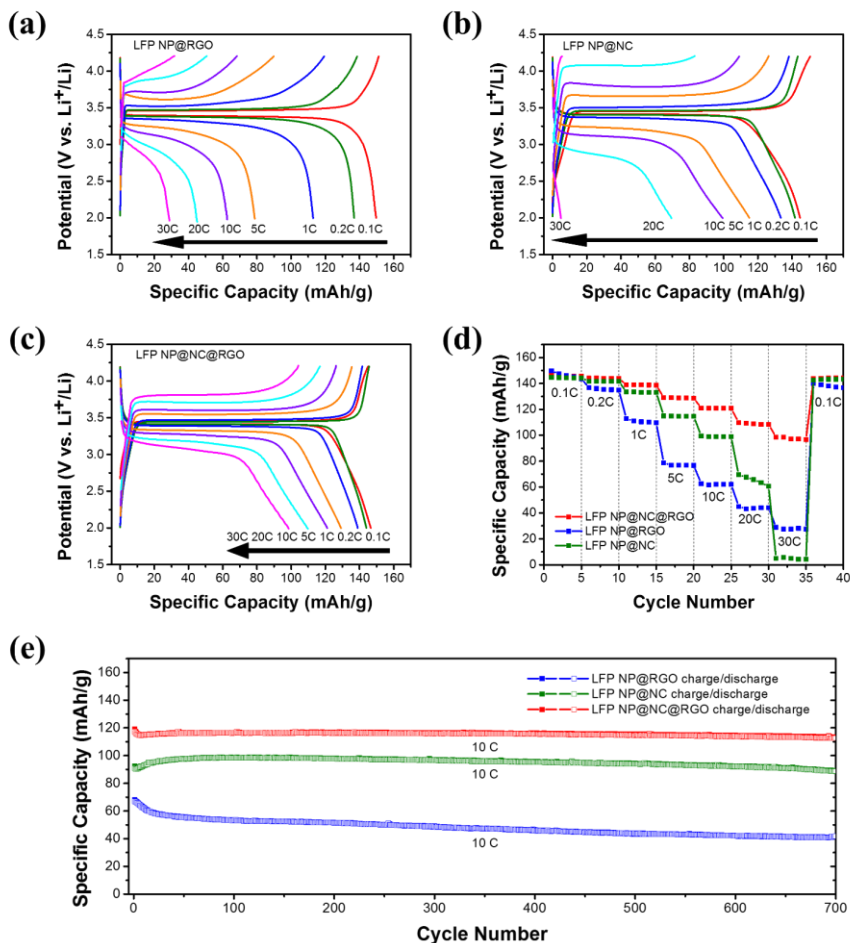
Figure 2.18. Initial galvanostatic charge/discharge profiles of the LFP NP@RGO (a), LFP NP@NC (b), and LFP NP@NC@RGO (c) in the potential window 2.0–4.2 V at various rates between 0.1 C and 60 C, respectively. Rate capabilities of the LFP NP@RGO, LFP NP@NC, and LFP NP@NC@RGO (d). Cycling performance of LFP NP@RGO, LFP NP@NC, and LFP NP@NC@RGO extended to 700 charge/discharge cycles at 10 C.

Furthermore, the N-doped carbon layer helps the LFP NP particles retain their morphology, reducing the Li^+ diffusion path. To further investigate the rate performance, the rate performance test was operated by charging and discharging five times at between 0.1 C and 30 C, as shown in Figure 2.18.d. The LFP NP@NC@RGO sample exhibits the stable cycling performance without capacity fading at various C-rates. LFP NP@RGO and LFP NP@NC samples show poor rate performance compared with LFP NP@NC@RGO electrode. The long-term cycling performance of all three samples at 10C is shown in Figure 2.18.d. LFP NP@RGO electrode shows the discharge capacity of 42 mAh g^{-1} after 700 cycles at 10 C with 62.2% capacity retention. The LFP NP@NC electrode has a discharge capacity of 89 mAh g^{-1} after 700 cycles at 10C with 97.7% capacity retention, while LFP NP@NC@RGO has a discharge capacity of 112 mAh g^{-1} after 700 cycles at 10 C with 96.2% capacity retention. From this result, uniform N-doped carbon layer contributes to cycle stability, which agrees well with the results shown in Figure 2.16.b.

To further understand the good electrochemical performance, electrochemical impedance spectroscopy was carried out, and the results are shown in Figure 2.19.a. The impedance spectra of LFP NP@RGO, LFP NP@NC, and LFP NP@NC@RGO show suppressed semicircles at high frequencies and sloped straight lines at low frequencies. The suppressed semicircle is likely to associate with contact resistance between particles and at the electrode-electrolyte interface.[51, 52] Noticeably, the semicircle diameters of the LFP NP@RGO and LFP NP@NC@RGO electrode are smaller than that of the LFP NP@NC electrode. Furthermore, in comparison with that of LFP NP@RGO, the semicircle diameter of LFP NP@NC@RGO is smaller. This result means
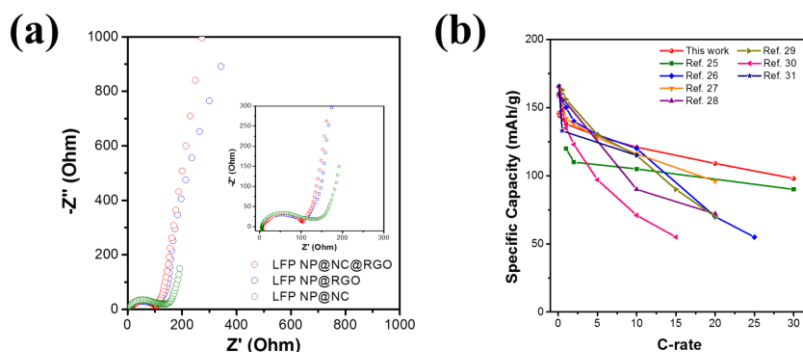
Figure 2.19. (a) Nyquist plot of the LFP NP@RGO, LFP NP@NC, and LFP NP@NC@RGO electrodes. (b) Comparison of the rate capability between LFP NP@NC@RGO and other graphene based LFP composite electrodes previously published.

that RGO based carbon structure contributes to reducing the inter-particle resistance, and N-doped carbon layers lead to a well-connected structure between the RGO and active materials, and this is reflected in Figure 2.19.a. The impressive rate performance is attributed to the synergetic effect between N-doped carbon and RGO. Figure 2.19.b compares the rate capability between the LFP NP@NC@RGO and other previously published $LiFePO_4$/graphene composites.[53-59] The N-doped carbon coated $LiFePO_4$/RGO composites show better electrochemical performance than other $LiFePO_4$/graphene composites, which might be ascribed to the synergistic effect between the uniformly coated N-doped carbon and graphene.

2.4. Conclusion

LFP NP and RGO composites uniformly coated with N-doped carbon were prepared by a one-pot polymerization process followed by heat treatment. The as-prepared LFP NP@NC@RGO composites show good electrochemical performance with remarkable rate performance and cycling performance at high C-rates. This performance can be ascribed to several reasons. First, the multifunctional role of polydopamine, which includes (1) preventing the LFP NP particle agglomeration, (2) enhancing the conductivity by uniform N-doped carbon coating of each particle, and (3) reducing the contact resistance between the LFP NP particles and RGO. Second, fast electron transport because of the RGO interconnected structure. The synergistic effect between the N-doped carbon and RGO enhances the electrochemical performance compared to LFP NP@NC and LFP NP@RGO. These are favorable factors for EV and HEV applications. Consequently, the polydopamine derived N-doped carbon and RGO carbon structure can be used to enhance the electronic conductivity of advanced cathode materials.

2.5. References

1.   Padhi, A. K.;   Nanjundaswamy, K. S.; Goodenough, J. B., Phospho-olivines as positive-electrode materials for rechargeable lithium batteries. *J. Electrochem. Soc*. **1997**, *144* (4), 1188-1194.

2.   Yamada, A.;   Chung, S. C.; Hinokuma, K., Optimized $LiFePO_4$ for lithium battery cathodes. *J. Electrochem. Soc*. **2001**, *148* (3), A224-A229.

3.   Padhi, A. K.;   Nanjundaswamy, K. S.;   Masquelier, C.; Okada, S.; Goodenough, J. B., Effect of structure on the Fe^{3+}/Fe^{2+} redox couple in iron phosphates. *J. Electrochem. Soc*. **1997**, *144* (5), 1609-1613.

4.   Andersson, A. S.;   Thomas, J. O.;   Kalska, B.; Haggstrom, L., Thermal stability of $LiFePO_4$-based cathodes. Electrochem. *Solid-State Lett*. **2000**, *3* (2), 66-68.

5.   Lu, L. G.;   Han, X. B.;   Li, J. Q.;   Hua, J. F.; Ouyang, M. G., A review on the key issues for lithium-ion battery management in electric vehicles. *J. Power Sources* **2013**, *226*, 272-288.

6.   Swierczynski, M.;   Stroe, D. I.;   Stan, A. I.;   Teodorescu, R.; S. K, K., Lifetime Estimation of the Nanophosphate $LiFePO_4$/C Battery

Chemistry Used in Fully Electric Vehicles. *IEEE Trans. Ind. Appl*. **2015**, *51* (4), 3453-3461.

7. Chung, S. Y.; Bloking, J. T.; Chiang, Y. M., Electronically conductive phospho-olivines as lithium storage electrodes. *Nat. Mater*. **2002**, *1* (2), 123-128.

8. Nishimura, S.; Kobayashi, G.; Ohoyama, K.; Kanno, R.; Yashima, M.; Yamada, A., Experimental visualization of lithium diffusion in Li_xFePO_4. *Nat. Mater*. **2008**, *7* (9), 707-711.

9. Malik, R.; Burch, D.; Bazant, M.; Ceder, G., Particle Size Dependence of the Ionic Diffusivity. *Nano Lett*. **2010**, *10* (10), 4123-4127.

10. Wu, X. L.; Guo, Y. G.; Su, J.; Xiong, J. W.; Zhang, Y. L.; Wan, L. J., Carbon-Nanotube-Decorated Nano-$LiFePO_4$ @C Cathode Material with Superior High-Rate and Low-Temperature Performances for Lithium-Ion Batteries. *Adv. Energy. Mater*. **2013**, *3* (9), 1155-1160.

11. Ha, J.; Park, S. K.; Yu, S. H.; Jin, A.; Jang, B.; Bong, S.; Kim, I.; Sung, Y. E.; Piao, Y., A chemically activated graphene-encapsulated $LiFePO_4$ composite for high-performance lithium ion

batteries. *Nanoscale* **2013**, *5* (18), 8647-8655.

12.   Li, X. L.;   Li, T. T.;   Zhang, Y. L.;   Zhang, X. L.;   Li, H. Y.;
Huang, J. M., Graphene nanoribbon-wrapping LiFePO$_4$ by electrostatic
absorbing with improved electrochemical performance for rechargeable
lithium batteries. *Electrochim. Acta* **2014**, *139*, 69-75.

13.   Nan, C. Y.;   Lu, J.;   Li, L. H.;   Li, L. L.;   Peng, Q.; Li, Y. D.,
Size and shape control of LiFePO$_4$ nanocrystals for better lithium ion
battery cathode materials. *Nano Research* **2013**, *6* (7), 469-477.

14.   Burch, D.; Bazant, M. Z., Size-Dependent Spinodal and
Miscibility Gaps for Intercalation in Nanoparticles. *Nano Lett*. **2009**, *9*
(11), 3795-3800.

15.   Cho, M. Y.;   Kim, H.;   Kim, H.;   Lim, Y. S.;   Kim, K. B.;
Lee, J. W.;   Kang, K.; Roh, K. C., Size-selective synthesis of
mesoporous LiFePO$_4$/C microspheres based on nucleation and growth
rate control of primary particles. *J. Mater. Chem. A* **2014**, *2* (16), 5922-
5927.

16.   Li, Z. J.;   Peng, Z. Z.;   Zhang, H.;   Hu, T.;   Hu, M. M.;
Zhu, K. J.; Wang, X. H., [100]-Oriented LiFePO$_4$ Nanoflakes toward

High Rate Li-Ion Battery Cathode. *Nano Lett*. **2016**, *16* (1), 795-799.

17.   Lin, M.;   Chen, Y. M.;   Chen, B. L.;   Wu, X.;   Kam, K. F.;   Lu, W.;   Chan, H. L. W.; Yuan, J. K., Morphology-Controlled Synthesis of Self-Assembled $LiFePO_4$/C/RGO for High-Performance Li-Ion Batteries. *ACS Appl. Mater. Interfaces* **2014**, *6* (20), 17556-17563.

18.   Ma, Z. P.;   Shao, G. J.;   Fan, Y. Q.;   Wang, G. L.;   Song, J. J.; Liu, T. T., Tunable Morphology Synthesis of $LiFePO_4$ Nanoparticles as Cathode Materials for Lithium Ion Batteries. *ACS Appl. Mater. Interfaces* **2014**, *6* (12), 9236-9244.

19.   Amin, R.;   Lin, C. T.;   Peng, J. B.;   Weichert, K.;   Acarturk, T.;   Starke, U.; Maier, J., Silicon-Doped $LiFePO_4$ Single Crystals: Growth, Conductivity Behavior, and Diffusivity. *Adv. Funct. Mater*. **2009**, *19* (11), 1697-1704.

20.   Chen, M.;   Shao, L. L.;   Yang, H. B.;   Ren, T. Z.;   Du, G. H.; Yuan, Z. Y., Vanadium-doping of $LiFePO_4$/carbon composite cathode materials synthesized with organophosphorus source. *Electrochim. Acta* **2015**, *167*, 278-286.

21.   Hu, J.;   Jiang, Y.;   Cui, S.;   Duan, Y.;   Liu, T.;   Guo, H.;

Lin, L.; Lin, Y.; Zheng, J.; Amine, K.; Pan, F., 3D-Printed Cathodes of $LiMn_{1-x}Fe_xPO_4$ Nanocrystals Achieve Both Ultrahigh Rate and High Capacity for Advanced Lithium-Ion Battery. *Adv. Energy. Mater.* **2016**, 1600856.

22.   Arico, A. S.; Bruce, P.; Scrosati, B.; Tarascon, J. M.; Van Schalkwijk, W., Nanostructured materials for advanced energy conversion and storage devices. *Nat. Mater.* **2005**, *4* (5), 366-377.

23.   Rui, X. H.; Zhao, X. X.; Lu, Z. Y.; Tan, H. T.; Sim, D. H.; Hng, H. H.; Yazami, R.; Lim, T. M.; Yan, Q. Y., Olivine-Type Nanosheets for Lithium Ion Battery Cathodes. *ACS Nano* **2013**, *7* (6), 5637-5646.

24.   Wang, J. J.; Yang, J. L.; Tang, Y. J.; Li, R. Y.; Liang, G. X.; Sham, T. K.; Sun, X. L., Surface aging at olivine $LiFePO_4$: a direct visual observation of iron dissolution and the protection role of nano-carbon coating. *J. Mater. Chem. A* **2013**, *1* (5), 1579-1586.

25.   Chen, Z. H.; Dahn, J. R., Reducing carbon in LiFePO/C composite electrodes to maximize specific energy, volumetric energy, and tap density. *J. Electrochem. Soc.* **2002**, *149* (9), A1184-A1189.

26.   Wang, Y. G.; Wang, Y. R.; Hosono, E. J.; Wang, K. X.; Zhou, H. S.; The design of a LiFePO$_4$/carbon nanocomposite with a core-shell structure and its synthesis by an in situ polymerization restriction method, *Angew. Chem. Int. Ed.*, **2008**, *47* 7461-7465.

27.   Chen, Z. Y.; Zhu, H. L.; R. Fakir, S. Ji,; Linkov, V.; Influence of carbon sources on electrochemical performances of LiFePO$_4$/C composites, *Solid State Ionics*, **2008**, *179* 1810-1815.

28.   Milev, A.; George, L.; Khan, S.; Selvam, P.; Kannangara, G. S. K.; Li-ion kinetics in LiFePO$_4$/carbon nanocomposite prepared by a two-step process: The role of phase composition, *Electrochim. Acta*, **2016**, *209* 565-573.

29.   Doeff, M. M.; Hu, Y. Q.; McLarnon, F.; Kostecki, R.; Effect of surface carbon structure on the electrochemical performance of LiFePO4, Electrochem. *Solid-State Lett.*, **2003**, *6* A207-A209.

30.   Ai, K. L.;   Liu, Y. L.;   Ruan, C. P.;   Lu, L. H.; Lu, G. Q., Sp^2 C-Dominant N-Doped Carbon Sub-micrometer Spheres with a Tunable Size: A Versatile Platform for Highly Efficient Oxygen-Reduction Catalysts. *Adv. Mater.* **2013,** *25*, (7), 998-1003.

31.   Liu, Y. L.;   Ai, K. L.; Lu, L. H., Polydopamine and Its Derivative Materials: Synthesis and Promising Applications in Energy,

Environmental, and Biomedical Fields. *Chem. Rev.* **2014,** *114*, (9), 5057-5115.

32.   Lee, H.;   Dellatore, S. M.;   Miller, W. M.; Messersmith, P. B., Mussel-inspired surface chemistry for multifunctional coatings. *Science* **2007,** *318*, (5849), 426-430.

33.   Su, F. Y.;   You, C. H.;   He, Y. B.;   Lv, W.;   Cui, W.;   Jin, F. M.;   Li, B. H.;   Yang, Q. H.; Kang, F. Y., Flexible and planar graphene conductive additives for lithium-ion batteries. *J. Mater. Chem.* **2010,** *20*, (43), 9644-9650.

34.   Kim, J. Y.; Kotov, N. A., Charge Transport Dilemma of Solution-Processed Nanomaterials. *Chem. Mater.* **2014,** *26*, (1), 134-152.

35.   Ding, B.;   Tang, W. C.;   Ji, G.;   Ma, Y.;   Xiao, P. F.;   Lu, L.; Lee, J. Y., Ultrathin carbon nanopainting of LiFePO4 by oxidative surface polymerization of dopamine. *J. Power Sources* **2014,** *265*, 239-245.

36.   Dreyer, D. R.;   Park, S.;   Bielawski, C. W.; Ruoff, R. S., The chemistry of graphene oxide. *Chem. Soc. Rev.* **2010,** *39*, (1), 228-240.

37.   Mi, Y. J.;   Wang, Z. F.;   Liu, X. H.;   Yang, S. R.;   Wang, H. G.;   Ou, J. F.;   Li, Z. P.; Wang, J. Q., A simple and feasible in-situ reduction route for preparation of graphene lubricant films applied to a

variety of substrates. *J. Mater. Chem.* **2012,** *22*, (16), 8036-8042.

38.   Hong, S.;   Na, Y. S.;   Choi, S.;   Song, I. T.;   Kim, W. Y.; Lee, H., Non-Covalent Self-Assembly and Covalent Polymerization Co-Contribute to Polydopamine Formation. *Adv. Funct. Mater.* **2012,** *22*, (22), 4711-4717.

39.   Stobinski, L.;   Lesiak, B.;   Malolepszy, A.;   Mazurkiewicz, M.;   Mierzwa, B.;   Zemek, J.;   Jiricek, P.; Bieloshapka, I., Graphene oxide and reduced graphene oxide studied by the XRD, TEM and electron spectroscopy methods. *J. Electron Spectrosc.* **2014,** *195*, 145-154.

40.   Colomban, P.; Slodczyk, A., Raman Intensity: An Important Tool in the Study of Nanomaterials and Nanostructures. *Acta Phys. Pol. A* **2009,** *116*, (1), 7-12.

41.   Chu, P. K.; Li, L. H., Characterization of amorphous and nanocrystalline carbon films. *Mater. Chem. Phys.* **2006,** *96*, (2-3), 253-277.

42.   Chang, Y. H.;   Wu, J. B.;   Chang, P. J.; Chiu, H. T., Chemical vapor deposition of tantalum carbide and carbonitride thin films from $Me_3CE = Ta(CH_2CMe_3)(_3)$ (E = CH, N). *J. Mater. Chem.* **2003,** *13*, (2), 365-369.

43. Doeff, M. M.; Wilcox, J. D.; Kostecki, R.; Lau, G., Optimization of carbon coatings on LiFePO4. *J. Power Sources* **2006,** *163*, (1), 180-184.

44. Hong, S. A.; Kim, S. J.; Chung, K. Y.; Chun, M. S.; Lee, B. G.; Kim, J., Continuous synthesis of lithium iron phosphate (LiFePO4) nanoparticles in supercritical water: Effect of mixing tee. *J. Supercrit. Fluids* **2013,** *73*, 70-79.

45. Hong, S. A.; Kim, S. J.; Kim, J.; Lee, B. G.; Chung, K. Y.; Lee, Y. W., Carbon coating on lithium iron phosphate (LiFePO4): Comparison between continuous supercritical hydrothermal method and solid-state method. *Chem. Eng. J.* **2012,** *198*, 318-326.

46. Dedryvere, R.; Maccario, M.; Croguennec, L.; Le Cras, F.; Delmas, C.; Gonbeau, D., X-Ray Photoelectron Spectroscopy Investigations of Carbon-Coated LixFePO4 Materials. *Chem. Mater.* **2008,** *20*, (22), 7164-7170.

47. El Ouatani, L.; Dedryvere, R.; Siret, C.; Biensan, P.; Gonbeau, D., Effect of Vinylene Carbonate Additive in Li-Ion Batteries: Comparison of LiCoO2/C, LiFePO4/C, and LiCoO2/Li4Ti5O12 Systems. *J. Electrochem. Soc.* **2009,** *156*, (6), A468-A477.

48. Liu, Y. Y.; Gu, J. J.; Zhang, J. L.; Yu, F.; Dong, L. T.;

Nie, N.; Li, W., Metal organic frameworks derived porous lithium iron phosphate with continuous nitrogen-doped carbon networks for lithium ion batteries. *J. Power Sources* **2016,** *304*, 42-50.

49.   Yan, S. C.;   Li, Z. S.; Zou, Z. G., Photodegradation of Rhodamine B and Methyl Orange over Boron-Doped g-C_3N_4 under Visible Light Irradiation. *Langmuir* **2010,** *26*, (6), 3894-3901.

50.   Zhang, J. S.; Zhang, M. W.; Zhang, G. G.; Wang, X. C.; Synthesis of Carbon Nitride Semiconductors in Sulfur Flux for Water Photoredox Catalysis, *ACS Catal.*, **2012,** *2* 940-948.

51.   Zhang, S. S.; Foster, D.; Wolfenstine, J.; Read, J., Electrochemical characteristic and discharge mechanism of a primary Li/CF_x cell. *J. Power Sources* **2009,** *187*, (1), 233-237.

52.   Li, Y.;   Chen, Y. F.;   Feng, W.;   Ding, F.; Liu, X. J., The improved discharge performance of Li/CF_x batteries by using multi-walled carbon nanotubes as conductive additive. *J. Power Sources* **2011,** *196*, (4), 2246-2250.

53.   Luo, W. B.;   Chou, S. L.;   Zhai, Y. C.; Liu, H. K., Self-assembled graphene and $LiFePO_4$ composites with superior high rate capability for lithium ion batteries. *J. Mater. Chem. A* **2014,** *2*, (14), 4927-4931.

54.   Shen, W. Z.;   Wang, Y. M.;   Yan, J.;   Wu, H. X.; Guo, S. W., Enhanced Electrochemical Performance of Lithium Iron(II) Phosphate Modified Cooperatively via Chemically Reduced Graphene Oxide and Polyaniline. *Electrochim. Acta* **2015,** *173*, 310-315.

55.   Fei, H. L.;   Peng, Z. W.;   Yang, Y.;   Li, L.;   Raji, A. R. O.; Samuel, E. L. G.; Tour, J. M., $LiFePO_4$ nanoparticles encapsulated in graphene nanoshells for high-performance lithium-ion battery cathodes. *Chem. Commun.* **2014,** *50*, (54), 7117-7119.

56.   Zhang, Y.;   Wang, W. C.;   Li, P. H.;   Fu, Y. B.; Ma, X. H., A simple solvothermal route to synthesize graphene-modified $LiFePO_4$ cathode for high power lithium ion batteries. *J. Power Sources* **2012,** *210*, 47-53.

57.   Guo, X. K.;   Fan, Q.;   Yu, L.;   Liang, J. Y.;   Ji, W. X.; Peng, L. M.;   Guo, X. F.;   Ding, W. P.; Chen, Y. F., Sandwich-like $LiFePO_4$/graphene hybrid nanosheets: in situ catalytic graphitization and their high-rate performance for lithium ion batteries. *J. Mater. Chem. A* **2013,** *1*, (38), 11534-11538.

58.   Yang, J. L.;   Wang, J. J.;   Tang, Y. J.;   Wang, D. N.;   Li, X. F.;   Hu, Y. H.;   Li, R. Y.;   Liang, G. X.;   Sham, T. K.; Sun, X. L., $LiFePO_4$-graphene as a superior cathode material for rechargeable

lithium batteries: impact of stacked graphene and unfolded graphene. *Energy Environ. Sci.* **2013,** *6*, (5), 1521-1528.

59.   Zhang, Y. Z.;   Chen, L.;   Ou, J. K.;   Wang, J.;   Zheng, B. Z.;   Yuan, H. Y.;   Guo, Y.; Xiao, D., Improving the performance of a LiFePO$_4$ cathode based on electrochemically cleaved graphite oxides with high hydrophilicity and good conductivity. *J. Mater. Chem. A* **2013,** *1*, (27), 7933-7941.

Chapter 3. Melamine Foam derived N-doped carbon Framework and Graphene Supported LiFePO₄ Composite for High-performance Lithium-ion Battery Cathode Material

3.1. Introduction

The lithium-ion battery market is rapidly growing due to increasing consumer interest in EVs, smart grids, and other electronic devices. With this growth, lithium-ion battery technology is becoming increasingly important. Accordingly, it is necessary to further improve the performance of the battery to match the ever increasing market demands of higher stability, power density, energy density, and longer lifetime.[1-3] Olivine type lithium iron phosphate, $LiFePO_4$ (LFP), has been used as cathode material for LIB because of its high theoretical capacity (170 mAh g^{-1}), environmental friendliness, acceptable operation potential (3.4 V vs Li/Li^+), superior safety, and low material costs.[4, 5] Thus, LFP has been widely used in EVs and smart grids, but several critical issues remain to be solved, including its sluggish electron and Li ion transport.[6, 7] To overcome these challenges, several methods, such as coating,[8-11]

foreign metal doping,[12-14] and morphology controlling[15-17] have been attempted.

An effective method to improve Li ion diffusion and electron transport is to combine LFP particle size reduction and LFP particle coating with conductive carbonaceous material.[18, 19] However, this combined method suffers from issues related to the internal resistance of the electrode. Electrons can travel through the carbon layers, which represents a detour for the electrons between the active materials and current collector because a conductive network is not formed.[20, 21] Furthermore, the connectivity between the active materials is important because electrons travel between them.[22] It is also difficult to uniformly coat nanoparticles with carbon, and this prevents the active material from receiving electrons from all directions evenly and increases the internal resistance of the electrode.[23, 24]

Another factor that contributes to the internal resistance of an electrode is the ionic network between the active material and electrolyte. Many studies have reported that ionic transport is important in high rate charge/discharge processes.[25] Thus, many attempts have been made to enhance ionic transport kinetics by forming ionic networks through a porous structure.[26, 27] Melamine foams with porous structure are often

used as carbon precursors to form ionic networks. Furthermore, a conductive N-doped carbon framework can be easily generated after heat treatment. Lee et al. developed melamine foam derived porous and interconnected carbon structures for oxygen reduction.[28] Recently, Lee et al. used melamine foam to prepare a porous interconnected carbon structure for sulfur hosts in lithium-sulfur batteries.[29] Therefore, melamine foam has the potential to provide the efficient conductive network as well as the ionic network. However, melamine foam has not been utilized for LFP cathode material yet even though it has such potential.

In this study, LFP was anchored on a designed carbon structure consisting of a melamine foam derived N-doped carbon framework (NCF) and rGO, which was fabricated using polydopamine as binding agent and studied as cathode material for lithium ion battery. Melamine foams with porous structure are often used as carbon precursors to form ionic networks. Furthermore, a conductive NCF can be easily generated after heat treatment. The NCF provided space for the LFP particles to be attached as well as a conductive network. In addition, this carbon framework provided electronic conducting pathway and enhanced ionic transport. rGO, which wrapped the NCF, enhanced the connectivity

between the LFP and carbon structure. This NCFG-NCL composite demonstrated a high rate performance with a discharge capacity of 108 mAh g^{-1} at 20 C and good long-term cycling stability of 131 mAh g^{-1} at 2 C after 500 cycles. To confirm the effect of the carbon framework to the battery performance, several validation and control experiments were carefully performed.

3.2. Experimental Section

3.2.1. Chemicals

Dopamine hydrochloride, Tris-buffer, and lithium hydroxide monohydrate (LiOH•H$_2$O, 99%) were purchased from Sigma-Aldrich. Phosphoric acid (H$_3$PO$_4$, 85%) was purchased from ACROS. Iron sulfate heptahydrate (FeSO$_4$•7H$_2$O, 99%) was purchased from Alfa Aesar. Ethylene glycol (EG) was purchased from SAMCHUN. All chemicals were used without further purification.

3.2.2. Characterization methods

The crystallographic structures of the samples were identified by X-ray diffractometer (XRD; Bruker New D8 Advance, 40 kV, 40 mA, scan range 2θ= 10–80°) with Cu Kα radiation source. The morphology of

samples was characterized using field emission scanning electron microscopy (FE-SEM; Hitachi S-4800, 15 kV). The microscopic features of the samples were observed using high-resolution transmission electron microscopy (HR-TEM; JEOL JEM-2100F, 200 keV). Nitrogen adsorption/desorption isotherms were obtained using a BELSORP-mini II (MicrotracBEL Corp) instrument. The specific surface area was calculated using the Brunauer-Emmett-Teller (BET) method and the average pore diameter was calculated using the Barrett-Joyner-Halenda (BJH) method. X-ray photoelectron spectroscopy (XPS) was performed to characterize the surface chemical composition of the samples (Axis-HIS with Al irradiation at 12 kV and 18 mA at a constant pass energy of 20 eV). Raman spectroscopy was performed on a DXR2xi instrument. Thermogravimetric analysis (TGA) was performed using a TGA/DSC 1 analyzer (Mettler Toledo) over a temperature range of 25 to 700 °C with a ramp rate of 5 °C/min in air.

3.2.3. Preparation of $LiFePO_4$

LFP nanoparticles were prepared by solvothermal synthesis using lithium hydroxide monohydrate ($LiOH \cdot H_2O$, 99%), Phosphoric acid (H_3PO_4, 85%), and Iron sulfate heptahydrate ($FeSO_4 \cdot 7H_2O$, 99%) as

precursors in the stoichiometric ratio of 2.7:1:1.5, respectively. First, an appropriate quantity of LiOH•H_2O was dissolved in EG (45 mL). Then, H_3PO_4 was added dropwise into the above solution with vigorous stirring. FeSO$_4$•7H_2O was dissolved in ethylene glycol (30 mL). Subsequently, the LiOH•H_2O solution was added into the iron sulfate solution with stirring. The obtained olive green suspension was transferred into a Teflon-lined stainless steel autoclave and then heated at 180 °C for 10 h. After heating, the autoclave was cooled to room temperature. The obtained gray precipitates were washed with EtOH and DI water several times. Finally, the LFP residues were dried in the freeze drier.

3.2.4. Preparation of the N-doped framework and N-doped carbon framework@rGO (NCFG)

To synthesize the N-doped carbon framework (NCF), commercial melamine foam was heated at 700 °C for 2 h under an Ar atmosphere. After heat treatment, the white melamine foam was shrunk and formed black carbon structure. Graphene oxide (GO) was prepared using a modified Hummer's method.[30] For the fabrication of rGO coated structure on the NCF, a piece of melamine foam was repeatedly soaked in GO suspension (1 mg/mL) and dried for 30 min. The as-prepared

melamine foam with GO was dried using a freeze drier, and then heated at 700 °C for 2 h under Ar. After heat treatment, the generated rGO@NCF was seriously shrunk compared to the original materials and turned to black.

3.2.5. Preparation of N-doped carbon coated LFP (NCL), N-doped carbon framework@N-doped carbon coated LFP (NCF-NCL), and N-doped carbon framework@rGO@N-doped carbon coated LFP (NCFG-NCL)

The as-prepared LFP powder was dispersed in Tris-buffer solution (10 mM) by sonication. Subsequently, dopamine hydrochloride (3 mg/mL, 200 mL H_2O) was added to the suspension and stirred for 10 min. Then, NCFG (10 wt% in H_2O) was added to the LFP and dopamine suspension over 5 min. After reacting for 5 min, the suspension of LFP, dopamine, and NCFG was washed three times with DI water and dried in a freeze drier for 10 h. Finally, the collected LFP@polydopamine@NCFG (NCFG-PD@LFP) composite was calcined at 700 °C for 5 h in an Ar-filled Swagelok container to form NCF@rGO@NC-LFP (NCFG-NCL). For comparison, the NCF@NC-LFP (NCF-NCL) sample was also prepared under the same conditions without rGO. For preparation of

NCL, the LFP and dopamine suspension was stirred for 15 min.

3.2.6 Electrochemical characterization

The working electrode was prepared by mixing the as-prepared active materials, Super P (Timcal, carbon black), and poly(vinylidene fluoride) (PVDF) with N-methyl-2-pyrrolidone (NMP, Aldrich) in a weight ratio of 70:15:15, respectively. The mixed slurry was spread onto an aluminum foil current collector and dried before use. Subsequently, a coin type 2016 cell was assembled in an Ar-filled glove box with a lithium foil as the counter electrode and a Celgard 2450 membrane as the separator. The loading mass of the active material was ~1.5 mg cm^{-2}. The electrolyte was 1 M LiPF$_6$ in ethylene carbonate (EC) and diethyl carbonate (DEC) in a 1:1 v/v solvent mixture. Electrochemical tests were conducted using a WBCS3000S cycler (WonATech, Korea) within a potential window of 2.0–4.2 V vs. Li/Li$^+$. Electrochemical impedance spectroscopy (EIS) was measured using a ZIVE SP1 (WonATech, Korea) instrument at a frequency range of 100 kHz to 0.1 Hz with an amplitude of 10 mV. The electrochemical performance was calculated based on the total active material weight.

3.3. Results and Discussion
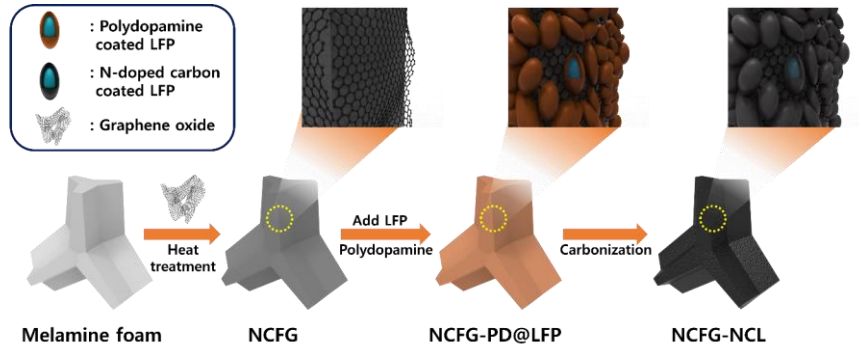
Figure 3.1. Schematic illustration of the synthesis of the NCFG-NCL sample.

The synthetic process for fabricating the NCFG-NCL sample is outlined in Figure 3.1. Briefly, GO was first entangled in the melamine foam frame through a simple soaking method. When the GO entangled melamine foam was heat-treated, GO was reduced and melamine foam carbonized to form NCFG. The NCF are very fragile and easily broken into small (micro-sized) pieces. Therefore, when using carbonized melamine foam as a carbon structure, the pieces of carbon framework can easily form appropriate pore spaces and achieve large specific surface areas.[31] The micro-sized pieces of the NCF provide sufficient surface area for LFP nanoparticle attachment, and the functional groups of rGO that wrapped the NCF can interact with the catechol and amine

groups of dopamine. Thus, the LFP nanoparticles were attached to the NCFG primarily through interactions with dopamine and formed the interconnected structure. Furthermore, LFP particle was uniformly coated with polydopamine. The NCFG-PD@LFP composite was thermally treated to obtain N-doped carbon from polydopamine and crystalline LFP and the final NCFG-NCL sample was obtained.

The structural information of the NCL, NCF-NCL, and NCFG-NCL
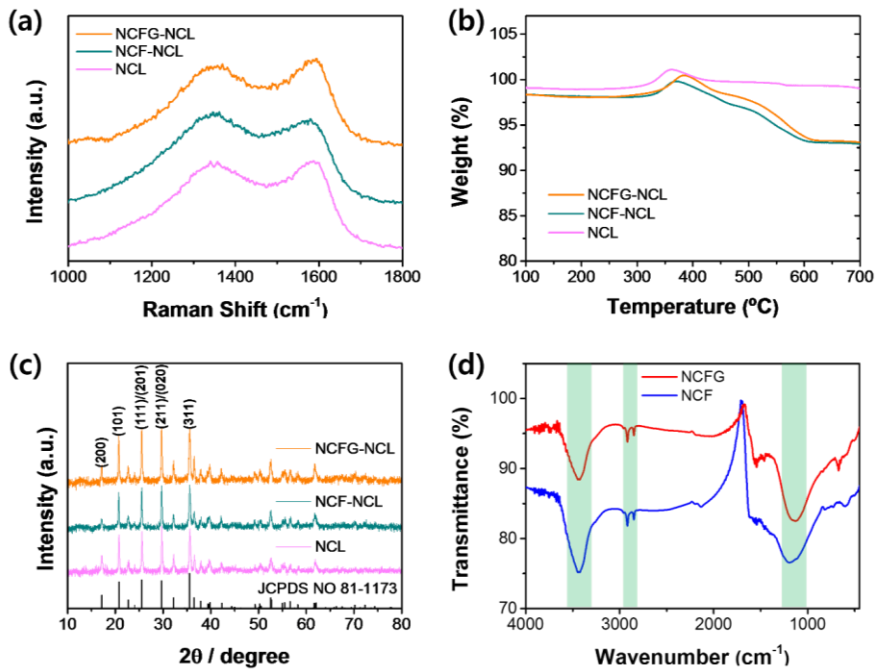
Figure 3.2. (a) Raman spectra, (b) TG analysis, and (c) XRD analysis of NCL, NCF-NCL, and NCFG-NCL samples. (d) FT-IR spectra of the NCF and NCFG samples.

samples were obtained using Raman spectroscopy (Figure 3.2.a). The bands observed at approximately 1350 and 1600 cm^{-1} were assigned to the disordered D and graphitic G bands of the carbon materials, respectively. The intensity ratio of the D and G bands can be used as an estimation of the disorder of the carbon materials (I_D/I_G). As shown in Figure 3.2.a, the I_D/I_G ratio of NCL, NCF-NCL, and NCFG-NCL was 0.99, 1.06, and 0.91, respectively. The carbon content in the samples was estimated by TGA analysis. The carbon contents of NCL, NCF-NCL, and NCFG-NCL were calculated from the curves shown in Figure 3.2.b. LFP can be oxidized to form new phases such as $Li_3Fe_2(PO_4)_3$ and Fe_2O_3, resulting in a weight increase of 5.03%.[32] Considering the oxidation of LFP, the carbon content of NCL, NCF-NCL, and NCFG-NCL were calculated to be 6.0%, 12.1%, and 11.9%, respectively. To determine the crystal structure and phase impurities in the as-prepared NCL, NCF-NCL, and NCFG-NCL samples, XRD analyses were conducted (Figure 3.2.c). The diffraction peaks of all these three samples were indexed to olivine LFP with the Pnma space group (JCPDS no 81-1173). No impurity peaks were observed in any of the samples. For NCFG-NCL, the rGO peak, which was assigned to the rGO (002) peak ($2\theta = 23°$), was not observed because it was hidden behind the LFP (111) peak. From these results, it

was confirmed that the sample preparation process had no effect on the LFP particles. Furthermore, FT-IR analysis was conducted to identify the surface functional groups on the NCF and NCFG samples (Figure 3.2.d). The strong peak at 3430 cm-1 arises from the O-H stretching vibration of H_2O in the NCF and NCFG samples. The peaks at 2920 and 2850 cm^{-1} were attributed to CH_2 asymmetric and C-H symmetric stretching vibrations, respectively. Furthermore, the broad peak between 1250 and 1000 cm^{-1} was attributed to the C-N bending vibration and C-O stretching vibration mode. The NCFG sample was shifted to a slightly lower wavenumber than the NCF sample. To figure out the reason for the peak shift of NCFG, compared to NCF, FT-IR analysis of rGO was also conducted (Figure 3.3.). The peaks at 1170 and 1056 cm^{-1} were attributed to the C-O stretching vibration mode and the epoxy or peroxide groups, respectively.[33] We believed that these peaks affect the peak position of NCFG to lower range wavenumber. Furthermore, many functional groups were present on the surface of NCF and NCFG that can interact
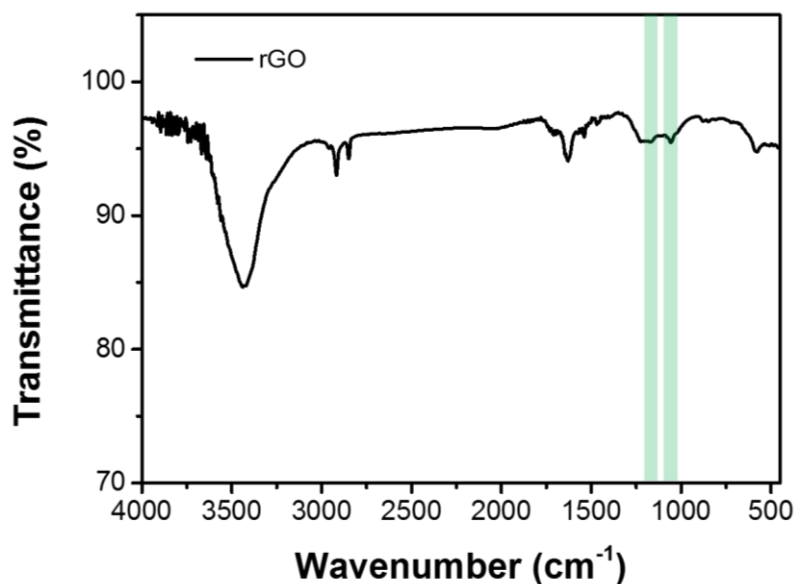
Figure 3.3. FT-IR spectra of rGO.

with dopamine, allowing LFP to adhere to the NCF and NCFG surface.

The morphology of NCL, NCF-NCL, and NCFG-NCL is shown in Figure 3.4. Figure 3.4.a and b show the morphology of NCL and the magnified images show that each LFP particle was unevenly aggregated. For NCF-NCL (Figure 3.4c and d), it was observed that the NCL particles were aggregated and formed a specific secondary particle shape. The morphology of the NCF sample was confirmed by SEM. The SEM images showed shapes similar to the secondary particles of the NCF-NCL composite, which are large chunks of NCF-NCL, as shown in Figure 3.4.c. Thus, it can be concluded that the NCL particles were well

attached to the NCF. For NCFG-NCL (Figure 3.4.e), as in NCF-NCL, the NCL particles agglomerated and formed NCF-shaped secondary particles. No size difference among the NCF, NCF-NCL, and NCFG-NCL samples was observed. This indicates that the NCL was uniformly and compactly attached to NCF (and NCFG) and formed the
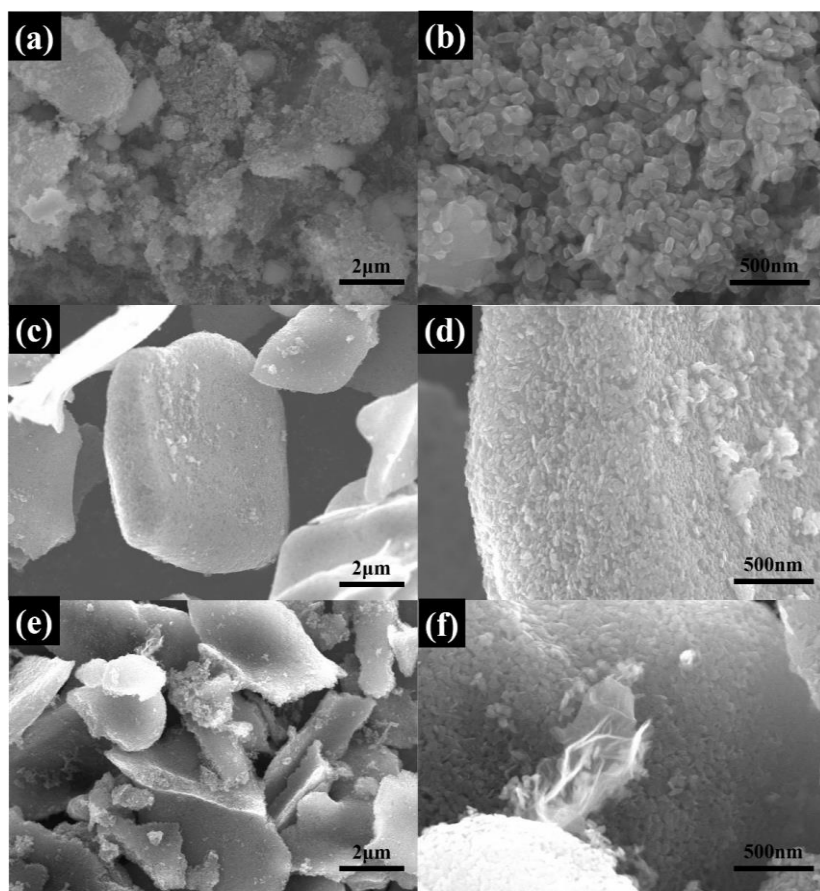
Figure 3.4. SEM images of the (a, b) NCL, (c, d) NCF-NCL, and (e, f) NCFG-NCL samples.

interconnected structure.   Furthermore, the NCF-NCL and NCFG-NCL samples contain pore spaces which were formed between the gaps of the NCF-shaped NCL secondary particles. However, it was difficult to confirm the morphology difference between NCFG-NCL and NCF-NCL. In Figure 3.5., most of rGO were observed to be entangled with NCF, forming the NCFG composite. The NCFG composite was well covered by the NCL particles, as the rGO was not frequently observed independently from the NCFG-NCL composite. Therefore, some rGO was observed between the NCL secondary particles (Figure 3.4.f), but the overall morphology of NCFG-NCL was similar to that of NCF-NCL
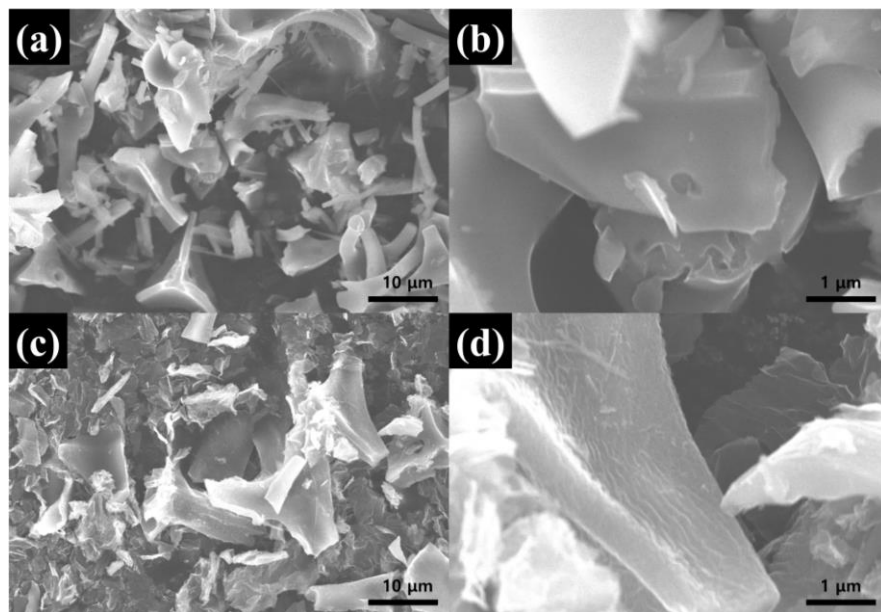
Figure 3.5. SEM images of (a, b) NCF, and (c, d) NCFG.

(Figure 3.6.).

The specific surface areas of bare LFP, NCL, NCF-NCL and NCFG-NCL were 44.8, 30.5, 46.5, and 44.2 m^2 g^{-1}, respectively (Table 3.1.). The specific surface areas of the prepared samples were observed to increase when the N-doped carbon framework was added. Interestingly, despite the introduction of rGO, with a large specific surface area compared to NCF, a similar specific surface area was observed for NCF-NCL and NCFG-NCL. This is likely because the rGO was entangled with the NCF surface and the NCL covered the rGO surface. This also confounded the SEM imaging of rGO as shown in Figure. 3.4. In addition, comparing the specific surface area of bare LFP with that of the NCL sample, the specific surface area of NCL was smaller. In addition, from the pore size distribution graph (Figure 3.7.), it was confirmed that
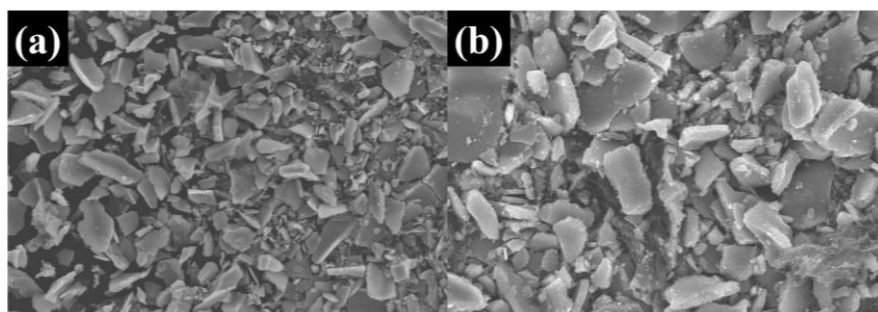
Figure 3.6. Low magnification SEM images of (a) NCF-NCL and (b) NCFG-NCL.

the NCL sample exhibited a smaller pore size than that of the bare LFP particles. The dopamine polymerization process likely aggregates the bare LFP particles.   However, when NCF is added, the pore size decreases and the specific surface area becomes larger. The results suggested that the LFP particles in the NCF-NCL and NCFG-NCL composites were uniformly and compactly attached to the carbon framework leading to increased specific surface area. Furthermore, smaller sized pores were formed between the uniformly attached NCL particles. On the other hand, NCFG-NCL and NCF-NCL have similar specific surface areas, but NCFG-NCL exhibited a smaller pore size. The BET results suggest that the NCL particles were compactly attached to the NCFG compared to the NCF structure due to the interaction between rGO and the polydopamine coated LFP particles. The structure where NCL is compactly attached to NCFG is electrochemically advantageous

Table 3.1. BET analysis of the as-synthesized NCL, NCF-NCL, and NCFG-NCL particles.

Sample	Bare LFP	NCL	NCF-NCL	NCFG-NCL
S_{BET} (m^2 g^{-1})	44.8	30.5	46.5	44.2
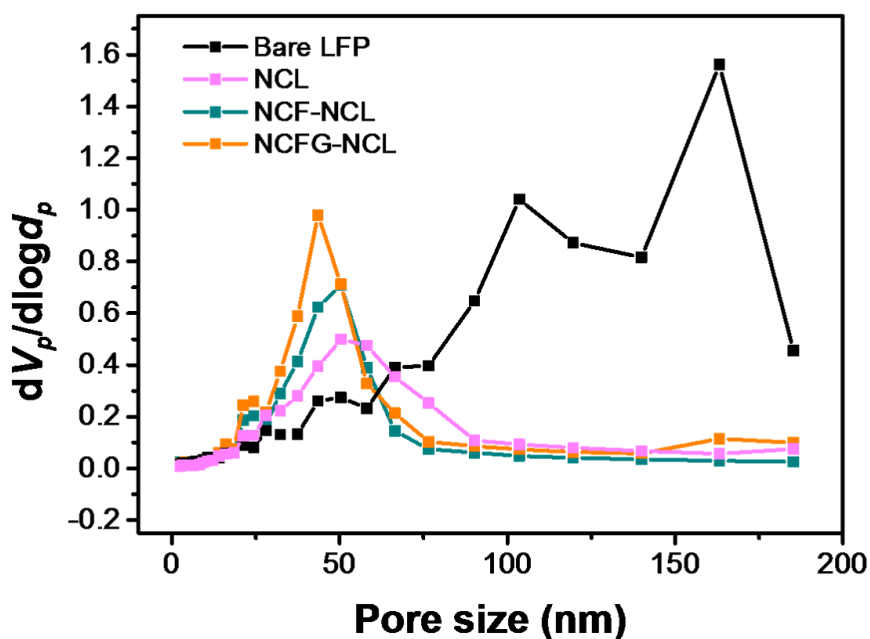
Figure 3.7. Pore size distribution of bare LFP, NCL, NCF-NCL, and NCFG-NCL.

because the electrolyte penetration distance is short. Also, tap density of NCFG-NCL and bare LFP was analyzed. The powder was transferred to a mass cylinder and tapped several hundred times. NCFG-NCL composite has higher tap density (0.86 g/cm^3) than bare LFP nanoparticles (0.59 g/cm^3). This result suggests that the improvement of tap density is attributed to the compactly attached LFP to the NCFG.

The microstructure characterization of the three samples was performed by TEM measurements (Figure 3.8.). Low and high magnification TEM images of each prepared sample were obtained. For
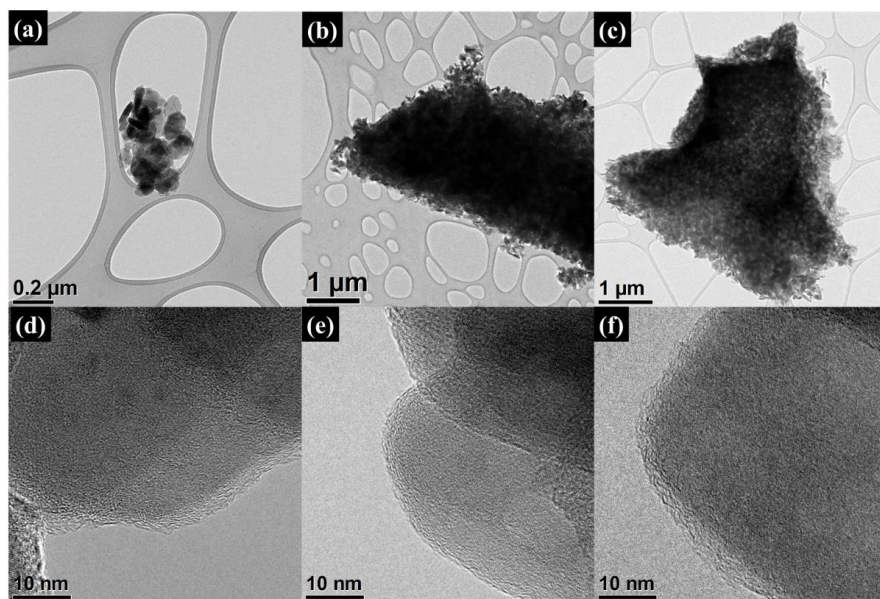
Figure 3.8. TEM and HRTEM images of the (a, b) NCL, (c, d) NCF-NCL, and (e, f) NCFG-NCL samples.

the NCL samples (Figure 3.8.a), TEM images showed that NCL particles were aggregated. On the other hand, in the NCF-NCL and NCFG-NCL samples (Figure 3.8.b and c) specific shaped micro-sized NCL secondary particles were observed. The specific shape of the micro-sized dark areas commonly observed at both NCL secondary particles originate from broken NCF fragments. In addition, the NCL particles were compactly attached along the micro-sized dark area. In the NCFG-NCL sample (Figure 3.8.c), it was also difficult to identify rGO, similar to the SEM analysis. In the magnified TEM image of all these three samples (Figures

3.8. d–f), carbon layers formed from polydopamine, which providing electrically conductive channel to LFP particles, were clearly observed.

XPS was performed to confirm the chemical state and composition in the NCL, NCF-NCL, and NCFG-NCL samples (Figure 3.9. and Figure 3.10.). The wide scan XPS survey spectrum of NCFG-NCL clearly indicated the presence of C, P, N, O, and Fe (Figure 3.9.a). To confirm the chemical state of each element, high resolution XPS spectra were deconvoluted.   The deconvolutions of the C1s spectra are shown in
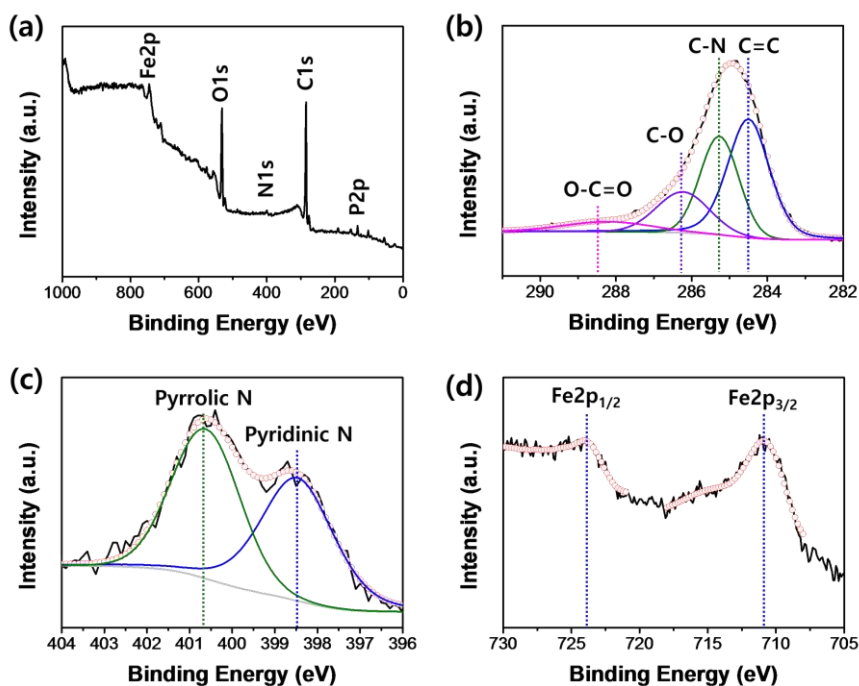
Figure 3.9. (a) XPS survey of NCFG-NCL. High resolution XPS spectra of (a) C1s, N1s, and Fe2p for the NCFG-NCL sample.

Figure 3.9.b. The peaks located at 284.5, 285.2, 286.2, and 288.2 eV were assigned to the C=C, C-N, C-O, and O-C=O functional groups, respectively.[34] These functional groups arose from the residual functional groups in NCFG. In Figure 3.9.c, the N1s spectra were deconvoluted into two peaks at 398.4 and 400.6 eV, which were assigned to pyridinic N and pyrrolic N, respectively.[35, 36] Similarly, for the NCF-NCL and NCL samples, pyridinic N and pyrrolic N peaks were observed (Figure 3.10).   The nitrogen peaks arose from the melamine foam and polydopamine, confirming that nitrogen was doped through C-N bond. Figure 3.9.d shows the Fe2p spectra of the NCFG-NCL sample. The
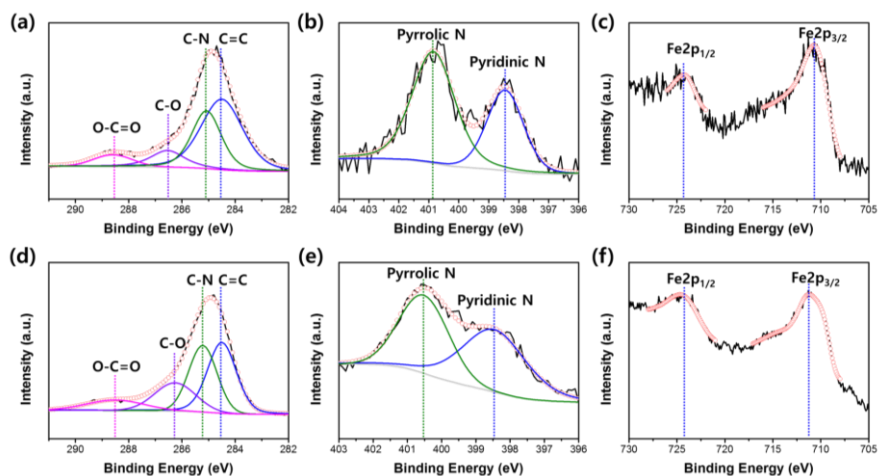
Figure 3.10. (a) C1s, (b) N1s, and (c) Fe2p deconvolution spectra of NCL composite and (d) C1s, (e) N1s, and (f) Fe2p deconvolution spectra of NCFG-NCL composite.

Fe2p spectra was divided into two pairs of peaks, associated with Fe2p$_{3/2}$ (~710 eV) and Fe2p$_{1/2}$ (~724 eV) due to spin orbit coupling. When Fe^{3+} impurities were present on the surface, Fe2p$_{3/2}$ is located at ~712 eV and Fe2p$_{1/2}$ at ~726 eV.[37, 38] For the NCFG-NCL sample, the Fe2p$_{3/2}$ peak is located at 710.5 eV and Fe2p$_{1/2}$ at 723.5 eV. This result indicates that Fe is present in the form of Fe^{2+} in the LFP phase. In addition, the NCF-NCL and NCL samples exhibit similar Fe peak positions, suggesting that both synthetic processes result in impurity-free LFP (Figure 3.10.).

The electrochemical properties of the NCFG-NCL, NCF-NCL, and NCL samples were investigated. The charge/discharge characteristics of the samples at different rates are shown in Figure 3.11.a–c. All three samples show flat voltage plateaus at approximately 3.0–3.4 V (vs. Li/Li$^+$) caused by the two-phase reaction between LiFePO$_4$ and FePO$_4$. The charge/discharge voltage differences increased with increased rate and the charge/discharge voltage plateau shortened as the rate increased. Even at a high C-rate of 20 C, the discharge plateau of the NCF-NCL and NCFG-NCL samples were maintained above 3.1 V. The NCFG-NCL sample exhibited a longer voltage plateau than those of the NCF-NCL and NCL samples, indicating that the NCFG-NCL sample exhibited the lowest degree of polarization. Furthermore, NCFG-NCL and NCF-

NCL samples showed a lower degree of polarization than NCL samples. It is assumed that the pore space formed by the melamine foam breakage formed an efficient ionic network, and the NCL compactly attached to the NCFG resulting in decreased internal resistance of the electrode (lower degree of polarization). The NCFG-NCL sample showed remarkable discharge capacities of 148, 147, 146, 136, 127, and 108 mAh g^{-1} at 0.1, 0.2, 1, 5, 10, and 20 C, respectively. On the other hand, the NCF-NCL exhibited discharge capacities of 143, 140, 137, 126, 118,
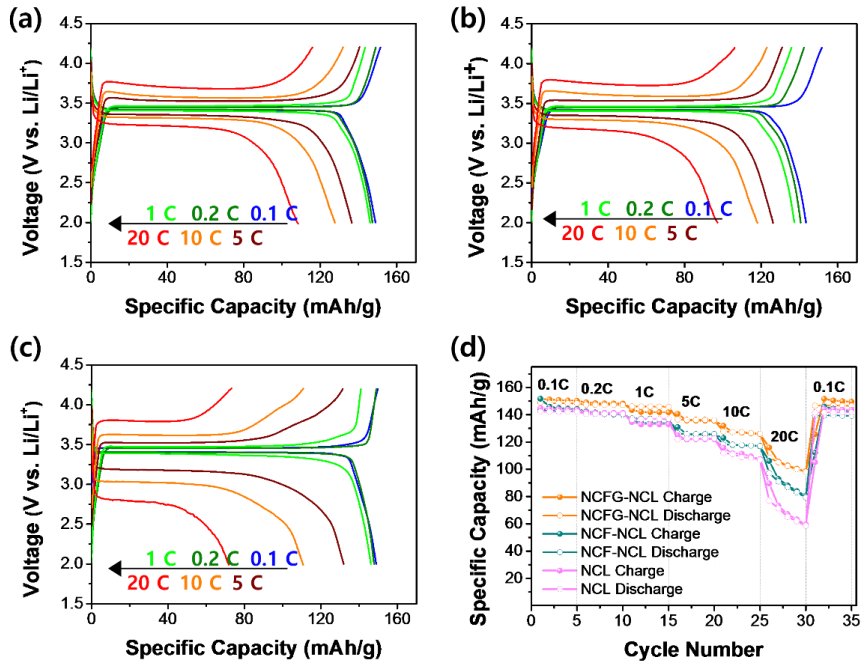
Figure 3.11. Charge/discharge curves of the (a) NCFG-NCL, (b) NCF-NCL, and (c) NCL samples at various rates. (d) Rate capability of the NCFG-NCL, NCF-NCL, and NCL samples.

and 97 mAh g^{-1} at 0.1, 0.2, 1, 5, 10, and 20 C, respectively. Furthermore, NCL showed discharge capacities of 148, 147, 146, 132, 111, and 76 mAh g^{-1} at 0.1, 0.2, 1, 5, 10, and 20 C, respectively. The overall rate performance of the three samples is shown in Figure 3.11.d for a more intuitive rate performance comparison. Comparing the NCF-NCL and NCL samples, the LFP particles were likely connected with a conductive carbon structure, which improved the rate performance because it forms a fast electron transfer path from the active material to current collector. In addition, when comparing NCF-NCL and NCFG-NCL, it is believed that the connectivity of the active materials and conductive carbon structure affected the electrochemical performance. The N-doped carbon structure from the melamine foam was coated with rGO, which improved its electrochemical properties by allowing the LFP to more compactly attach to the carbon structure. In order to examine the effect of graphene and NCF in detail, NCFG-NCL with different NCF and graphene ratio were tested (Figure 3.12.). While maintaining the total carbon amount in composites, the ratio of NCF and graphene was varied as 7:3, 8:2 and

9:1. Interestingly, 7:3 and 9:1 sample showed very similar performance while 8:2 sample (the main sample) showed the best performance. This might be due to the different performance contribution mechanism of NCF and graphene. NCF contributes the wide-range connectivity and graphene may contribute to the connectivity between LFP and NCF. Therefore, if the amount of NCF is larger and the amount of graphene is lower, the wide-range connectivity increases but LFP is not attached well on the framework, which can cause higher internal resistance. On the other hand, if the amount of graphene is larger and the amount of NCF
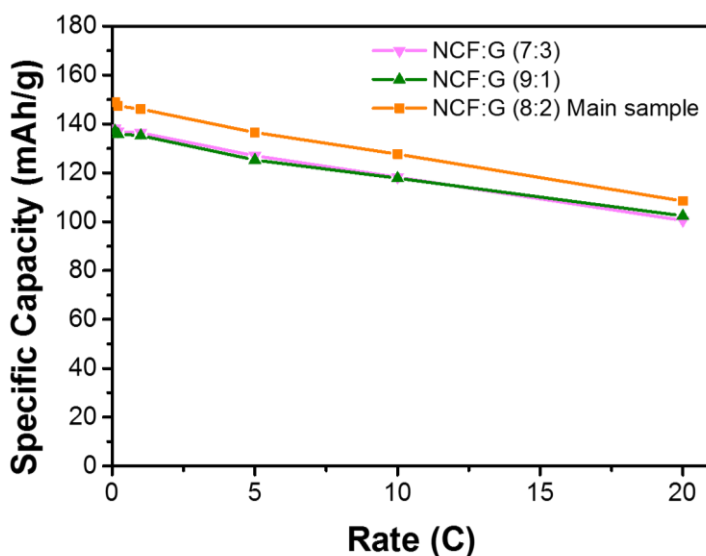
Figure 3.12. Rate performance comparison of NCFG-NCL composite with different ratio of NCF and graphene as 7:3, 9:1, and 8:2.

is lower, there is not enough carbon framework that serves as the wide-range network. As a consequence, 7:3 and 9:1 sample showed the similar performance with different reasons. This result concludes that 8:2 ratio is an optimum balance between the wide-range connectivity and well-attachment of LFP on the framework. In terms of commercialization, achieving good performance at high mass loading is also important. Therefore, the rate performance with different the loading masses was tested (Figure 3.13.). As the loading mass increased, the rate performance of NCFG-NCL electrode deteriorated. This is very natural
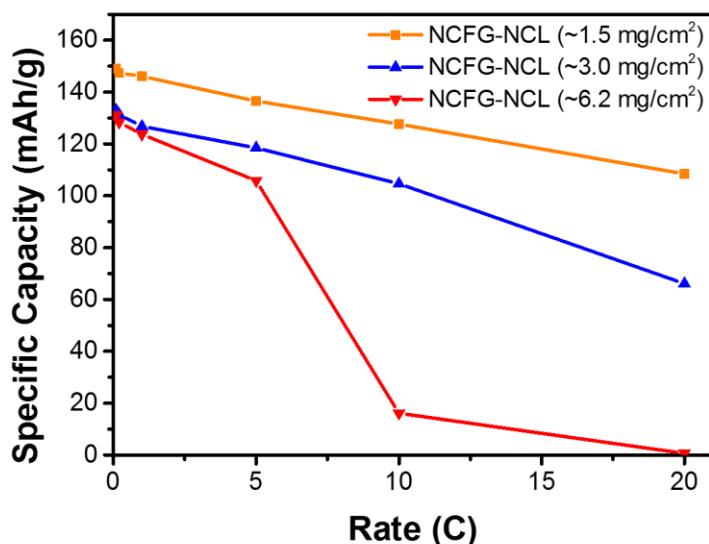
Figure 3.13. Electrochemical performance of NCFG-NCL electrode with different loading mass.

and well-known phenomenon since high mass loading is directly related to a thick electrode that has longer electron and ionic path. Longer diffusion paths cause the electrode polarization which decreases the rate performance.

The dQ/dV curves for the NCFG-NCL, NCF-NCL, and NCL samples during the 0.1 C initial cycle from 2.0 to 4.2 V are shown in Figure 3.12.a. All samples showed a pair of redox peaks corresponding to the two-
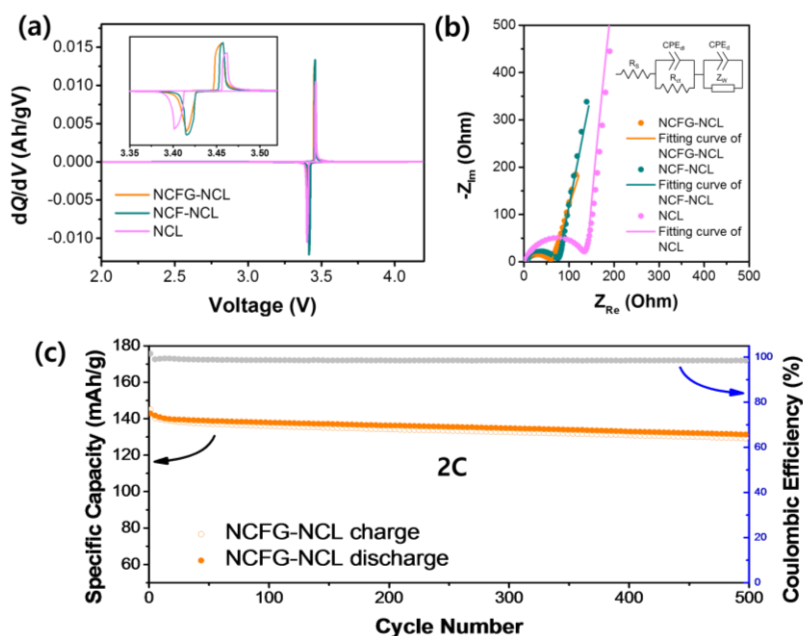
Figure 3.14. (a) dQ/dV profiles of the NCFG-NCL, NCF-NCL, and NCL samples at 0.1 C. (b) Nyquist plots of NCFG-NCL, NCF-NCL, and NCL samples with fitted curves. Inset is the simplified equivalent circuit. (c) Cycling performance of NCFG-NCL, NCF-NCL (black, left), and NCL at 2 C and their coulombic efficiencies (blue, right).

phase reaction of LFP. The potential difference between the redox peaks of the NCFG-NCL, NCF-NCL, and NCL samples was 40, 40, and 60 mV, respectively. These results indicated that the lithium insertion/deinsertion kinetics of NCFG-NCL and NCF-NCL samples is faster than that of the NCL sample due to the shortened Li ion penetration pathways. As shown in Figure 3.14.b, the the EIS spectra consisted of a semicircle and almost linear slope. The suppressed semicircle in between the high to middle frequency range is associated with inter-particle and electrode-electrolyte interface contact resistance. Charge transfer resistances (R_{ct}) of NCFG-NCL, NCF-NCL, and NCL are 58.5 ± 1.54, 69.4 ± 2.1, and 137.0 ± 9.9 Ohm, respectively (Figure 3.14. and Table 3.2.). The NCL particles were uniformly and compactly attached to the carbon structure, which lead to the inter-particle resistance reduction.

Table 3.2. EIS parameters of NCL, NCF-NCL and NCFG-NCL from Figure 3.14.b.

	R_s [Ohm]	R_{ct} [Ohm]
NCFG-NCL	3.4 ± 0.33	58.5 ± 1.54
NCF-NCL	6.1 ± 0.36	69.4 ± 2.1
NCL	3.2 ± 0.74	137.0 ± 9.9

The NCFG-NCL sample exhibited a smaller R_{ct} than the NCF-NCL sample, indicating that rGO induced better electrochemical contact between NCL and NCF. This was likely facilitated by the functional groups on the rGO surface and polydopamine. The NCFG-NCL sample demonstrated excellent cyclability with discharge capacity of 131 mAh g^{-1} at 2 C and capacity retention of 92.2% with average coulombic efficiency of 98.5% after 500 cycles. On the other hand, the NCF-NCL and NCL samples showed reduced capacity retentions of 90.2% and 81.3%, respectively (Figure 3.13.). Interestingly, the NCF-NCL sample exhibited poorer cycling stability despite the better electrochemical properties than the NCL sample. This result implied that NCL particles in the NCF-NCL sample were unstably attached to the NCF. The addition of graphene improved the connectivity between NCF and NCL, resulting in better cycle stability. Also, we compare the rate performances with literatures about LFP/graphene composites (Figure 3.16).
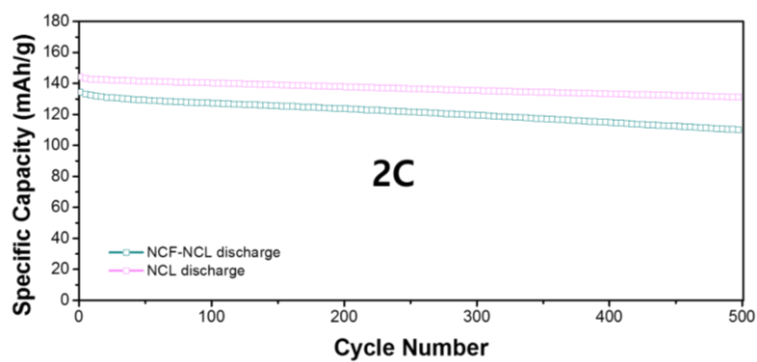
Figure 3.15. Cycling performances of NCL and NCF-NCL at 2 C.
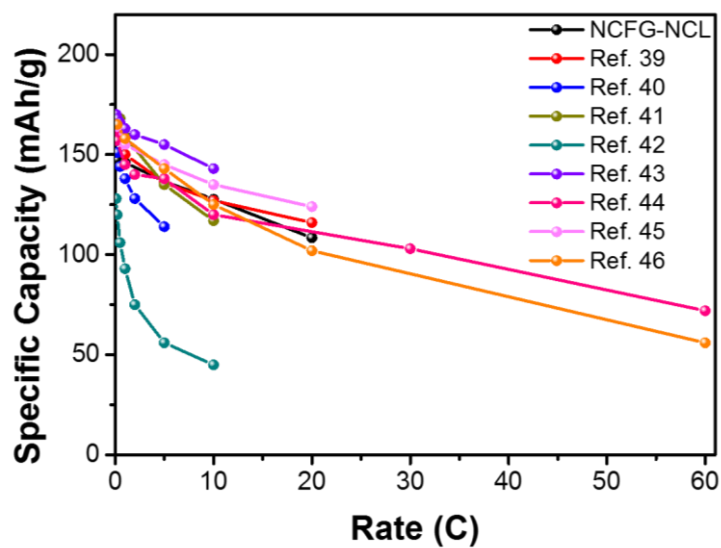
Figure 3.16. Rate performance of the NCFG-NCL compared with previously published studies of LFP and graphene composites.

3.4. Conclusion

In conclusion, by using polydopamine as binding agent and carbon coating source, uniformly carbon-coated LFP particles were attached to rGO wrapped N-doped carbon framework and studied as cathode material for lithium ion battery. The N-doped carbon framework was prepared by heat treatment of GO wrapped melamine foam under reduced atmosphere. The electrochemical performance of the NCFG-NCL electrode (discharge capacity of 108 mAh g^{-1} at 20 C) and stability (discharge capacity of 131 mAh g^{-1} with capacity retention of 92.2% at 2 C after 500 cycles) were superior compared to those of the NCL and NCF-NCL samples. The excellent electrochemical performance was mainly ascribed to the porous and interconnected structure that formed an ionic and electronic network, resulting in good electrochemical properties at high rates. In addition, the rGO enhanced the interaction between the carbon structure (carbonized melamine foam) and LFP, improving the rate property and cycle stability. Finally, the compactly attached NCL in NCFG-NCL shortened the ionic pathway and improved electrochemical performance. Furthermore, it is expected that the NCFG-NCL will be used to the high-power lithium ion batteries.

3.5. References

1.   Choi, J. W.; Aurbach, D., Promise and reality of post-lithium-ion batteries with high energy densities. *Nat. Rev. Mater*. **2016**, *1* (4) 16013-16028.

2.   Goodenough, J. B.; Park, K.-S., The Li-Ion Rechargeable Battery: A Perspective. *J. Am. Chem. Soc*. **2013**, *135* (4), 1167-1176.

3.   Groenewald, J.;   Grandjean, T.; Marco, J., Accelerated energy capacity measurement of lithium-ion cells to support future circular economy strategies for electric vehicles. *Renewable Sustainable Energy Rev*. **2017**, *69*, 98-111.

4.   Padhi, A. K.;   Nanjundaswamy, K. S.; Goodenough, J. B., Phospho-olivines as positive-electrode materials for rechargeable lithium batteries. *J. Electrochem. Soc*. **1997**, *144* (4), 1188-1194.

5.   Yamada, A.;   Chung, S. C.; Hinokuma, K., Optimized $LiFePO_4$ for lithium battery cathodes. *J. Electrochem. Soc*. **2001**, *148* (3), A224-A229.

6.   Swierczynski, M.;   Stroe, D. I.;   Stan, A. I.;   Teodorescu, R.; Kaer, S. K., Lifetime Estimation of the Nanophosphate $LiFePO_4$/C

Battery Chemistry Used in Fully Electric Vehicles. *IEEE Trans. Ind. Appl.* **2015**, *51* (4), 3453-3461.

7.   Wang, J. J.; Sun, X. L., Olivine $LiFePO_4$: the remaining challenges for future energy storage. *Energy Environ. Sci.* **2015**, *8* (4), 1110-1138.

8.   Zhu, P.; Yang, Z.; Zhang, H. Z.; Yu, J.; Zhang, Z.; Cai, J.; Li, C., Utilizing egg lecithin coating to improve the electrochemical performance of regenerated lithium iron phosphate. *J. Alloy Compd.* **2018**, *745*, 164-171.

9.   Wang, X.; Feng, Z.; Huang, J.; Deng, W.; Li, X.; Zhang, H.; Wen, Z., Graphene-decorated carbon-coated $LiFePO_4$ nanospheres as a high-performance cathode material for lithium-ion batteries. *Carbon* **2018**, *127*, 149-157.

10.   Fischer, M. G.; Hua, X.; Wilts, B. D.; Castillo-Martinez, E.; Steiner, U., Polymer-Templated $LiFePO_4$/C Nanonetworks as High-Performance Cathode Materials for Lithium-Ion Batteries. *ACS Appl. Mater. Interfaces* **2018**, *10* (2), 1646-1653.

11.   Naoi, K.; Kisu, K.; Iwama, E.; Nakashima, S.; Sakai, Y.;

Orikasa, Y.; Leone, P.; Dupre, N.; Brousse, T.; Rozier, P.; Naoi, W.; Simon, P., Ultrafast charge-discharge characteristics of a nanosized core-shell structured $LiFePO_4$ material for hybrid supercapacitor applications. *Energy Environ. Sci.* **2016**, *9* (6), 2143-2151.

12.   Gao, L.;   Xu, Z.; Zhang, S., The co-doping effects of Zr and Co on structure and electrochemical properties of $LiFePO_4$ cathode materials. *J. Alloy Compd.* **2018**, *739*, 529-535.

13.   Liu, W.;   Liu, Q.;   Qin, M.;   Xu, L.; Deng, J., Inexpensive and green synthesis of multi-doped $LiFePO_4$/C composites for lithium-ion batteries. *Electrochim. Acta* **2017**, *257*, 82-88.

14.   Yue, H.-F.;   Wang, D.; Li, L.-S., The synergistic effect of multiple doping on structure and electrochemical performance of $LiFe_{1-x-y-z}Zn_xMn_yCa_zPO_4$. *J. Alloy Compd.* **2017**, *711*, 617-626.

15.   Wu, K.;   Du, K.;   Hu, G., Red-blood-cell-like $(NH_4)[Fe_2(OH)(PO_4)_2]\cdot 2H_2O$ particles: fabrication and application in high-performance $LiFePO_4$ cathode materials. *J. Mater. Chem. A* **2018**, *6* (3), 1057-1066.

16.   Yang, W.;   Liu, J.;   Zhang, X.;   Chen, L.;   Zhou, Y.; Zou, Z.,

Ultrathin LiFePO$_4$ nanosheets self-assembled with reduced graphene oxide applied in high rate lithium ion batteries for energy storage. *Appl. Energ.* **2017**, *195*, 1079-1085.

17.   Huang, X.;   Yao, Y.;   Liang, F.; Dai, Y., Concentration-controlled morphology of LiFePO$_4$ crystals with an exposed (100) facet and their enhanced performance for use in lithium-ion batteries. *J. Alloy Compd.* **2018**, *743*, 763-772.

18.   Malik, R.;   Burch, D.;   Bazant, M.; Ceder, G., Particle Size Dependence of the Ionic Diffusivity. *Nano Lett.* **2010**, *10* (10), 4123-4127.

19.   Eftekhari, A., LiFePO$_4$/C nanocomposites for lithium-ion batteries. *J. Power Sources* **2017**, *343*, 395-411.

20.   Li, P.;   Zhang, K.; Park, J. H., Dual or multi carbonaceous coating strategies for next-generation batteries. *J. Mater. Chem. A* **2018**, *6* (5), 1900-1914.

21.   Xu, D.;   Chu, X.;   He, Y.-B.;   Ding, Z.;   Li, B.;   Han, W.; Du, H.; Kang, F., Enhanced performance of interconnected LiFePO$_4$/C microspheres with excellent multiple conductive network and subtle

mesoporous structure. *Electrochim. Acta* **2015**, *152*, 398-407.

22.   Kim, J.-Y.; Kotov, N. A., Charge Transport Dilemma of Solution-Processed Nanomaterials. *Chem. Mater*. **2014**, *26* (1), 134-152.

23.   Wang, Y.; Wang, Y.; Hosono, E.; Wang, K.; Zhou, H., The design of a $LiFePO_4$/carbon nanocomposite with a core-shell structure and its synthesis by an in situ polymerization restriction method. *Angew. Chem. Int. Ed*. **2008**, *47* (39), 7461-7465.

24.   Gaberscek, M.; Dominko, R.; Jamnik, J., Is small particle size more important than carbon coating? An example study on $LiFePO_4$ cathodes. *Electrochem. Commun*. **2007**, *9* (12), 2778-2783.

25.   Zhang, X.; Verhallen, T. W.; Labohm, F.; Wagemaker, M., Direct Observation of Li-Ion Transport in Electrodes under Nonequilibrium Conditions Using Neutron Depth Profiling. *Adv. Energy. Mater*. **2015**, *5* (15), 1500498.

26.   Du, Y.;   Tang, Y.; Chang, C., Enhanced electrochemical performance from 3DG/$LiFePO_4$/G sandwich cathode material. *J. Phys. Chem. Solids* **2017**, *107*, 36-41.

27.   Asfaw, H. D.;   Roberts, M. R.;   Tai, C.-W.;   Younesi, R.;

Valvo, M.; Nyholm, L.; Edstrom, K., Nanosized LiFePO$_4$-decorated emulsion-templated carbon foam for 3D micro batteries: a study of structure and electrochemical performance. *Nanoscale* **2014**, *6* (15), 8804-8813.

28. Lee, J.-S.; Park, G. S.; Kim, S. T.; Liu, M. L.; Cho, J., A Highly Efficient Electrocatalyst for the Oxygen Reduction Reaction: N-Doped Ketjenblack Incorporated into Fe/Fe$_3$C-Functionalized Melamine Foam. *Angew. Chem. Int. Ed.* **2013**, *52* (3), 1026-1030.

29. Lee, J.; Park, S.-K.; Piao, Y., N-doped Carbon Framework/Reduced Graphene Oxide Nanocomposite as a Sulfur Reservoir for Lithium-Sulfur Batteries. *Electrochim. Acta* **2016**, *222*, 1345-1353.

30. Kovtyukhova, N. I.; Ollivier, P. J.; Martin, B. R.; Mallouk, T. E.; Chizhik, S. A.; Buzaneva, E. V.; Gorchinskiy, A. D., Layer-by-layer assembly of ultrathin composite films from micron-sized graphite oxide sheets and polycations. *Chem. Mater.* **1999,** *11*, (3), 771-778.

31. Lee, J.-S.; Park, G. S.; Kim, S. T.; Liu, M. L.; Cho, J., A Highly Efficient Electrocatalyst for the Oxygen Reduction Reaction: N-Doped Ketjenblack Incorporated into Fe/Fe$_3$C-Functionalized Melamine

Foam. *Angew. Chem. Int. Ed.* **2013**, *52*, (3), 1026-1030.

32.   Belharouak, I.;   Johnson, C.; Amine, K., Synthesis and electrochemical analysis of vapor-deposited carbon-coated LiFePO$_4$. *Electrochem. Commun.* **2005,** *7*, (10), 983-988.

33.   Lorestani, F.;   Shahnavaz, Z.;   Mn, P.;   Alias, Y.; Manan, N. S. A., One-step hydrothermal green synthesis of silver nanoparticle-carbon nanotube reduced-graphene oxide composite and its application as hydrogen peroxide sensor. *Sensor Actuat. B-Chem.* **2015,** *208*, 389-398.

34.   Sugino, T.; Tai, T., Dielectric constant of boron nitride films synthesized by plasma-assisted chemical vapor deposition. *Jpn. J. Appl. Phys. 2* **2000,** *39*, (11a), L1101-L1104.

35.   Aijaz, A.;   Fujiwara, N.; Xu, Q., From Metal-Organic Framework to Nitrogen-Decorated Nanoporous Carbons: High CO$_2$ Uptake and Efficient Catalytic Oxygen Reduction. *J. Am. Chem. Soc.* **2014,** *136*, (19), 6790-6793.

36.   Xu, J. T.;   Wang, M.;   Wickramaratne, N. P.;   Jaroniec, M.; Dou, S. X.; Dai, L. M., High-Performance Sodium Ion Batteries Based on a 3D Anode from Nitrogen-Doped Graphene Foams. *Adv. Mater.* **2015,** *27*, (12), 2042-2048.

37.   Dedryvere, R.;   Maccario, M.;   Croguennec, L.;   Le Cras, F.; Delmas, C.; Gonbeau, D., X-Ray Photoelectron Spectroscopy Investigations of Carbon-Coated $LixFePO_4$ Materials. *Chem. Mater.* **2008,** *20*, (22), 7164-7170.

38.   El Ouatani, L.;   Dedryvere, R.;   Siret, C.;   Biensan, P.; Gonbeau, D., Effect of Vinylene Carbonate Additive in Li-Ion Batteries: Comparison of $LiCoO_2$/C, $LiFePO_4$/C, and $LiCoO_2$/$Li_4Ti_5O_{12}$ Systems. *J. Electrochem. Soc.* **2009,** *156*, (6), A468-A477.

39.   Wang, B.; Wang, D. L.; Wang, Q. M.; Liu, T. F.; Guo, C. F.; Zhao, X. S., Improvement of the electrochemical performance of carbon-coated $LiFePO_4$ modified with reduced graphene oxide. *J. Mater. Chem. A* **2013**, *1* (1), 135-144.

40.   Su, C.; Bu, X. D.; Xu, L. H.; Liu, J. L.; Zhang, C., A novel $LiFePO_4$/graphene/carbon composite as a performance-improved cathode material for lithium-ion batteries. *Electrochim. Acta* **2012**, *64*, 190-195.

41.   Guo, X. K.; Fan, Q.; Yu, L.; Liang, J. Y.; Ji, W. X.; Peng, L. M.; Guo, X. F.; Ding, W. P.; Chen, Y. F., Sandwich-like $LiFePO_4$/graphene hybrid nanosheets: in situ catalytic graphitization and their high-rate performance for lithium ion batteries. *J. Mater. Chem. A* **2013**, *1* (38),

11534-11538.

42.   Yang, J. L.; Wang, J. J.; Wang, D. N.; Li, X. F.; Geng, D. S.; Liang, G. X.; Gauthier, M.; Li, R. Y.; Sun, X. L., 3D porous LiFePO$_4$/graphene hybrid cathodes with enhanced performance for Li-ion batteries. *J. Power Sources* **2012**, *208*, 340-344.

43.   Zhang, K.; Lee, J. T.; Li, P.; Kang, B.; Kim, J. H.; Yi, G. R.; Park, J. H., Conformal Coating Strategy Comprising N-doped Carbon and Conventional Graphene for Achieving Ultrahigh Power and Cyclability of LiFePO$_4$. *Nano Lett.* **2015**, *15* (10), 6756-6763.

44.   Ha, S. H.; Lee, Y. J., Core-Shell LiFePO$_4$/Carbon-Coated Reduced Graphene Oxide Hybrids for High-Power Lithium-Ion Battery Cathodes. *Chem-Eur. J.* **2015**, *21* (5), 2132-2138.

45.   Wang, B.; Xu, B. H.; Liu, T. F.; Liu, P.; Guo, C. F.; Wang, S.; Wang, Q. M.; Xiong, Z. G.; Wang, D. L.; Zhao, X. S., Mesoporous carbon-coated LiFePO$_4$ nanocrystals co-modified with graphene and Mg^{2+} doping as superior cathode materials for lithium ion batteries. *Nanoscale* **2014**, *6* (2), 986-995.

46.   Wang, B.; Liu, A. M.; Al Abdulla, W.; Wang, D. L.; Zhao, X. S., Desired crystal oriented LiFePO$_4$ nanoplatelets in situ anchored on a graphene cross-linked conductive network for fast lithium storage.

Nanoscale **2015**, *7* (19), 8819-8828.

Chapter 4. Ultrafine Sn Nanoparticles Anchored on Nitrogen- and Phosphours- Doped Hollow Carbon Frameworks for Lithium Ion Batteries

4.1. Introduction

Lithium-ion batteries have attracted attention because of their great potential in mobile and stationary applications.[1, 2] Graphite, which is extensively utilized as an Lithium-ion batteries anode material, has reltively low theoretical capacity (372 mAh g^{-1}). Therefore, many researchers have focused on alternative anode materials such as Si, Ge, and Sn, which have high capacity. Sn-based materials have been considered as a promising anode material for high-power LIBs because of the abundance, appropriate working voltage, high theoretical capacity (992 mAh g^{-1} for Li$_{4.4}$Sn), and high electrical conductivity of Sn.[3] However, Sn exhibits large volume changes (~300%) during the charge/discharge process, which causes electrode pulverization and consequently quick capacity fading during cycling. Thus, the practical applications of Sn electrode are limited.[4-6]

One of the most widely reported approaches to solve these problems is

reducing the particle size of Sn.[7-11] Decreasing the size of the Sn particles to the nanometer range is considered as an effective way to reduce the mechanical stress caused by volume expansion of Sn particles during the charge/discharge process, thus restraining electrode pulverization.[12-14] In addition, nanosized Sn particles improve the rate capability by shortening the path length of both ions and electrons.[15] However, cycling performance is adversely affected by aggregation and peeling-off failure of the Sn nanoparticles during the charge/discharge process.[5, 16, 17]

One widely used method to prevent these problems is anchoring Sn particles to multifunctional materials. The multifunctional material should have mechanical strength and electrical conductivity, which gives electrochemical stability. Thus, carbon nanotubes, carbon nanofibers, porous carbon, and graphene have been used as multifunctional material.[18-21] Among these, graphene is widely used for anchoring materials because it has good conductivity and flexibility; therefore, it can act as a buffer for volume expansion of Sn-based anodes.[22, 23] Despite anchoring Sn nanoparticles to multifunctional materials, Sn nanoparticles can still re-aggregate and get pulverized over long-term cycling, resulting in deterioration of electrical conductivity, capacity loss, and electrode failure caused by Sn peeling off from the carbon support.

Therefore, to improve the electrochemical performance, it is necessary to formulate a better material composed of Sn nanoparticles with an appropriate carbon structure. Zhang et al. reported that yolk-shell structured Sn@C composite exhibit a reversible capacity of 810 mAh g^{-1} at 200 mA g^{-1} after 500 cycles.[24] Also, Chang et al. reported that N-doped porous carbon and ultra-small Sn particle composites show a reversible capacity of 522 mAh g^{-1} after 1000 cycles.[25] However, it is still difficult to improve the stability of Sn-based electrodes.

Herein, we reported ultrafine Sn nanoparticles anchored on a structurally well-designed carbon framework consisting of graphene and a hollow carbon shell via a simple melt diffusion method. The structurally well-designed carbon structure could imbibe molten Sn and form a composite with well-dispersed ultrafine Sn nanoparticles. The graphene-hollow carbon framework (G-HCF) was prepared by the template method. LFP, well known as a cathode material, was used as a dopant source as well as the template to form the porous and hollow carbon structures. This prepared composite exhibited excellent cycling performance (1048 mAh g^{-1} in 1000 cycles) and rate performance (199 mAh g^{-1} at 5 A g^{-1}). In this case, the G-HCF played three important roles. First, the interconnected hollow carbon structure facilitated more rapid

lithium ion and electron transfer. Also, graphene and the hollow carbon shell were well woven together and induced capillary forces. Therefore, the ultrafine Sn nanoparticles could be formed. Finally, the G-HCF provided buffer space to accommodate the volume expansion of the Sn particles and was doped with N and P to stabilize the electrochemical performance.

4.2. Experimental Section

4.2.1. Chemicals

Lithium hydroxide monohydrate (99%), dopamine hydrochloride, Tris-buffer, and Sn particles were purchased from Sigma-Aldrich Corporation. Iron sulfate heptahydrate (99%) was purchased from Alfa Aesar. Ethylene glycol and hydrochloric acid were supplied by SAMCHUN Pure Chemical. All reagents were used without further purification.

4.2.2. Characterization methods

The crystal structure of the samples was characterized by X-ray diffractometer (XRD; Bruker New D8 Advance, 40 kV, 40 mA, Cu-Kα radiation source, scan range 2θ = 10–80°). The morphology and structure of the samples were characterized via field-emission scanning electron microscopy (FE-SEM; Hitachi S-4800, 15 kV) and high-resolution transmission electron microscopy (HR-TEM; JEOL JEM-2100F, 200 keV) coupled with energy-dispersive X-ray spectrometry. Nitrogen adsorption and desorption isotherms were measured using a BELSORP-mini II apparatus (MicrotracBEL Corp). The Brunauer-Emmett-Teller

(BET) method was used to calculate the average pore diameter and specific surface area. X-ray photoelectron spectroscopy (XPS) analysis was conducted on an Axis-HIS spectrometer with Al irradiation of 12 kV and 18 mA at a constant energy of 20 eV. Raman analysis was performed using a Raman spectrometer (ThermoFisher scientific DXR™ 2xi Raman Imaging Microscope). The thermogravimetric analysis (TGA) was performed using a TGA/DSC 1 analyzer (Mettler Toledo) with a ramp rate of 5 °C/min in air.

4.2.3. Synthesis of Graphene-Hollow Carbon Framework (G-HCF)

Hollow Carbon Framework (HCF)

The as-prepared LFP particles were dispersed in 10 mM Tris-buffer solution by sonication. Then, dopamine hydrochloride (1 mg/mL, 600 mg) was added to the above suspension. The mixture was stirred for 6 h. Then, GO suspension (3 wt% of LFP in H_2O) was added to the above mixture and stirred for an additional 2 h. After the total reaction for 8 h, the composite consisting of LFP, dopamine, and GO suspension was washed three times with deionized water and dried in a freeze dryer. The collected LFP@polydopamine@GO (LFP@PD@GO) composite was calcined at 800 °C for 5 h in an Ar-filled Swagelok container to form

LFP@N-doped carbon@rGO (G-HCF-LFP). To form HCF, the LFP@N-doped carbon samples were prepared under the same conditions without rGO. As-synthesized LFP@N-doped carbon@rGO and LFP@N-doped carbon particles were dispersed in 80 mL of 12 M HCl solution under stirring at 80 °C for 8 h. After the acid treatment, the final products were washed with deionized water and dried in a freeze dryer. Through the above process, LFP@N-doped carbon particles were converted to HCF and LFP@N-doped carbon@rGO particles were converted to G-HCF.

4.2.4. Synthesis of Graphene-Sn (G-Sn) and Hollow Carbon Framework-Sn (HCF-Sn) and Graphene-Hollow Carbon Framework-Sn (G-HCF-Sn)

Powdered tin was anchored on the carbon frameworks by a melt diffusion method. The tin was mixed with G, HCF, and G-HCF in a weight ratio of 1:1 by a mortar for 1 h. The mixtures were heated using a tube furnace at 250 °C for 5 h under inert gas.

4.2.5. Electrochemical characterization

Electrochemical measurements of the samples were conducted using

coin-type CR2016 cells with lithium foil as the counter electrode. The working electrode was composed of the as-prepared active materials, Super P (Timcal, carbon black), and polyvinylidene fluoride with N-methyl-2-pyrrolidone (Sigma-Aldrich) in a weight ratio of 70:20:10. The mixed slurry was spread onto a copper foil current collector and dried before use. The loading density for the active material was ~1.07 mg cm^{-2}. The electrolyte was 1.3 M LiPF$_6$ in ethylene carbonate and diethyl carbonate in a 3:7 v/v mixture of solvent with 10% fluoroethylene carbonate additive. All coin cells were assembled in an Ar-filled glove box. The charge-discharge test was conducted using a WBCS3000s cycler (WonATech, Korea) within a potential range of 0.001–3.0 V (vs. Li/Li$^+$) at room temperature. Electrochemical impedance spectroscopy (EIS) was measured on an SP1 spectrometer (WonATech, Korea) at a frequency range of 100 kHz to 0.1 Hz with an amplitude of 10 mV. Cycling performance was tested after the formation cycle at a current density of 0.1 A g^{-1} for 5 cycles. The electrochemical performance was tested using total active material weight of all three samples.

4.3. Results and Discussion

Figure 4.1. illustrates the synthesis of the Graphene-hollow carbon framework-Sn (G-HCF-Sn) composite. Dopamine was used as the nitrogen doping source for the carbon structure and as a binding agent between LFP and GO because dopamine contains both catechol and amine functional groups.[26] LFP@PD@GO was obtained by simple polymerization, and it was subjected to heat treatment at 800 °C. During this heat treatment, GO was reduced to
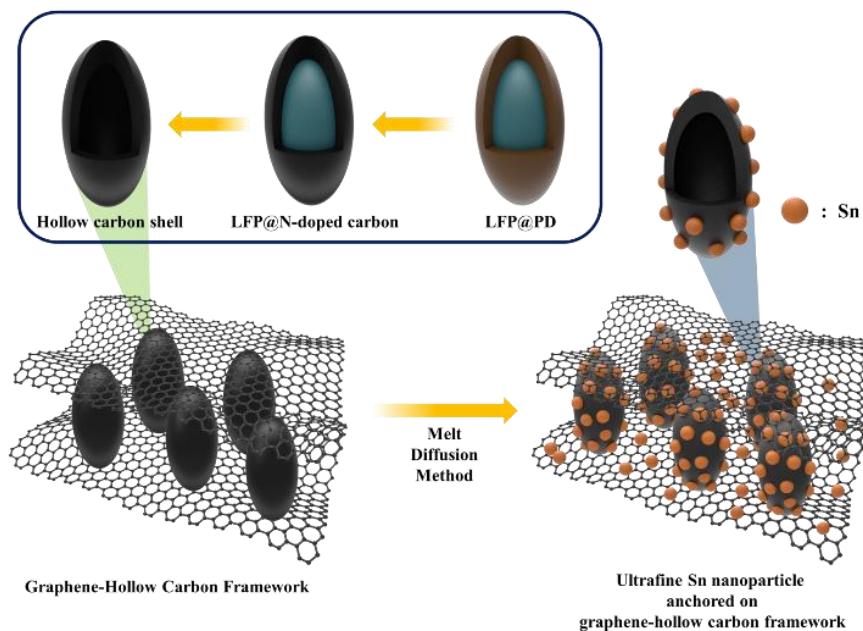
Figure 4.1. Schematic illustration of the synthesis of G-HCF-Sn composite.

rGO and polydopamine became N-doped carbon. Furthermore, LFP coated by N-doped carbon diffused out from the carbon shell, leaving a porous carbon structure at 800 °C (Figure 4.2.). On the other hand, LFP particles did not diffuse out from the carbon shell at 700 °C heat treatment (Figure 4.3.c and d). After 800 °C heat treatment, LFP was dissolved and washed away from the carbon framework by acid treatment to obtain G-HCF. At 250 °C, molten Sn could be imbibed to the carbon structure due to the low melting point of Sn (231 °C).[27] The capillary force exerted by the carbon scaffold sandwiched with hollow porous carbon structures could help the molten Sn to get embedded into the carbon structure.
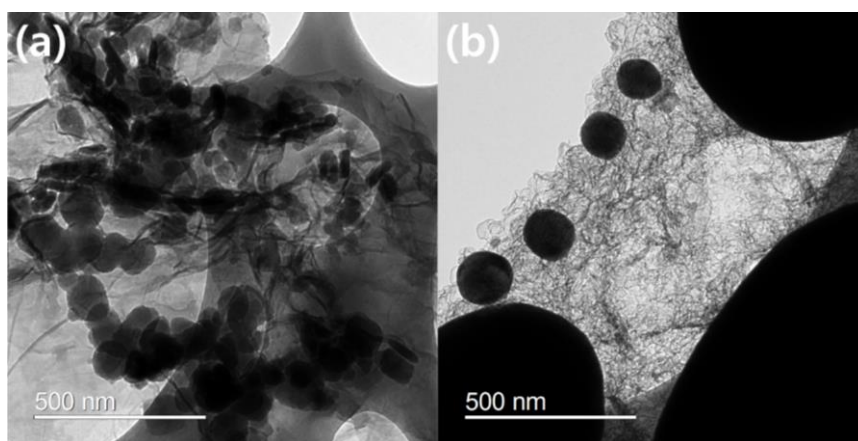
Figure 4.2. TEM images of G-HCF-LFP samples (a) before and (b) after heat treatment.

Graphene-Sn (G-Sn) and hollow carbon framework-Sn (HCF-Sn) samples were also prepared to compare the effect of the carbon structure.

First, as shown in Figure 4.4.a, the crystal structures of G-HCF-LFP and HCF-LFP were characterized by XRD. All diffraction peaks corresponded to the orthorhombic space group Pnma (JCPDS Card No. 81-1173). These samples were converted to HCF-Sn and G-HCF-Sn throughout the process shown in Figure 4.1. The crystallographic structures of G-Sn, HCF-Sn, and G-HCF-Sn are
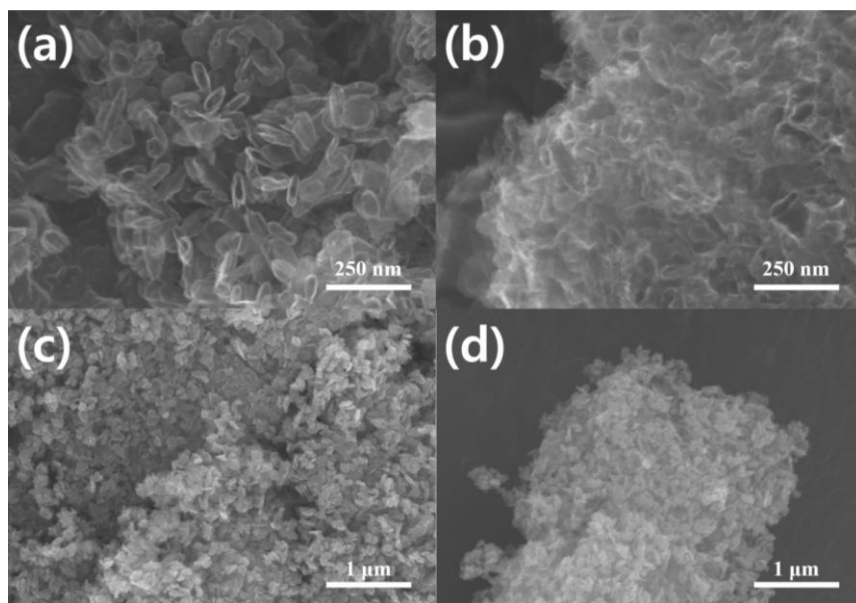
Figure 4.3. SEM images of (a) HCF, (b) G-HCF, (c) HCF-LFP (after 700 °C heat treatment), and (d) G-HCF-LFP (after 700 °C heat treatment).

shown in Figure 4.5.a. All diffraction peaks were well indexed to tetragonal Sn with a space group of $I4_1/amd$ (JCPDS Card No. 065-0296) and tetragonal SnO with a space group of P4/nmm (JCPDS Card No. 06-0395), which indicated the coexistence of the Sn and SnO phases in the composite. The SnO phase was considered to be formed by residual oxygen functional groups on the carbon surface. Furthermore, a broad peak at $2\theta = 26°$ was observed as the (002) peak for the carbonaceous materials.[28] There was no other diffraction peak for LFP, indicating that LFP was removed during acid treatment. The amount of Sn in the all three composites was calculated because the weight increases by the oxidation process when the heat treatment is performed in the oxygen atmosphere.
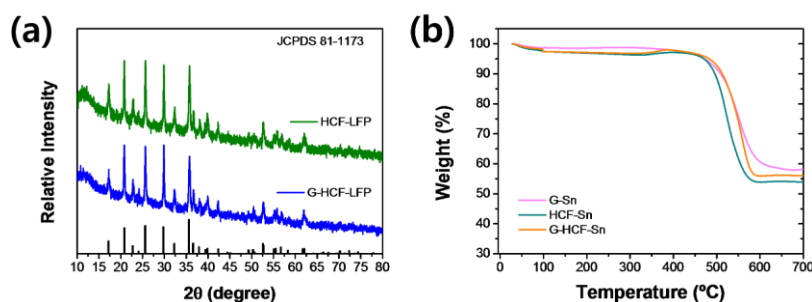
Figure 4.4. (a) XRD patterns of HCF-LFP and G-HCF-LFP, and (b) TGA analysis of G-Sn, HCF-Sn, and G-HCF-Sn with temperature range from 25 to 700 °C under air flow.

FE-SEM measurements were conducted to investigate the morphology and microstructure of the samples. The hollow carbon framework (HCF), G-HCF, hollow carbon framework-LFP (HCF-LFP), and graphene-hollow carbon framework-LFP (G-HCF-LFP) samples are shown in the Figure 4.3. As shown in the Figure 4.3.c and d, the LFP nanoparticles were well covered by the carbon structure. On the other hand, HCF and G-HCF were translucent carbon structures, indicating that LFP particles were removed and the hollow carbon structure retained the shape of the LFP nanoparticles after acid treatment. Figure 4.6. shows the FE-SEM images of the as-prepared G-Sn, HCF-Sn, and G-HCF-Sn samples. For G-Sn and HCF-Sn (Figure 4.6.a and b and Figure 4.6.c and d, respectively), several hundred nanosized Sn nanoparticles were
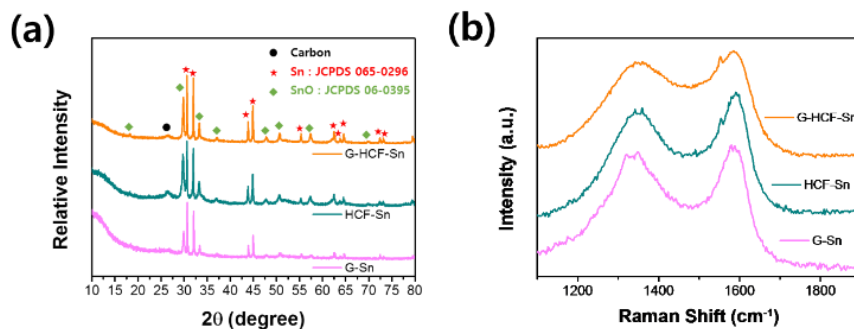
Figure 4.5. (a) XRD patterns and (b) Raman spectra of G-Sn, HCF-Sn, and G-HCF-Sn samples.

observed in the samples, which means that Sn aggregated rather than dispersed on the carbon. On the other hand, G-HCF-Sn (Figure 4.6.e and f) did not show several hundred nanosized Sn particles. Furthermore, most of the translucent carbon structures disappeared, unlike for HCF-Sn.
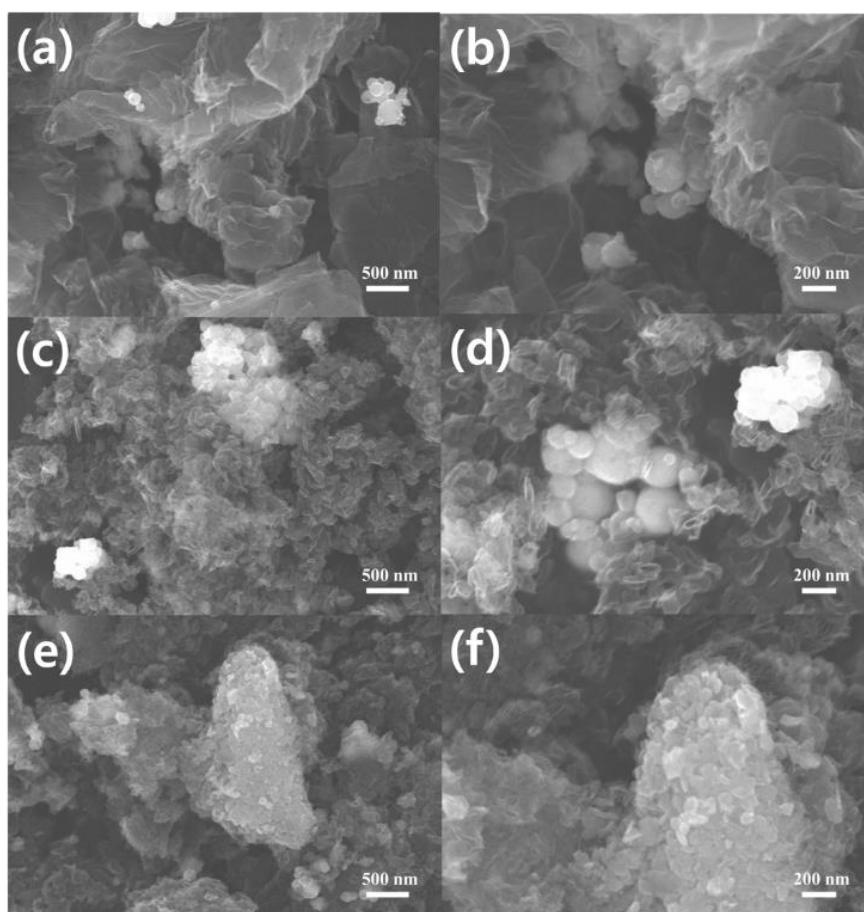
Figure 4.6. SEM images of (a and b) G-Sn, (c and d) HCF-Sn, and (e and f) G-HCF-Sn samples.

HR-TEM measurements were utilized to confirm the microstructure of the as-prepared samples. From Figure 4.7., we found that the LFP particles are removed during the acid treatment. G-Sn showed aggregated several hundred nanosized Sn particles (Figure 4.8.a and b). From the enlarged image in Figure 4.8.b and EDS mapping in Figure 4.8.c, some molten Sn formed the ultrafine Sn nanodots attached to the graphene surface.   In the case of the
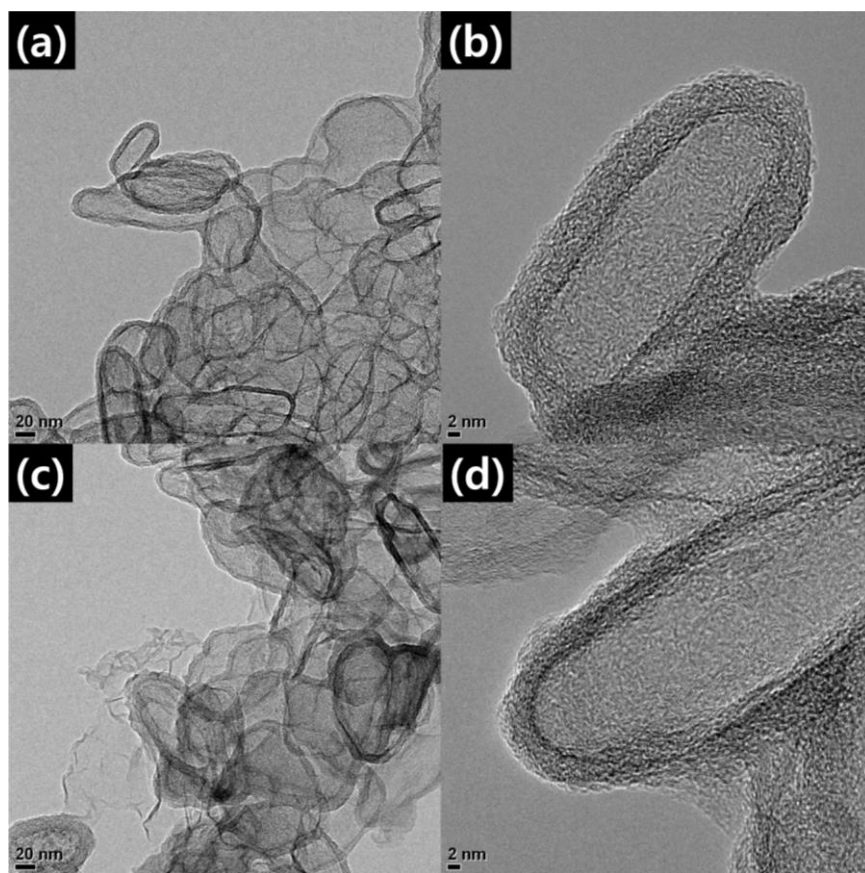
Figure 4.7. TEM images of (a, b) HCF and (c, d) G-HCF samples.

HCF-Sn sample (Figure 4.8.d–f), it seemed that the Sn particles were distributed between the hollow carbon shells. Considering the SEM and TEM results, most of the molten Sn preferred to agglomerate together to form large particles, but some molten Sn penetrated the void space between the hollow carbon shells due to capillary force. However, as shown in Figure 4.8.g–i, Sn particles
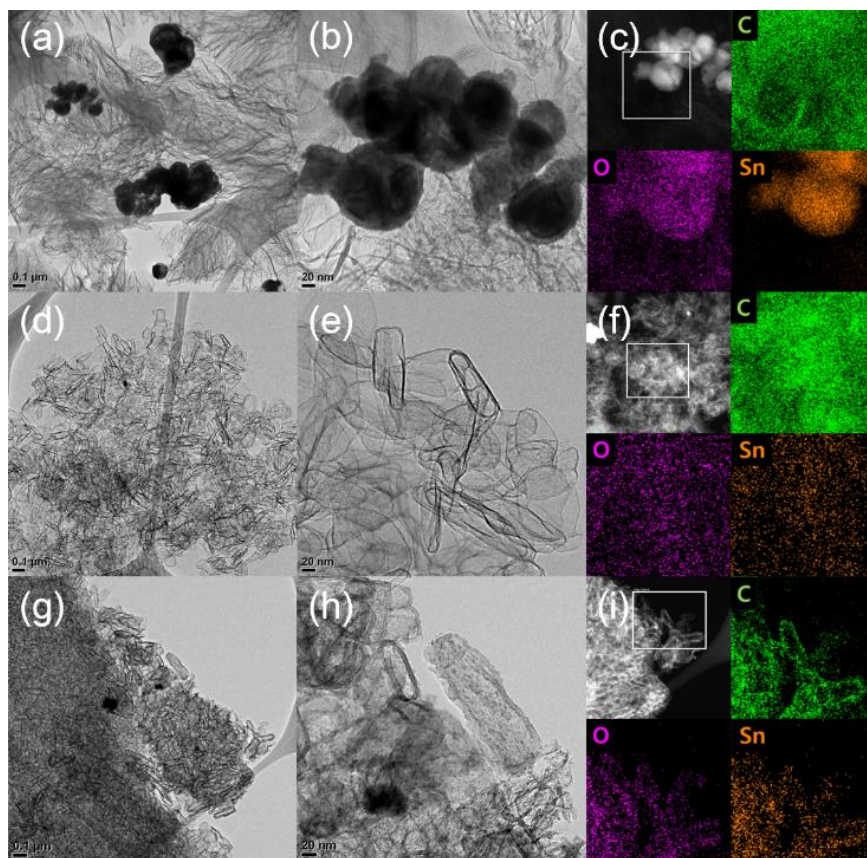
Figure 4.8. TEM images with C, O, and Sn element mapping of (a - c) G-Sn, (d - f) HCF-Sn, and (g - i) G-HCF-Sn samples, respectively.

were distributed over the entire carbon structure. Some of the Sn particles aggregated to sizes of several tens of nanometers, but most of the Sn particles were found to be ultrafine Sn nanodots attached to the carbon structure. Furthermore, as shown in Figure 4.9., crystalline Sn particles of a very small size were observed. EDS mapping was used to confirm that nitrogen- and phosphorus-doped carbon was obtained (HCF, G-HCF, HCF-Sn, and G-HCF-Sn) (Figure 4.10.). It was confirmed that the carbon structure was well doped with nitrogen and phosphorus and a small amount of Fe was partially retained. It was believed that the hollow carbon shell sandwiched between graphene layers could induce capillary force on molten Sn, so that the Sn particles were uniformly anchored on
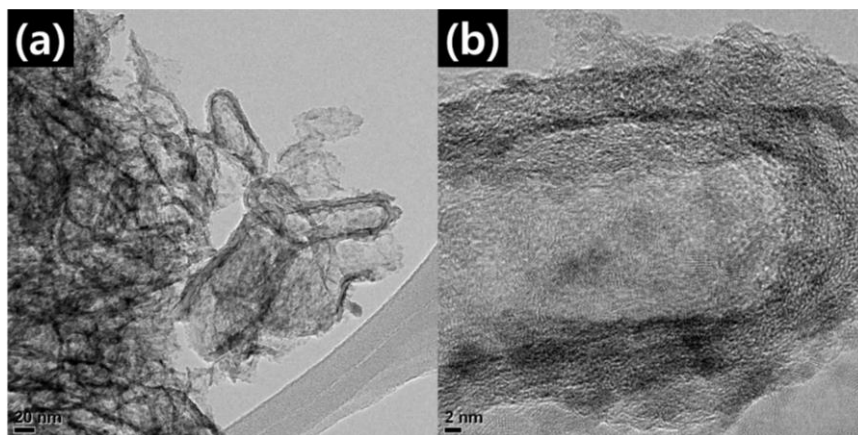
Figure 4.9. (a) Low and (b) high-resolution TEM images of G-HCF-Sn.

the carbon structure by forming ultrafine Sn nanodots. In addition, doping elements could bridge Sn nanoparticles to the carbon support, which leads Sn nanoparticles to be distributed well on the carbon framework. This will be discussed later in detail.

BET analysis was performed to confirm the effect of the existence of the Sn nanoparticles on the samples (Table 4.1.). For the G-Sn sample, rGO was used for comparison. The specific surface area of rGO, HCF, and G-HCF was 448.9 m^2 g^{-1}, 402.9 m^2 g^{-1}, and 469.3 m^2 g^{-1}, respectively. In particular, the G-HCF sample had a higher
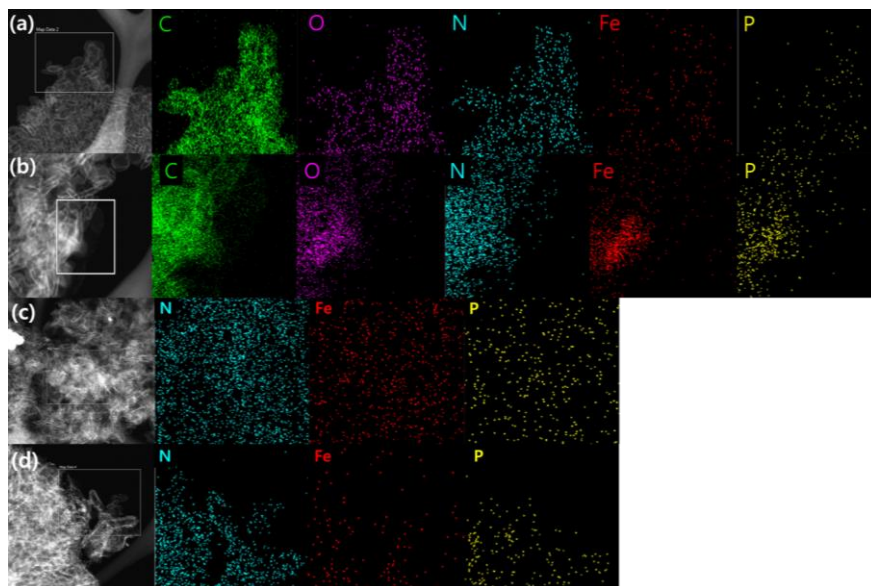
Figure 4.10. EDS mapping images of (a) HCF, (b) G-HCF, (c) HCF-Sn, and (d) G-HCF-Sn composites.

specific surface area than the rGO sample, suggesting that the hollow carbon shell was appropriately placed between the graphene layers and served as a spacer. After the Sn melt diffusion process, the specific surface area of the G-Sn sample remarkably decreased
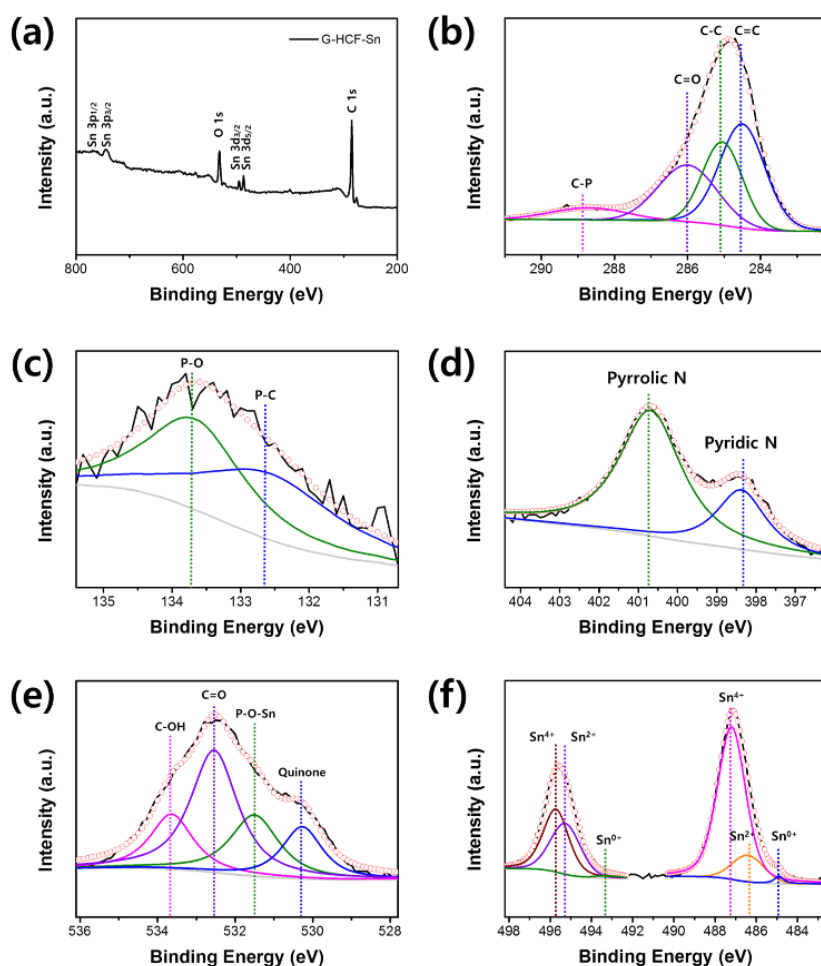
Figure 4.11. XPS spectra of the G-HCF-Sn composite: (a) wide scan, (b) C1s, (c) P2p, (d) N1s, (e) O1s, and (f) Sn3d.

to 134.4 m^2 g^{-1} because Sn particles filled most of the void spaces between the rGO layers. Also, the HCF and HCF-Sn samples showed no significant difference in specific surface area. This indicated that Sn did not penetrate the hollow carbon structure and the Sn particles aggregated of the HCF surface. For G-HCF and G-HCF-Sn, the surface area decreased because Sn particles filled the void space between the carbon structures. However, G-HCF-Sn sample had a larger specific surface area than the G-Sn sample. This result implied that for the G-HCF-Sn sample, the ultrafine Sn

Table 4.1. BET surface area and total pore volume of HCF, HCF-Sn, G-HCF, and G-HCF-Sn samples.

Sample	S_{BET} (m^2 g^{-1})	Pore volume (cm^3 g^{-1})	Mean pore diameter (nm)
rGO	448.9	3.1	28.4
G-Sn	134.3	0.8	25.5
HCF	402.9	92.5	25.6
HCF-Sn	408.7	93.9	37.2
G-HCF	469.3	107.8	25.6
G-HCF-Sn	262.6	60.3	25.0

particles were anchored on the carbon surface, resulting in a smaller decrease in surface area than in the G-Sn sample.

 To investigate how doping elements interact with carbon and Sn in the composites, G-HCF-Sn composite was identified by XPS. As expected, C, N, P, O, and Sn were confirmed in the composite (Figure 4.11.a).   As shown in Figure 4.11.b, the C1s spectrum could be deconvoluted into four different peaks at 284.5 eV, 285.1 eV, 286 eV, and 288.7 eV, assigned to the C=C, C-C, C=O, and C-
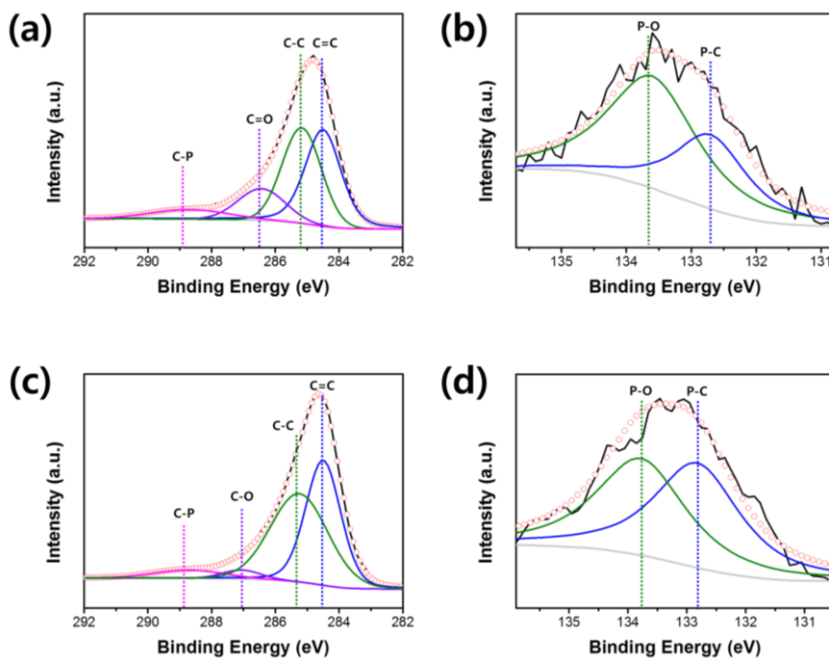
Figure 4.12. (a) C1s and (b) P2p deconvolution spectra of HCF composite and (c) C 1s and (d) P2p deconvolution spectra of G-HCF composite.

P bonds, respectively.[29] To further confirm the C-P bond, high-resolution P2p spectra were investigated (Figure 4.11.c). Two peaks centered at 132.5 eV and 133.6 eV, corresponding to the P-C and P-O bonds,[29] respectively, were observed. The composition of the HCF and G-HCF samples were also obtained (Figure 4.12.) to identify the phosphorus source. For these samples, the C-P and P-O bonds were observed in the C1s and P2p deconvoluted results. However, for the G-Sn sample (shown in Figure 4.13.a), no P element was observed. This indicated that the P-O bond is due to the phosphate residue of the LFP template and that the P-C bond might be formed during carbonization of polydopamine. Figure 5d shows the high-resolution XPS N1s spectra; two peaks centered at 398.3 eV and 400.6 eV, assigned to pyridic N and pyrrolic N
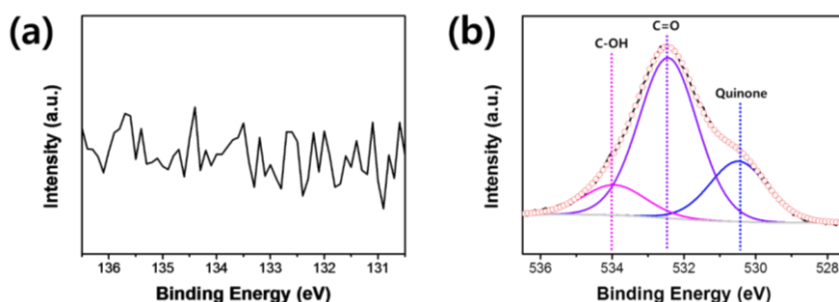
Figure 4.13. (a) P2p deconvolution spectra of G-Sn composite and (b) O1s deconvolution spectra of G-HCF composite.

from the amine group of polydopamine,[30] respectively, were observed. Furthermore, the high-resolution O1s spectra were also deconvoluted (Figure 4.11.e). The O1s peaks at 533.6 eV and 532.5 eV were associated with graphene functional groups. The peak at 531.5 eV was attributed to the P-O-Sn bond.[31] There was no P-O-Sn bond in the G-HCF sample (Figure 4.13.b), indicating that Sn formed the P-O-Sn bond during the melt diffusion process and was attached to the carbon surface by the phosphorus functional group. The peak at 530.2 eV was ascribed to quinone from the catechol groups of dopamine.[32] In the high-resolution Sn3d spectra, peaks were observed around 495.5 eV and 487 eV, assinged to Sn $3d_{5/2}$ and Sn $3d_{3/2}$, respectively (Figure 4.11.f). The Sn $3d_{5/2}$ orbital could be deconvoluted into three different peaks at 495.7 eV, 495.5 eV, and 493.2 eV. In addition, the Sn $3d_{5/2}$ orbital could be deconvoluted into three different peaks at 487.2 eV, 486.4 eV, and 484.9 eV. The peaks at 495.7 eV and 487.2 eV were ascribed to Sn^{4+} in SnO_2. Furthermore, the peaks at 495.2 eV and 486.4 eV were attributed to Sn^{2+} in SnO. The weakest peaks at 493.2 eV and 484.9 eV were assigned to Sn^{0+}.[33] This result indicated that the ultrafine Sn nanoparticles in the G-HCF-Sn composite were

covered with oxide layers. The oxide layers were derived from the graphene functional groups and residual phosphate groups. These functional groups bridged Sn and G-HCF by forming SnO and P-O-Sn bonds. Therefore, doping elements help Sn nanoparticles to bind well on the carbon framework. Furthermore, the surface of the SnO particles could be partially oxidized and converted to SnO_2 in ambient air because the SnO particles were unstable.[34] Therefore, Sn^{4+} peaks were observed.

Figure 4.14. shows the electrochemical performance of the G-Sn, HCF-Sn, and G-HCF-Sn electrodes. The rate capability of the G-HCF-Sn electrode was evaluated (Figure 4.14.a). The assembled half-cell was tested in a current density range of 0.1–5 A g^{-1} within a voltage window of 0.001–3.0 V. The average discharge capacities were 1118, 746.6, 596.6, 471.4, 351.2, and 199.4 mAh g^{-1} at current densities of 0.1, 0.2, 0.5, 1, 2, and 5 A g^{-1}, respectively. In contrast, the G-Sn electrode showed much lower capacities of 1015.8, 561, 334.6, 236, 173, and 61.6 mAh g^{-1} at current densities of 0.1, 0.2, 0.5, 1, 2, and 5 A g^{-1}, respectively. Furthermore, the HCF-Sn electrode showed capacities of 870, 532.2, 383.4, 284.2, 202.4, and

86.6 mAh g^{-1} at current densities of 0.1, 0.2, 0.5, 1, 2, and 5 A g^{-1}, respectively.
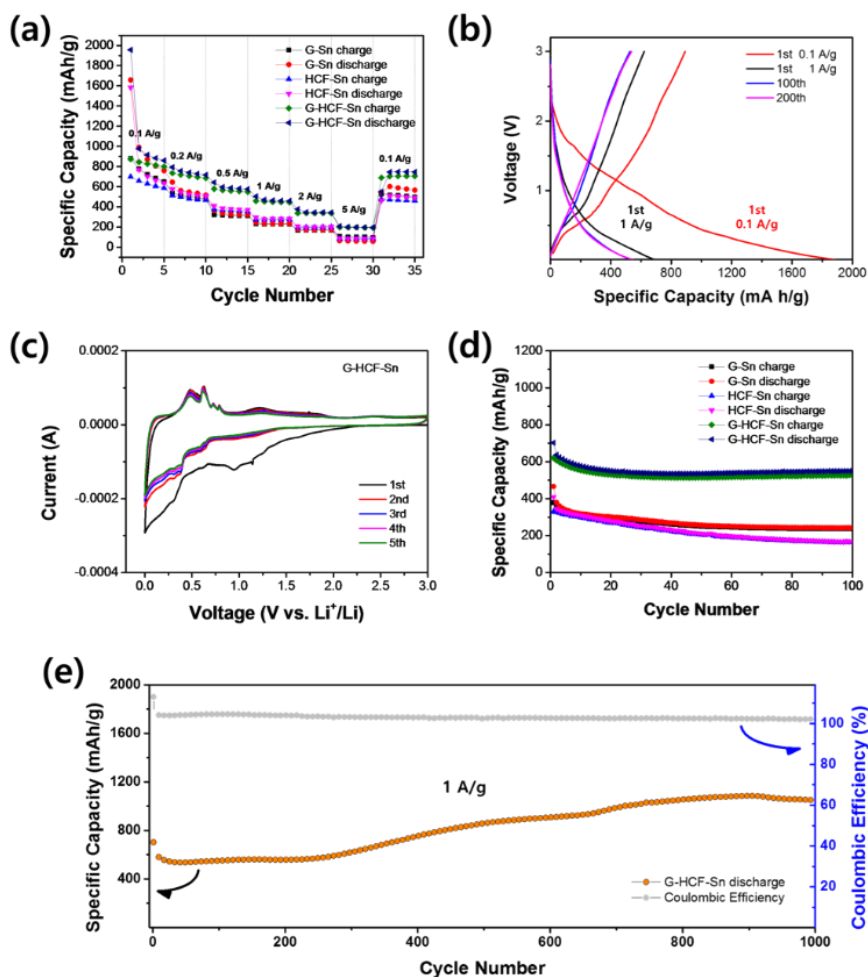
Figure 4.14. (a) Rate performance of G-Sn, HCF-Sn, and G-HCF-Sn samples ranging from 0.1 A g^{-1} to 5 A g^{-1}. (b) Galvanostatic charge/discharge profiles of G-HCF-Sn composite at a current density of 1.0 A g^{-1}. (c) CV curves of G-HCF-Sn composite in the voltage range of 0.001–3.0 V at a scan rate of 100 mV/s. (d) Cycling performance of G-Sn, HCF-Sn, and G-HCF-Sn electrodes at 1 A g^{-1} for 200 cycles. (e) Long-term cycling test of G-Sn, HCF-Sn, and G-HCF-Sn samples at 1 A g^{-1} for 1000 cycles.

The enhanced rate performance of the G-HCF-Sn electrode could be attributed to the rapid diffusion of lithium ions due to the well-woven structure of graphene and the hollow carbon shell as well as to the fast electron transport due to good contact between the carbon structure and the ultrafine Sn nanoparticles. Figure 4.15. compares the rate performance between G-HCF-Sn and other previously published Sn composite anode.[11, 20, 33, 35-38] Galvanostatic charge/discharge profiles of G-HCF-Sn were obtained at a current density of 0.1 A g^{-1} for the first five cycles and 1 A g^{-1} for the 1000th
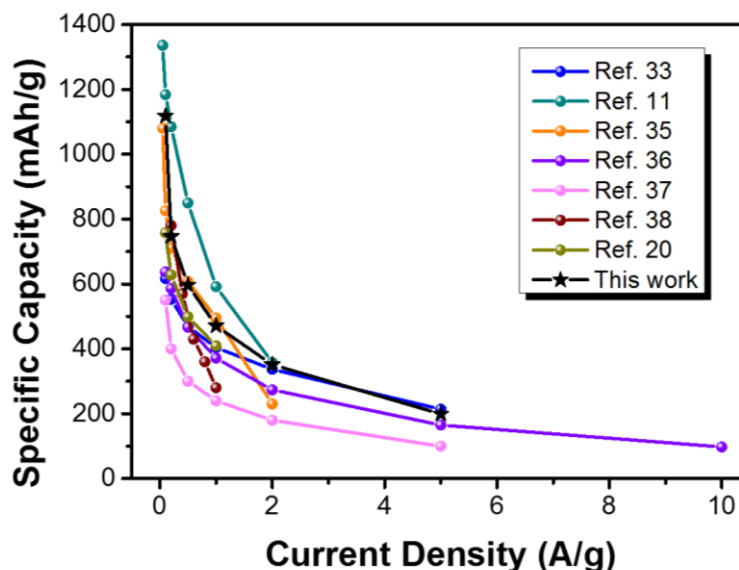
Figure 4.15. Comparison of the rate capability of this work with previously published Sn based composite electrodes.

cycle in the potential range between 0.001 and 3.0 V. The typical galvanostatic charge/discharge curves of the 1st, 100th, and 200th cycles are shown in Figure 4.14.b. The unclear plateau of the galvanostatic curve might imply the successful formation of ultrafine tin and carbonaceous material composite.[39, 40] The first lithiation and delithiation capacities at 0.1 A g^{-1} were 1909 mAh g^{-1} and 892 mAh g^{-1}, respectively, corresponding to a coulombic efficiency of 46.7%. The initial irreversible capacity decay of the G-HCF-Sn composite might arise from the solid-electrolyte interphase (SEI) layer formed by SnO_x and the irreversible lithium storage in carbon. After 200 cycles, the galvanostatic charge/discharge profiles well overlapped and showed a reversible capacity of 558 mAh g^{-1}.

Typical cyclic voltammetry (CV) curves of the G-HCF-Sn composite at a scan rate of 0.1 mV s^{-1} between 0.001 and 3.0 V are shown in Figure 4.14.c. In the first cathodic scan, the irreversible peak around 1.1 V was attributed to the formation of the SEI layer and SnO$_x$ reduction from the Sn surface. The peak around 0.9 V was associated with conversion of SnO$_2$ to Sn and the formation of Li$_2$O. The other two cathodic peaks below 0.7 V were associated with the lithiation of Sn (Li-Sn alloy Li$_x$Sn). On the other hand, an irreversible peak around 1.2 V was observed, corresponding to the conversion of LiC$_x$ to C. The anodic peak between 0.4 and 0.8 V could be associated with the de-alloying of Li$_x$Sn.[41, 42] The peaks related to the SnO$_2$ and SEI formation were observed only for the first cycle. In addition, the CV peaks well overlapped after the first cycle, indicating that the alloying and de-alloying process of the
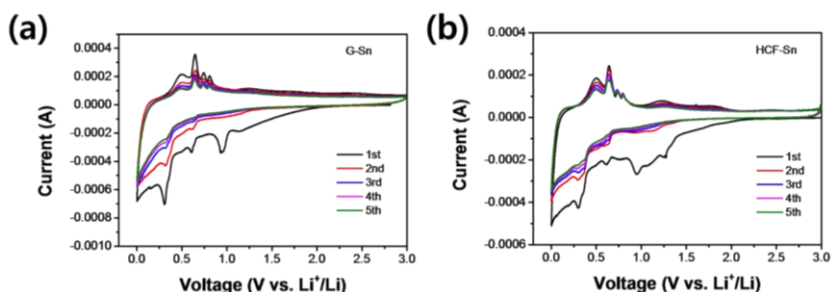
Figure 4.16. CV curves of (a) G-Sn and (b) HCF-Sn composites in voltage range of 0.001-3.0 V (V vs. Li$^+$/Li) at a scan rate of 0.1 V s^{-1}.

ultrafine Sn nanoparticles was reversible. The CV curves of the G-Sn and HCF-Sn samples were also obtained (Figure 4.16.).

Figure 4.14.d shows the cycling performance of the G-Sn, HCF-Sn, and G-HCF-Sn samples at a current density of 1 A g^{-1}. The G-Sn, HCF-Sn, and G-HCF-Sn samples showed a reversible capacity of 242, 168, and 550 mAh g^{-1}, respectively. The G-HCF-Sn sample showed better cycling performance than the other samples. Figure 4.14.e shows the long-term cycling performance of the G-HCF-Sn sample at a current density of 1.0 A g^{-1} for 1000 cycles. The capacity of the G-HCF-Sn composite decreased for the initial cycles and increased gradually after 50 cycles. This phenomenon is often observed for nanoscale metal oxides and can be ascribed to the reversible formation of a polymeric gel-like layer.[24, 43-45] The formation and decomposition of this layer are attributed to the capacity. In addition, the ultrafine Sn nanoparticles, well-dispersed in the G-HCF-Sn composite, led to an increased surface area and lithium ions could be trapped by the formed polymeric gel-like layer. The G-HCF-Sn composite showed excellent cycling performance (specific capacity of 1048 mAh g^{-1} at a current density 1.0 A g^{-1} for 1000 cycles). This indicated that the ultrafine Sn

particles were well anchored on the carbon surface, which prevents Sn nanoparticles from losing contact with the carbon support during the charge/discharge process. Especially, doping elements could help Sn nanoparticles to bind with the carbon support. In addition, the hollow carbon structure provided buffer space and structural stability.

EIS was performed for the G-Sn, HCF-Sn, and G-HCF-Sn samples. Figure 4.17 shows the Nyquist plot of the as-prepared samples. These samples showed compressed semicircles in the high-frequency range and straight lines in the low-frequency range. The compressed semicircles corresponded to resistance at the electrode/electrolyte interface and that between the particles. The semicircle diameters of the G-Sn and G-HCF-Sn electrodes were
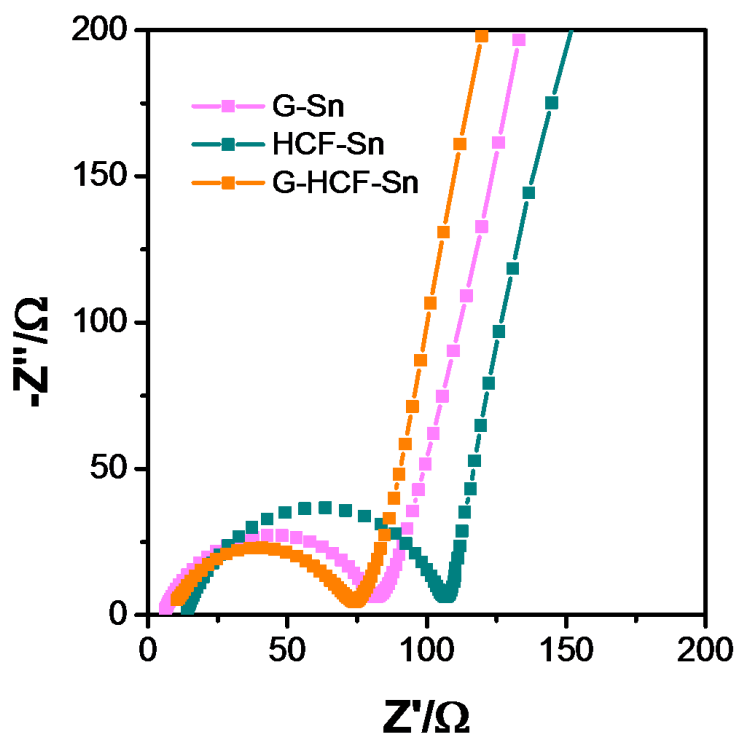
Figure 4.17. Nyquist plots of G-Sn, HCF-Sn, and G-HCF-Sn composite in frequency range from 100 kHz to 0.1 Hz.

smaller than that of the HCF-Sn electrode. Further, the G-HCF-Sn electrode had a smaller semicircle diameter than the G-Sn electrode. This result implied that the graphene-based carbon structures reduced the inter-particle resistance between Sn and carbon. From the XPS and EIS results, it was found that the ultrafine Sn nanoparticles were well anchored on the carbon structure by the doping element, thus reducing the inter-particle resistance. Furthermore, the microstructures of the G-Sn, HCF-Sn, and G-HCF-Sn electrodes after 100 cycles at 1 A g^{-1} were investigated by SEM (Figure 4.18.). Unlike the G-Sn and HCF-Sn electrodes, the G-HCF-Sn electrode was confirmed to be well covered by the carbon structure even after the charge/discharge process. To investigate the structural stability of the all three samples, TEM analysis was conducted with the 200-cycled electrodes at 2 A g^{-1}
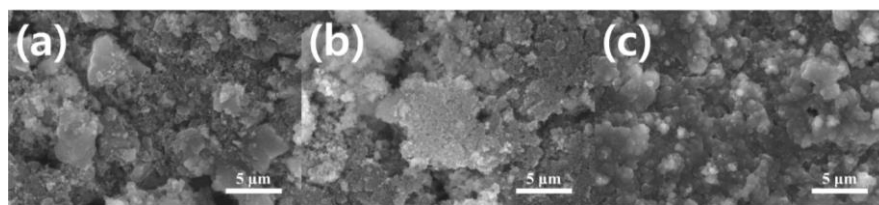
Figure 4.18. SEM images of (a) G-Sn, (b) HCF-Sn, and (c) G-HCF-Sn electrodes after 100 cycles at 1 A g^{-1}.

(Figure 4.19.). In the case of G-Sn and HCF-Sn samples (Figure 4.19. a and b, respectively), the Sn particles were aggregated and failed to maintain the initial morphology after the cycle. However, the Sn particles did not fall off completely from the carbon structure. This might be because the doping elements in the carbon structure hold the Sn particles well. On the other hand, the ultrasmall Sn nanoparticles in the G-HCF-Sn sample (Figure 4.19.c) were only slightly aggregated after the cycle and they were not aggregated to the larger Sn particles like the other samples. This result implied that the hollow carbon structure could accommodate Sn volume changes during the charge/discharge process and the ultrafine Sn nanoparticles were prevented from falling off the carbon structure.
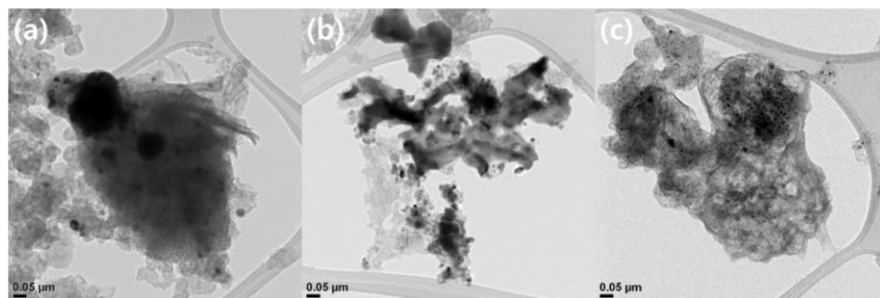
Figure 4.19. TEM images of (a) G-Sn, (b) HCF-Sn, and (c) G-HCF-Sn samples after 200 cycle at 2 A g^{-1}.

4.4. Conclusion

A G-HCF-Sn composite was fabricated using a simple melt diffusion method. The G-HCF carbon structure was prepared by the template method using LFP particles. The G-HCF carbon structure consisted of a uniformly dispersed hollow carbon shell between graphene layers. Molten Sn could be uniformly imbibed into the G-HCF structure by capillary force to form ultrafine Sn nanoparticles. Thus, the ultrafine Sn nanodots were integrated into the G-HCF structure. In the process of preparing the G-HCF carbon structure, nitrogen from polydopamine and phosphorus from LFP were doped on the structure during heat treatment. These doping elements acted as bridges between the G-HCF carbon structure and the ultrafine Sn nanoparticles. The ultrafine Sn nanoparticles anchored on the hollow carbon structure provided sufficient void space to accommodate volume changes occurring in the Sn particles during the charge/discharge process. The G-HCF-Sn anode had a high reversible capacity of 1048 mAh g^{-1} at 1.0 A g^{-1} after 1000 cycles. Furthermore, it exhibited good rate performance and stability up to 5.0 A g^{-1}. Thus, we believe that this paper will provide further inspiration for high-performance rechargeable batteries.

4.5. References

1. Tarascon, J. M.; Armand, M., Issues and challenges facing rechargeable lithium batteries. *Nature* **2001**, *414* (6861), 359-367.

2. Bruce, P. G.; Scrosati, B.; Tarascon, J. M., Nanomaterials for rechargeable lithium batteries. *Angew. Chem. Int. Ed.* **2008**, *47* (16), 2930-2946.

3. Courtney, I. A.; Dahn, J. R., Electrochemical and in situ x-ray diffraction studies of the reaction of lithium with tin oxide composites. *J. Electrochem. Soc.* **1997**, *144* (6), 2045-2052.

4. Winter, M.; Besenhard, J. O., Electrochemical lithiation of tin and tin-based intermetallics and composites. *Electrochim. Acta* **1999**, *45* (1-2), 31-50.

5. Wang, J. W.; Fan, F. F.; Liu, Y.; Jungjohann, K. L.; Lee, S. W.; Mao, S. X.; Liu, X. H.; Zhu, T., Structural Evolution and Pulverization of Tin Nanoparticles during Lithiation-Delithiation Cycling. *J. Electrochem. Soc.* **2014**, *161* (11), F3019-F3024.

6. Huang, J. Y.; Zhong, L.; Wang, C. M.; Sullivan, J. P.; Xu, W.; Zhang, L. Q.; Mao, S. X.; Hudak, N. S.; Liu, X. H.; Subramanian, A.;

Fan, H. Y.; Qi, L. A.; Kushima, A.; Li, J., In Situ Observation of the Electrochemical Lithiation of a Single SnO_2 Nanowire Electrode. *Science* **2010**, *330* (6010), 1515-1520.

7.   Cao, M. D.; Zhang, M.; Xing, L. L.; Wang, Q.; Xue, X. Y., One-step preparation of pomegranate-shaped Sn/SnO_x/nanocarbon composites for fabricating ultrafast-charging/long-life lithium-ion battery. *J Alloy Compd.* **2017**, *694*, 30-39.

8.   Liu, L. J.; Huang, X. K.; Guo, X. R.; Mao, S.; Chen, J. H., Decorating in situ ultrasmall tin particles on crumpled N-doped graphene for lithium-ion batteries with a long life cycle. *J. Power Sources* **2016**, *328*, 482-491.

9.   Guo, Y. Y.; Zeng, X. Q.; Zhang, Y.; Dai, Z. F.; Fan, H. S.; Huang, Y.; Zhang, W. N.; Zhang, H.; Lu, J.; Huo, F. W.; Yan, Q. Y., Sn Nanoparticles Encapsulated in 3D Nanoporous Carbon Derived from a Metal-Organic Framework for Anode Material in Lithium-Ion Batteries. *ACS Appl. Mater. Interfaces* **2017**, *9* (20), 17173-17178.

10.   Zhang, N.; Zhao, Q.; Han, X. P.; Yang, J. G.; Chen, J., Pitaya-like Sn@C nanocomposites as high-rate and long-life anode for lithium-

ion batteries. *Nanoscale* **2014**, *6* (5), 2827-2832.

11.   Li, W. Y.; Li, Z.; Yang, F.; Fang, X. J.; Tang, B. H. J., Synthesis and Electrochemical Performance of SnO_x Quantum Dots@ UiO-66 Hybrid for Lithium Ion Battery Applications. *ACS Appl. Mater. Interfaces* **2017**, *9* (40), 35030-35039.

12.   Kravchyk, K.; Protesescu, L.; Bodnarchuk, M. I.; Krumeich, F.; Yarema, M.; Walter, M.; Guntlin, C.; Kovalenko, M. V., Monodisperse and Inorganically Capped Sn and Sn/SnO_2 Nanocrystals for High-Performance Li-Ion Battery Anodes. *J. Am. Chem. Soc.* **2013**, *135* (11), 4199-4202.

13.   Xu, L. P.; Kim, C.; Shukla, A. K.; Dong, A. G.; Mattox, T. M.; Milliron, D. J.; Cabana, J., Monodisperse Sn Nanocrystals as a Platform for the Study of Mechanical Damage during Electrochemical Reactions with Li. *Nano Lett.* **2013**, *13* (4), 1800-1805.

14.   Song, H. Z.; Li, X. F.; Cui, Y. H.; Xiong, D. B.; Wang, Y. F.; Zeng, J. S.; Dong, L. T.; Li, D. J.; Sun, X. L., Controllable lithium storage performance of tin oxide anodes with various particle sizes. *Int. J. Hydrogen Energ.* **2015**, *40* (41), 14314-14321.

15. Wang, Z. Y.; Wang, D.; Luo, S. H.; Bao, S.; Liu, Y. G.; Qi, X. W.; He, C. N. A.; Shi, C. S.; Zhao, N. Q., Three-dimensional porous bowl-shaped carbon cages interspersed with carbon coated Ni-Sn alloy nanoparticles as anode materials for high-performance lithium-ion batteries. *New J. Chem.* **2017**, *41* (1), 393-402.

16. He, M.; Yuan, L. X.; Hu, X. L.; Zhang, W. X.; Shu, J.; Huang, Y. H., A SnO_2@carbon nanocluster anode material with superior cyclability and rate capability for lithium-ion batteries. *Nanoscale* **2013**, *5* (8), 3298-3305.

17. Courtney, I. A.; McKinnon, W. R.; Dahn, J. R., On the aggregation of tin in SnO composite glasses caused by the reversible reaction with lithium. *J. Electrochem. Soc.* **1999**, *146* (1), 59-68.

18. Dai, R. L.; Sun, W. W.; Lv, L. P.; Wu, M. H.; Liu, H.; Wang, G. X.; Wang, Y., Bimetal-Organic-Framework Derivation of Ball-Cactus-Like Ni-Sn-P@C-CNT as Long-Cycle Anode for Lithium Ion Battery. *Small* **2017**, *13* (27).

19. Shi, S. J.; Deng, T. T.; Zhang, M.; Yang, G., Fast facile synthesis of SnO_2/Graphene composite assisted by microwave as anode material

for lithium-ion batteries. *Electrochim. Acta* **2017**, *246*, 1104-1111.

20.   Han, Q. G.;   Yi, Z.;   Wang, F. X.;   Wu, Y. M.; Wang, L. M., Preparation of bamboo carbon fiber and sandwich-like bamboo carbon fiber@SnO$_2$@carbon composites and their potential application in structural lithium-ion battery anodes. *J. Alloy Compd.* **2017**, *709*, 227-233.

21.   Shi, X.;   Song, H. H.;   Li, A.;   Chen, X. H.;   Zhou, J. S.; Ma, Z. K., Sn-Co nanoalloys embedded in porous N-doped carbon microboxes as a stable anode material for lithium-ion batteries. *J. Mater. Chem. A* **2017**, *5* (12), 5873-5879.

22.   Zhou, X. S.; Wan, L. J.; Guo, Y. G., Binding SnO$_2$ Nanocrystals in Nitrogen-Doped Graphene Sheets as Anode Materials for Lithium-Ion Batteries. *Adv. Mater.* **2013**, *25* (15), 2152-2157.

23.   Lin, J.; Peng, Z. W.; Xiang, C. S.; Ruan, G. D.; Yan, Z.; Natelson, D.; Tour, J. M., Graphene Nanoribbon and Nanostructured SnO$_2$ Composite Anodes for Lithium Ion Batteries. *ACS Nano* **2013**, *7* (7), 6001-6006.

24.   Zhang, H. W.; Huang, X. D.; Noonan, O.; Zhou, L.; Yu, C. Z.,

Tailored Yolk-Shell Sn@C Nanoboxes for High-Performance Lithium Storage. *Adv. Funct. Mater.* **2017**, *27* (8).

25.   Chang, X. H.; Wang, T.; Liu, Z. L.; Zheng, X. Y.; Zheng, J.; Li, X. G., Ultrafine Sn nanocrystals in a hierarchically porous N-doped carbon for lithium ion batteries. *Nano Research* **2017**, *10* (6), 1950-1958.

26.   Lee, H.; Dellatore, S. M.; Miller, W. M.; Messersmith, P. B., Mussel-inspired surface chemistry for multifunctional coatings. *Science* **2007**, *318* (5849), 426-430.

27.   Du, F. H.; Liu, Y. S.; Long, J.; Zhu, Q. C.; Wang, K. X.;   Wei, X.; Chen, J. S., Incorporation of heterostructured Sn/SnO nanoparticles in crumpled nitrogen-doped graphene nanosheets for application as anodes in Lithium-ion batteries. *Chem. Commun.* **2014**, *50* (69), 9961-9964.

28.   Ma, Z. X.; Kyotani, T.; Tomita, A., Preparation of a high surface area microporous carbon having the structural regularity of Y zeolite. *Chem. Commun.* **2000**, (23), 2365-2366.

29.   Song, P.; Bo, X. J.; Nsabimana, A.; Guo, L. P., Additional doping of phosphorus into polypyrrole functionalized nitrogenous carbon

nanotubes as novel metal-free oxygen reduction electrocatalyst in alkaline solution. *Int. J. Hydrogen Energ.* **2014**, *39* (28), 15464-15473.

30.   Huang, X. X.; Yang, Z. Y.; Dong, B.; Wang, Y. Z.; Tang, T. Y.; Hou, Y. L., In situ Fe_2N@N-doped porous carbon hybrids as superior catalysts for oxygen reduction reaction. *Nanoscale* **2017**, *9* (24), 8102-8106.

31.   Zhang, L.; Zhao, K. N.; Yu, R. H.; Yan, M. Y.; Xu, W. W.; Dong, Y. F.; Ren, W. H.; Xu, X.; Tang, C. J.; Mai, L. Q., Phosphorus Enhanced Intermolecular Interactions of SnO_2 and Graphene as an Ultrastable Lithium Battery Anode. *Small* **2017**, *13* (20).

32.   Ishizaki, T.; Wada, Y.; Chiba, S.; Kumagai, S.; Lee, H.; Serizawa, A.; Li, O. L.; Panomsuwan, G., Effects of halogen doping on nanocarbon catalysts synthesized by a solution plasma process for the oxygen reduction reaction. *Phys. Chem. Chem. Phys.* **2016**, *18* (31), 21843-21851.

33.   Dai, R. L.; Sun, W. W.; Wang, Y., Ultrasmall Tin Nanodots Embedded in Nitrogen-Doped Mesoporous Carbon: Metal-Organic-Framework Derivation and Electrochemical Application as Highly

Stable Anode for Lithium Ion Batteries. *Electrochim. Acta* **2016**, *217*, 123-131.

34.   Yue, W. B.; Yang, S.; Ren, Y.; Yang, X. J., In situ growth of Sn, SnO on graphene nanosheets and their application as anode materials for lithium-ion batteries. *Electrochim. Acta* **2013**, *92*, 412-420.

35.   Wang, H. G.; Jiang, C.; Yuan, C. P.; Wu, Q.; Li, Q.; Duan, Q., Complexing agent engineered strategy for anchoring SnO_2 nanoparticles on sulfur/nitrogen co-doped graphene for superior lithium and sodium ion storage. *Chem. Eng. J.* **2018**, *332*, 237-244.

36.   Yang, G.; Yan, Z.; Cui, L.; Qu, Y.; Li, Q.; Li, X.; Wang, Y.; Wang, H., Electroless plating of a Sn-Ni/graphite sheet composite with improved cyclability as an anode material for lithium ion batteries. *RSC Advances* **2018**, *8* (28), 15427-15435.

37.   Qin, J.; Liu, D.; Zhao, N.; Shi, C.; Liu, E.-Z.; He, F.; Ma, L.; Li, Q.; Li, J.; He, C., Fabrication of Sn-core/CNT-shell nanocable anchored interconnected carbon networks as anode material for lithium ion batteries. *Mater. Lett.* **2018**, *212*, 94-97.

38.   Mao, M. L.; Yan, F. L.; Cui, C. Y.; Ma, J. M.; Zhang, M.; Wang,

T. H.; Wang, C. S., Pipe-Wire TiO$_2$-Sn@Carbon Nanofibers Paper Anodes for Lithium and Sodium Ion Batteries. *Nano Lett.* **2017**, *17* (6), 3830-3836.

39.   Zhang, Q.; Gao, Q. M.; Qian, W. W.; Zhang, H.; Tan, Y. L.; Tian, W. Q.; Li, Z. Y.; Xiao, H., Graphene-based carbon coated tin oxide as a lithium ion battery anode material with high performance. *J. Mater. Chem. A* **2017**, *5* (36), 19136-19142.

40.   An, G. H.; Lee, D. Y.; Ahn, H. J., Tofu-derived carbon framework with embedded ultrasmall tin nanocrystals for high-performance energy storage devices. J Alloy Compd 2017, 722, 60-68.

41.   Huang, X. K.; Cui, S. M.; Chang, J. B.; Hallac, P. B.; Fell, C. R.; Luo, Y. T.; Metz, B.; Jiang, J. W.; Hurley, P. T.; Chen, J. H., A Hierarchical Tin/Carbon Composite as an Anode for Lithium-Ion Batteries with a Long Cycle Life. *Angew. Chem. Int. Ed.* **2015**, *54* (5), 1490-1493.

42.   An, W. L.; Fu, J. J.; Mei, S. X.; Xia, L.; Li, X. X.; Gu, H. Z.; Zhang, X. M.; Gao, B.; Chu, P. K.; Huo, K. F., Dual carbon layer hybridized mesoporous tin hollow spheres for fast-rechargeable and

highly-stable lithium-ion battery anodes. *J. Mater. Chem. A* **2017**, *5* (27), 14422-14429.

43.   Zhu, X. J.; Guo, Z. P.; Zhang, P.; Du, G. D.; Zeng, R.; Chen, Z. X.; Li, S.; Liu, H. K., Highly porous reticular tin-cobalt oxide composite thin film anodes for lithium ion batteries. *J. Mater. Chem.* **2009**, *19* (44), 8360-8365.

44.   Mondal, A. K.; Su, D. W.; Chen, S. Q.; Ung, A.; Kim, H. S.; Wang, G. X., Mesoporous $MnCo_2O_4$ with a Flake-Like Structure as Advanced Electrode Materials for Lithium-Ion Batteries and Supercapacitors. *Chem.-Eur. J.* **2015**, *21* (4), 1526-1532.

45.   Jiang, X.; Yang, X. L.; Zhu, Y. H.; Yao, Y. F.; Zhao, P.; Li, C. Z., Graphene/carbon-coated Fe_3O_4 nanoparticle hybrids for enhanced lithium storage. *J. Mater. Chem. A* **2015**, *3* (5), 2361-2369.

Chapter 5. Conclusion

The objective of this thesis is to improve the cycling stability and rate capability of LFP cathode and Sn anode by efficient carbon network. The efficient carbon network synthesized from a carbon additives (RGO, and carbonized melamine foam) by using polydopamine binder. To optimize the cycling stability and rate capability, small particles with carbon network should be achieved.

First, we developed the RGO based carbon network using dual layer coating strategy for high performance LFP cathode material. LFP particles act as a spacer, which prevent restacking of RGO and form a porous structure. In addition, LFP particles are anchored to graphene layers due to the interaction between polydopamine and GO, led to fast electron transport.

Second, melamine foam was chosed as a carbon precursor to form the carbon network. The carbonized melamine foam can easily break into small pecese and form the porous structure. This carbon structure provide the high surface area for anchoring the LFP particles, pore space for Li ion migration, and carbon network for electron pathway.

Third, ultrafine Sn nanoparticles anchored on nitrogen- and phosphorous-doped hollow carbon frameworks were synthesize using a

simple melt diffusion method. Efficient carbon network enable molten Sn to form ultrafine Sn nanoparticles uniformly on the carbon support. In addition, doping elements (N, P) help Sn to be anchored on the carbon support. Well-woven carbon network provide the efficient electron and ion diffusion path.

Through this thesis, simple and well-designed carbon network has been developed for cathode, and anode materials. This carbon network works very well both LFP and Sn leading to high rate performance and cycling stability. The efficient carbon network not only improves electronic conductivity at the material level, but also improves ionic conductivity and electrical conductivity at the battery system level. This combined approach to develop the efficient carbon network can be potentially utilized for various other electrode materials in many other applications such as supercapacitor and eletrocatalyst, too.

Bibliography

1. International Publications

1) Sohee Lee, **<u>Jiseop Oh</u>**, Dongwon Kim, Yuanzhe Piao*, "A sensitive electrochemical sensor using an iron oxide/graphene composite for the simultaneous detection of heavy metal ions", *Talanta*, **2016**, 160, 528–536.

2) Minsik Hwang[+], **<u>Jiseop Oh</u>**[+], Jeongmin Kang, Kwang-dong Seong, Yuanzhe Piao*, "Enhanced active sites possessing three-dimensional ternary nanocomposites of reduced graphene oxide/polyaniline/Vulcan carbon for high performance supercapacitors", *Electrochimica Acta*, **2016**, 221, 23-30. ([+]**Co-first author)**

3) **<u>Jiseop Oh</u>**[+], Jeongyeon Lee[+], Taejin Hwang, Jong Min Kim, Kwang-dong Seoung, Yuanzhe Piao*, "Dual Layer Coating Strategy Utilizing N-doped Carbon and Reduced Graphene Oxide for High-Performance LFP Cathode Material", *Electrochimica Acta*, **2017**,

231, 85-93. ([+]**Co-first author**)

4) Jong Min Kim, Valentina Guccini, Kwang-dong Seong, **<u>Jiseop Oh</u>**, German Salazar-Alvarez*, Yuanzhe Piao*, "Extensively Interconnected Silicon Nanoparticles via Carbon Network Derived from Ultrathin Cellulose Nanofibers as High Performance Lithium Ion Battery Anodes", *Carbon*, **2017**, 118, 8-17.

5) Jong Min Kim[+], Dongjin Ko[+], **<u>Jiseop Oh</u>**, Jeongyeon Lee, Taejin Hwang, Youngmoo Jeon, Wytse Hooch Antink, Yuanzhe Piao*, "Electrochemically Exfoliated Graphene as a Novel Microwave Susceptor: the Ultrafast Microwave-assisted Synthesis of Carbon-coated Silicon-graphene Film as Lithium-ion Battery Anode", *Nanoscale*, **2017**, 9, 15582–15590.

6) Jeongyeon Lee[+], Taejin Hwang[+], **<u>Jiseop Oh</u>**, Jong Min Kim, Youngmoo Jeon, Yuanzhe Piao*, "Sn/SnO$_x$-loaded Uniform-sized Hollow Carbon Spheres on Graphene Nanosheets as an Anode for Lithium-ion Batteries", *Journal of Alloys and Compounds*, **2018**, 736, 42-50.

7) Dongwon Kim, Jong Min Kim, Youngmoo Jeon, Jeongyeon Lee, **<u>Jiseop Oh</u>**, Wytse Hooch Antink, Daekyu Kim, Yuanzhe Piao*, "Novel Two-step Activation of Biomass-derived Carbon for Highly Sensitive Electrochemical Determination of Acetaminophen", *Sensors and Actuators B: Chemical*, **2018**, 259, 50-58.

8) **<u>Jiseop Oh</u>**[+], Jeongyeon Lee[+], Youngmoo Jeon, Jong Min Kim, Kwang-dong Seong, Taejin Hwang, Seungman Park, Yuanzhe Piao*, "Ultrafine Sn Nanoparticles Anchored on Nitrogen- and Phosphorus-Doped Hollow Carbon Frameworks for Lithium Ion Batteries", *ChemElectroChem*, **2018**, 5, 2098–2104. ([+]**Co-first author**)

9) Jong Min Kim, Valentina Guccini, Dongwon Kim, **<u>Jiseop Oh</u>**, Seungman Park, Youngmoo Jeon, Taejin Hwang, German Salazar-Alvarez*, Yuanzhe Piao*, "A Novel Textile-like Carbon Wrapping for High-performance Silicon Anodes in Lithium-ion Batteries", *Journal of Materials Chemistry A*, **2018**, 6, 12475–12483.

10) Jeongyeon Lee[+], **<u>Jiseop Oh</u>**[+], Youngmoo Jeon, Yuanzhe Piao*, "Multi-heteroatom-doped Hollow Carbon Attached on Graphene using $LiFePO_4$ nanoparticles as Hard Templates for High-performance Lithium-sulfur Batteries", *ACS Applied Materials & Interfaces*, **2018**, 10, 26485–26493. ([+]**Co-first author)**

11) **<u>Jiseop Oh</u>**[+], Jeongyeon Lee[+], Youngmoo Jeon, Seungman Park, Jong Min Kim, Taejin Hwang, Yuanzhe Piao*, "Melamine foam derived N-doped carbon framework and Graphene supported $LiFePO_4$ composite for high performance lithium ion battery cathode material", *ACS Sustainable Chemistry & Energy*, Accepted. ([+]**Co-first author)**

국 문 초 록

지구온난화의 문제가 도래한 이후로, 녹색 에너지기술들과 전기차 기술들은 온실가스의 배출을 줄일 수 있는 하나의 대안으로 제시되었다. 리튬이차전지는 가벼우면서도 높은 에너지밀도를 가져 이러한 전기차에 적합한 에너지지정장치로 주목받고있다. 에너지지정장치가 전기차와 같은 높은 출력을 필요로하는 장치에 사용되기 위해서는 높은 출력특성과, 가격의 합리성, 그리고 안정성을 갖춰야 한다. 리튬이차전지는 전극에서의 전자전도와 이온전도가 느려 전체적으로 안좋은 출력특성을 보인다. 이러한 양극과 음극에서의 출력특성을 보완하기 위해서는 전극물질의 개질과 전극의 구조제어가 반드시 고려되어야 한다.

폴리도파민에서 비롯된 질소도핑된 탄소와 rGO 두가지의 탄소재료를 사용하는 이중 탄소층 코팅 전략을 LFP에 율특성을 개선하기 위해여 적용하였다. 이중의 탄소층은 one-pot에서의 중합과정과 열처리과정을 통해 만들어졌다. 두개의 탄소로 코팅된 LFP는 30 C에서 방전시 98 mAh g⁻¹의 용량을 보였고, 수명특성은 10 C에서 700번 충/방전 후에도 115 mAh g⁻¹의

방전용량을 보이며 초기 용량 대비 96.18%의 용량을 유지하였다. 이러한 뛰어난 율특성과 수명특성은 질소 도핑된 탄소코팅에 의한 전기전도성의 향상과 잘 연결되어있는 전자진로, 그리고 작은 입자사이로의 빠른 리튬이온의 전도등에 의한것으로 나타난다.

질소 도핑된 탄소로 코팅된 LFP 나노입자를 rGO가 감싸고있는 질소 도핑된 탄소구조체에 붙여 복합체를 만들었고, 이때 폴리도파민을 접착제면서 동시에 탄소 코팅재로 사용하여 이를 리튬이차전지 양극재로 연구하였다. 질소 도핑된 탄소구조체는 LFP입자가 붙을 수 있는 표면을 제공하고, 리튬이온이 이동할 수 있는 기공을 제공하면서, 전자가 빠르게 이동할 수 있는 탄소 네트워크를 제공한다. LFP 나노입자는 폴리도파민과 rGO간에 상호작용으로 조밀하게 붙는다. 게다가 rGO와 폴리도파민과의 상호작용은 전극의 수명의 안정성에 도움을 준다. 이렇게 만들어진 NCFG-NCL 물질은 2 C에서 500번 충/방전을 하여도 처음 방전용량 대비 92.2%를 유지하는 좋은 수명특성을 보였다. 또한 20 C에서도 108 mAh g^{-1}의 인상적인 방전용량을 보였다.

매우 작은 Sn 나노입자를 그래핀-hollow 탄소구조체(G-HCF)에 붙였고 이를 리튬이온 배터리 음극물질로 연구하였다.

매우 작은 Sn입자는 G-HCF에 붙여 Sn입자들끼리의 aggregation을 막아주었다. Hollow한 구조는 Sn입자가 충/방전시에 부피팽창을 수용할 수 있는 여분의 공간을 제공해서 Sn이 전극에서 떨어져나가는 것을 방지하였다. 게다가 상호연결된 hollow한 탄소구조는 리튬이온과 전자가 빠르게 이동 할 수 있게하여 전극의 율특성을 향상시킨다. 이렇게 만들어진 G-HCF-Sn 복합체는 1 A g^{-1}의 전류밀도에서 1000번 충/방전 후에도 1048 mAh g^{-1}의 용량을 보이며 좋은 수명특성을 보였다.

주요어: 탄소네트워크, 폴리도파민, 그래핀, 멜라민폼, 리튬이온 배터리

학   번: 2013-23750